Title
Development of a Bioartificial Pancreas Using Size-Controlled Insulin-Secreting Cell Clusters

Author
Mendelsohn, Adam

Publication Date
2011

Development of a Bioartificial Pancreas Using Size-Controlled Insulin-Secreting Cell Clusters

by

Adam Daniel Mendelsohn

DISSERTATION

Submitted in partial satisfaction of the requirements for the degree of

DOCTOR OF PHILOSOPHY

in

Bioengineering

in the

GRADUATE DIVISION

of the

UNIVERSITY OF CALIFORNIA, SAN FRANCISCO

AND

UNIVERSITY OF CALIFORNIA, BERKELEY

Dedications and Acknowledgements

I want to express gratitude for all of the support I received throughout my graduate program from all of my family and friends without which the process would have been much more difficult and much less enjoyable. Their interest in learning about my research encouraged my continued effort and belief in the pursuit's worthiness. I want to especially thank my mom and dad, whose love has been essential in my achievements so far and will always serve as continued inspiration. There have been an uncountably large number of graduate students, post-doctoral researchers and faculty who have provided pivotal pieces of advice and wisdom that I will carry with me as I continue my endeavors. Specifically, I would like to thank the members of my thesis committee, Kevin Healy, Michael German, and especially Tejal Desai for the support she has provided in my research and towards the numerous other activities I engaged in while in graduate school.

The following dissertation includes work that has been published, and the co-authors of these publications deserve recognition. Chapter 2 is based on a textbook chapter published by Landes Bioscience in 2010 and was co-authored with Tejal Desai. Chapter 4 is based on a work published in Langmuir in 2010 that was co-authored with Daniel Bernards, Rachel Lowe and Tejal Desai. Daniel performed XPS characterization and Rachel Lowe performed FTIR characterization, while the rest of the work was done primarily by the author of this dissertation. Chapter 5 is based on a work that was recently accepted for publication in Stem Cell Research in 2011 co-authored with Dennis Van Hoof, Rena Seerke, Michael German and Tejal Desai. Dennis and the author of this dissertation both designed the experiments and wrote the manuscript. The author of this dissertation developed the techniques for patterning the stem cells and provided substrates to Dennis and Rena, who performed cell culture, differentiation and analysis under the supervision of Michael German. Chapter 6 is based on a work co-authored with Crystal Nyitray, Mark Sena and Tejal Desai that is currently in preparation. The author of this manuscript designed the experiments and wrote the manuscript, except for the RT-PCR which was performed by Crystal, who also aided in experiment design. Mark helped develop analysis techniques.

Development of a Bioartificial Pancreas Using Size-Controlled Insulin-Secreting Cell Clusters

By

Adam Daniel Mendelsohn

Transplantation of encapsulated insulin-secreting cell clusters represents a potential cure for type I diabetes, but development efforts so far have yet to live up to its promise. Recent studies have elucidated the importance of cluster size on the insulin response in a manner that affects viability and efficacy of transplanted clusters. Using microfabrication techniques, a method to fabricate uniformly-sized insulin-secreting cell clusters was developed and thoroughly characterized using water contact angle, x-ray photoelectron spectroscopy, Fourier transform infrared spectroscopy, and fluorescent microscopy. This technique enabled the formation of both monolayered and multilayered cell clusters of a predetermined size and shape. Subsequent evaluation of the impact that cluster size has on insulin expression, content and secretion using RT-PCR, ELISA, and confocal quantitative immunocytochemistry suggested that two cluster-size dependent behavioral changes relevant to transplant efficacy exist: First, glucose stimulation causes increased insulin production for clusters exceeding 40 μm in size. Second, cluster sizes greater than 60 μm secrete insulin more efficiently after production than smaller sized clusters. These results suggest that an optimal cluster size exists between 100-120 μm. Lastly, human embryonic stem cells were differentiated in

patterned 120 μm clusters along the pancreatic lineage, an effort that could produce optimally sized insulin-secreting cell clusters from a renewable cell supply. The studies presented here may help overcome two remaining challenges preventing encapsulated cell transplantation therapy from truly providing a cure for type I diabetes.

Table of Contents

Figures

Chapter 1 – Preface

The following dissertation represents this author's exploration of a cell-based type I diabetes treatment option with the potential to dramatically improve the lives for the millions who suffer from this disease. Three major factors, which are addressed in different capacities throughout, have prevented long-term efficacy and widespread adoption including: (1) immune rejection, (2) insufficient insulin production from transplanted cells, and (3) limited availability of suitable cell sources. Development efforts for this therapeutic approach have focused primarily on overcoming the immune response triggered upon introduction of foreign cells into a patient. Chapter 2 introduces the concept of cell-based drug delivery, explores the attempts that have been made in this pursuit, describes some limited success with immunosuppressant medication, and highlights possibilities for nanoporous membranes to decrease the need for immunosuppressants. Immunosuppression only replaces some of the inconveniences and side effects associated with the disease with, admittedly less severe, inconveniences and side effects associated with the treatment. As a result, the ability to transplant cells without immunosuppression remains the goal for cell-based drug delivery, and represents the motivation for this dissertation.

In order for immunoisolated cell-based drug delivery to succeed, transplanted cells must produce therapeutically effective insulin levels when transplanted in a capsule that prevents revascularization. Chapters 4 and 5 explore a critical but largely ignored factor, the size of the transplanted cluster, which has been implicated in insufficient insulin production after transplantation that has resulted in over half a century without successful administration. A set of multi-disciplinary techniques that enable the formation of precisely sized cell clusters are described, characterized, and applied towards evaluating the effect that cluster size has on insulin production. The techniques necessary to achieve this outcome derive from varying disciplines which are described in detail throughout Chapter 3. Furthermore, an optimal cluster size of 100-120 μm is suggested through rigorous studies evaluating the effect that cluster size has on proinsulin mRNA expression, insulin and c-peptide content, and insulin secretion.

In an attempt to overcome cell supply limitations while concurrently obtaining optimally sized clusters, the cell patterning techniques described were applied towards stem cell differentiation as described in Chapter 6. Human embryonic stem cells in 120 μm clusters were successfully differentiated towards pancreatic β-cell precursors when patterned on glass coverslips using the techniques developed here. Additionally, patterned clusters detached from the glass coverslips to form uniform spherical structures approximately 100 μm in diameter. Detachment of patterned cells is a necessary step prior to transplantation, and these results highlight the exciting potential for this technique to enable transplantation of uniform optimally-sized clusters that utilize a renewable cell source. The work presented here was performed in a close collaboration with Dennis Van Hoof, a post-doctoral student in the lab of Dr. Michael German at UCSF.

After understanding the optimal size for a cell cluster prior to transplantation, and developing a method to produce these clusters from a renewable cell supply, additional methods to detach patterned clusters and an evaluation of appropriate extracellular environments for these cells are explored in Chapter 7. Additional evaluation of the extracellular environment most appropriate to enable cell cluster viability will be required prior to clinical translation of this therapeutic approach.

Chapter 2 – Cell-based Drug Delivery Background

Cell-based drug delivery has been proposed as a treatment for diseases characterized by cell degeneration including Parkinson's disease[1, 2], testicular dysfunction and hypogonadal disorders[3], and liver failure[4]. However, the driving force behind cell-based drug delivery research has been to improve the treatment of insulin dependent diabetes mellitus (IDDM). IDDM is characterized by the loss of pancreatic β-cell function which normally regulates the blood-glucose concentration by the secretion of insulin. Without functional β-cells, chronic hyperglycemia can lead to complications including retinopathy, neuropathy, nephropathy, and death. Healthy β-cells secrete insulin in quantities that are highly sensitive to the blood-glucose level, and successful IDDM treatment requires the same sensitivity to avoid debilitating events.

The first major advancement in treating IDDM occurred in 1922 with the first successful clinical trial using insulin[5]. Unfortunately, while insulin-replacement therapy has saved countless lives, 82 years later in 2004 diabetes remained one of the most deadly diseases, ranking 6th in the United States[6]. The most common insulin-replacement therapy requires frequent blood-glucose measurement through finger pricks as well as multiple insulin injections per day. The most advanced insulin-replacement therapy is approaching its ultimate goal of a closed-loop artificial pancreas, consisting of an artificial glucose sensor coupled to an insulin delivery pump[7]. So far the development has fallen short of its goals for two reasons. First, a fully implantable long-term insulin pump has not yet achieved clinical success, requiring the user to wear an external pump. Second, development of a long-term artificial glucose sensor remains elusive in part because of protein adsorption causing measurement drift, thus requiring frequent sensor calibration through finger pricking. As a result, while the current technologies offer remarkable advances for insulin-replacement therapy when used appropriately, proper treatment requires constant user attention. Lastly, even if glucose-sensing technologies improve, the algorithms with which the sensor communicates information to the pump to modulate insulin delivery kinetics represents only an approximation of blood-glucose regulation in healthy patients. Several companies continue to research towards a closed-loop artificial pancreas, including Medtronic Minimed Inc. and Roche Diagnostic's Disetronic.

1. Cell-Based Drug Delivery

An alternate approach to the replacement of insulin in treating IDDM is to transplant functional pancreatic β-cells either alone or as part of the Islets of Langerhans. The transplanted cells will sense extracellular glucose levels and secrete insulin accordingly, improving upon free drug delivery by eliminating the need for patient compliance and by enabling a more physiological regulation of glucose levels. While possessing greater therapeutic potential, cell-based drug delivery will not become widely accepted until its efficacy equals or surpasses that of insulin replacement therapy while offering decreased patient complications. Despite the promised benefits of cell-based drug delivery, however, sufficient transplant viability has not yet been achieved.

One challenge involved with cell-based drug delivery is immune-mediated destruction of the transplanted cells. The immune system can destroy transplanted cells through a variety of mechanisms. The most severe modality characterized by transplant rejection within minutes, called hyperacute rejection, has not frequently occurred with islet transplants in rodent models[8]. The most common islet transplant rejection modality is a delayed antibody response for which the dominant mechanisms differ between allotransplants and xenotransplants. For allotransplants, antibody binding usually occurs with antigens presented on major histocompatibility complex (MHC) class I molecules on the surface of a cell. The MHC complex varies among a species more than the attached expressed peptides. As a result, peptides shed from an allogenic cell are unlikely to be recognized by antigen-presenting cells (APC's) for activation of the indirect presentation pathway. On the other hand, antibodies will recognize the variation in the MHC complex for activation of the direct presentation pathway. Xenotransplants express peptides that differ from those of the host and can be more potent activators of the indirect presentation pathway, resulting in B-cell activation and the production of secreted forms of antibodies that can target the transplanted cells. As a result, allotransplants in general are thought to be sufficiently protected by avoiding direct cell-cell contact whereas xenotransplants require the isolation of antibodies as well. It should be noted that allotransplants can also elicit the indirect antigen presentation pathway leading to destruction, although to a lesser extent than that from xenotransplants, and therefore antibody isolation will likely result in improved viability of allotransplants as well.

An additional rejection modality for islet transplants is the production of macrophage-activating factors when under stress[9]. Islet transplant viability has been correlated with the release of monocyte chemoattractant protein-1 (MCP-1) and tissue factor (TF)[10]. These cytokines are associated with macrophage recruitment and activation. Upon activation, macrophages release inflammatory cytokines including tumor necrosis factor-α (TNF-α) and interleukin 1-β (IL-1β), which are implicated in β-cell death[9]. Interestingly, one study suggests that bovine islets are less susceptible to human cytokines than they are to bovine cytokines, suggesting that xenogenic cells might be better able to survive a cytokine response than allogenic human cells[11]. Therefore, an important consideration in islet transplantation is providing an environment which limits the production of macrophage-activating factors.

The only chance of avoiding the above immune responses without immunosuppression or immunoisolation is to transplant cells that are genetically identical to the patient. For type I diabetics, these are the cells that have degenerated and are therefore not available as autografts. Furthermore, type I diabetes is thought to have an autoimmune etiology, and therefore even the transplantation of pancreatic β-cells that are genetically identical to the recipient will be subject to the same degeneration that originally caused the patient's disease. Recently in Brazil, one study demonstrated the potential of autologous bone marrow-derived pancreatic stem cell transplantation following immune ablation[12]. Unfortunately, this study applied only to patients between ages 14-31 that were diagnosed with type I diabetes within 6 weeks prior to treatment. Furthermore, patient hospitalization and isolation was required because of the temporarily weakened immune system caused by ablation. While a small subset of type I diabetics may benefit from this treatment, more research is needed to determine whether it can be applied to a larger patient population.

2. Immunosuppressed Cell Transplantation

One approach to providing protection for islet transplants has been to chronically administer immunosuppressive medication. In this pursuit, whole organ pancreas transplantations are possible with immunosuppression. The complications are deemed worthwhile only for patients that are already undergoing transplantation of a life-sustaining organ such as a kidney. These complications include susceptibility to infection, decreased capability of healing wounds properly, and increased risk for developing lymphoma[13, 14]. Until recently, isolated islet transplantations had been much less successful than whole pancreas transplantations, with only 8% of patients maintaining insulin independence for up to one year in all procedures between 1990 and 1998[15]. More recently, isolated allogenic islet transplantation was validated using a medication regimen outlined in the Edmonton protocol that resulted in 7 of 7 patients who remained insulin independent one year after transplant[16]. However, a 5 year study of the same therapy resulted in only 10% of patients who remained insulin-independent[17]. Additionally, this therapy requires human donor pancreatic islets of which the supply is limited[18]. Currently, efforts are underway to differentiate pancreatic β-cells from human stem cell lines that could ultimately increase the supply for allogenic transplantations[19]. Unfortunately, insulin-independence for the patient has not been achieved through immunosuppressed xenogenic islet transplantation for which the current supply is much greater[20].

Some methods have been developed to potentially reduce or eliminate the need for immunosuppressive medication during islet transplantation. In vitro culture prior to transplantation has demonstrated decreased immune rejection[21]. Additionally, non-immunosuppressed xenotransplantation of embryonic pig tissue has demonstrated promise in treating diabetic rats[22-24]. However, no success has been reported in larger animals, although research is underway to better understand the immune response of primates to fetal xenogenic transplants[25]. As a result, immunosuppressed cell-based drug delivery and strategies to avoid immune rejection have not yet provided a treatment option that can be widely administered.

3. *Immunoisolated Cell-Based Drug Delivery*

3.1. *Origins*

A solution to increasing the viability of allo- and xenotransplanted cells without the complications of immunosuppressive therapy is their encapsulation in an immunoisolating semipermeable membrane. The membrane serves to impede contact with antibodies, complement, and cells, but allow transport of insulin, glucose, nutrients, and waste products. The relatively smaller size of insulin, glucose, and nutrients compared with antibodies, complement, and cells, has inspired the development of immunoisolated cell-based drug delivery; a cell secretes insulin when stimulated by extracellular glucose but is protected from immune-mediated death by a semipermeable membrane.

One of the first attempts resembling immunoisolated cell-based drug delivery for diabetes treatment occurred in 1933 through xenotransplantation of human insulinoma tissue using membranous bags into rats[26]. However, the field of immunoisolated transplantation became more formally established in the early 1950's through a series of experiments that examined the survival rates of allotransplanted tissue into an extravascular space with and without a cell-impermeable encapsulating membrane[27-30]. These experiments demonstrated prolonged survival of transplanted tissue when immune cell contact was prevented. The non-vascularized transplanted tissue, while receiving fewer nutrients, survived longer due to the lack of contact with the immune cells, preventing the direct antigen presentation pathway that leads to immune-mediated destruction.

The treatment of IDDM by immunoisolated cell transplantation was made possible only after the β-cell containing Islets of Langerhans were isolated in 1965[31]. Several immunoisolated transplantation methods were subsequently developed, including intravascular chambers, microcapsules, and extravascular chambers[32-34]. Each of these will be addressed in the following sections.

3.2. Intravascular Chambers

3.2.1. Motivation

Intravascular chamber development was motivated by the need for transplanted cells to regulate the blood-glucose level in a timely manner. These chambers directly access the blood, being separated only be a semipermeable membrane. Such an approach offers an advantage over both extravascular chambers and microcapsules, which are also implanted in an extravascular space, often in the peritoneal cavity. Glucose from the blood must first diffuse through the mesothelium that lines the peritoneal cavity in order to access the cells. As a result, the cells receive blood-glucose information that is delayed. This delay is exacerbated in humans because of the greater thickness of human mesothelium compared with that of animals. For example, human mesothelium is 4-5 times thicker than that of a rat[35]. If the delay is significant in duration, the patient will experience peaks and valleys of blood glucose concentrations that will increase the chance of debilitating events. Therefore, the intravascular chamber approach avoids the increased delay and for this reason is a promising approach for immunoisolated cell-based drug delivery.

3.2.2. Development

The development of intravascular transplantation chambers began with the development of methods to culture cells on artificial capillaries by Knazek and Chick[36, 37]. Sun, Tze, and Orsetti subsequently demonstrated some success in rats using Amicon (polyvinyl chloride-acrylic copolymer) membranes[38-40]. These membranes comprise an artificial capillary that is attached to the animal's vascular system. The cells surround the semipermeable capillary which protects them from contacting the immune cells flowing through the blood. Glucose and other nutrients diffuse across the membrane, directly stimulating the cells to secrete insulin, which quickly disperses throughout the body to regulate the metabolism of glucose. More on intravascular transplantation chamber has been reviewed elsewhere[34]

3.2.3. Commercialization

The intravascular chamber approach at one time inspired several companies to further develop the technology. One example, BioHybrid Technologies, founded in 1985, developed an intravascular transplantation chamber with limited success in transplanting allogenic islets into pancreatectomized dogs[41]. Unfortunately, commercial development of this approach was halted for reasons discussed below.

3.2.4. Failure modes

The intravascular approach was abandoned due to the inability to control blood coagulation issues. This problem has not yet been overcome, and these authors know of no current development in intravascular transplantation chamber technology. Perhaps as materials science advances or our ability to control biological processes improves and coagulation can be prevented, intravascular chamber transplantation for diabetes treatment will be revisited. However, even if coagulation can be controlled, the complications involved with implantation of an intravascular device are more dangerous than those involved with the implantation of an extravascular device.

3.3. Microcapsules

3.3.1. Motivation

Nutrient availability is another factor that determines the viability of cellular implants over time. For this reason, one design consideration in the early development of islet transplantation chambers were insulin and glucose diffusion across the membranes[42]. In order to optimize these diffusion rates, the surface area to volume ratio should be maximized. As a result, researchers began transplanting cells encapsulated in semipermeable microcapsules[43, 44]. Furthermore, microcapsule implantation can occur through injection, offering a less invasive procedure than the surgery required for transplantation chamber implantation.

3.3.2. Development

Cell microencapsulation was first mentioned by Chang in 1964[45]. However, it was not until 1980 that Lim and Sun applied microcapsules to diabetes treatment, demonstrating prolonged isograft islet survival when microencapsulated in alginate-polylysine-polyethyleneimine microcapsules[46]. Initially, microencapsulated islet transplantation delayed the return to hyperglycemia compared with the transplantation of unencapsulated islets by only 10 days and failed due to a lack of biocompatibility of the microcapsule itself. The microcapsule material was improved in 1984 by O'shea and Sun who removed the polyethyleneimine component and designed alginate to be the outer layer of the microcapsule[47]. The improved material demonstrated significant improvement, and in one of the five animals the microencapsulated islets remained viable for 365 days, when the experiment ended. An additional advantage of the new microcapsules was increased microcapsule strength. Efforts to further improve biocompatibility of alginate microcapsules involved decreasing the impurities and increasing the guluronic acid to mannuronic acid ratio[48, 49]. Other researchers questioned the reproducibility of alginate-polylysine microcapsules and explored either their coating with a polyethylene glycol hydrogel or manufacturing the microcapsules from a different material altogether such as a polyacrylate[50, 51] or silica[52]. In an optimization effort, Wang et al. evaluated over 1,000 combinations of polyanions and polycations with regards to suitability for cell encapsulation[53]. The result was a polyelctrolyte complexation process using 5 different polymers enabling independent control over capsule size, wall thickness, mechanical strength, and permeability. For further information, microencapsulation technology has been extensively reviewed elsewhere[54, 55].

3.3.3. Commercialization

The advances in microencapsulation technology have brought this approach to the forefront of islet transplantation therapy. Recent progress has resulted in several ongoing clinical trials. Dr. Calafiore led a study at the University of Perugia with two patients in 2006 receiving alginate-polylysine-polyornithine encapsulated islets[56]. Also, Novocell, Inc. recently presented interim data on a Phase I/II clinical trial using a photopolymerizable polyethylene glycol microcapsule[57]. In both cases, evidence existed that the islets were not rejected by the immune response throughout the duration of the trial. However, neither study resulted in insulin independence for the patient. It is important to note that although in 1994 Dr. Soon-Shiong was able to achieve insulin independence in a patient using alginate microencapsulated islets after 9 months, the patient was taking immunosuppressive therapy as well[58]. The work from Dr. Soon-Shiong's experiments is being pursued commercially by ReNeuron (previously Amcyte). In early 2007, Living Cell Technology (previously Diatranz) began their second clinical trial with a successful implant of neo-natal porcine islets encapsulated in alginate. Recently, interim data from Living Cell Technology indicates that one of two patients was successfully weaned off of insulin one month after transplantation, while the other was able to reduce exogenous insulin by 40%[59]. For how long the insulin independence will last is uncertain. Living Cell Technology's first trial was halted due to a ban on xenotransplantation issued by New Zealand in 1997 which has recently been repealed. Lastly, MicroIslet Inc., and Progenitor Cell Therapy are also working towards developing alginate-based microcapsules for diabetes treatment[60]. Clearly, the microencapsulation approach of immunoisolated cell-based drug delivery is flourishing.

3.3.4. Failure modes

Despite significant activity, microencapsulation technology still has not achieved clinical success. Several experiments point to some key factors that may be playing a role in transplant failure. Originally, the lack of biocompatibility of the membranes was associated with cellular overgrowth of the capsule, particularly when the islets are not completely encapsulated, and the resulting nutrient deficiency was blamed on transplant failure[61]. However, improved materials and encapsulation techniques have enabled microcapsule implants that lack significant cellular overgrowth (<10% of the microcapsules)[9]. One study that analyzed the cause of failure in the absence of overgrowth suggested that the failure was likely due to nutrient deficiency throughout the encapsulated cluster of cells, as illustrated by necrosis of the cells furthest away from a nutrient source[62]. However, a more recent study demonstrated that insulin secretion is also significantly reduced when the microcapsules are in a solution of activated macrophages compared to a solution without macrophages with identical nutrient availability[9]. Cytokines secreted by activated macrophages such as IL-1β (17.5 kD) and TNF-α (17 kD) have been implicated in transplant rejection[63, 64]. These cytokines are similar in size to insulin (5.6 kD). Therefore, any membrane that impedes diffusion of these and other cytokines will likely also affect nutrient and insulin diffusion. It is important, therefore, to ensure that the environment surrounding the transplanted cells minimizes the production of macrophage activating factors.

While microencapsulation technology is approaching human clinical success, there remain many disadvantages inherent with this approach. Microcapsule manufacturing processes have resulted in pore sizes with relatively broad distributions[65]. Even if cytokine-mediated cell death is limited, a broad pore size distribution presents a potentially insurmountable challenge in the attempt to isolate antibodies, complement and immune cells while allowing sufficient nutrient and insulin diffusion. An optimal membrane will completely isolate the encapsulated cells from the relevant antibodies and complement (IgG, IgM, and C_{1Q}). Transport inhibition of such molecules is particularly necessary for xenotransplants because of increased indirect antigen presentation[8]. Additionally, microcapsule walls are susceptible to having embedded islets enabling a portion of the islet that is not protected by the membrane to stimulate an immune response[66]. Although this limitation can be overcome, doing so typically requires a larger diameter microcapsule or a double layer, increasing the blood-glucose diffusion time[67]. Efforts are underway to create ultrathin microcapsule walls without any exposed portion of the islet, but *in vivo* success has not yet been demonstrated[68].

A further disadvantage of microcapsules is their difficulty in simultaneously achieving biocompatibility, immunoisolation, and a suitable environment that minimizes stress on the islets. To date, the design of microcapsules has focused on biocompatibility as well as achieving immunoisolation while allowing sufficient nutrient availability. However, the design that optimizes these parameters may compromise the environment surrounding the cells and negatively impact cell behavior. In addition to biocompatibility, nutrient availability, and immune protection, pancreatic β-cell behavior is also highly dependent on the surrounding matrix environment [69]. Therefore, the inability to independently control cell environment from membrane permeability will continue to present challenges for achieving therapeutic success of microencapsulated cells.

3.4. Extravascular Chambers

3.4.1. Motivation

Meanwhile, membranes manufactured from materials that cannot be formed into microcapsules have continued to advance. These membranes can be incorporated into a transplantation chamber such as those used by the early researchers in this field[27-30, 70, 71] (See Figure 2). Additionally, the design of the matrix environment surrounding the cells is independent from the design of the membranes, allowing for greater design flexibility. A further advantage of the extravascular transplantation chamber is that it is more easily retrievable than both intravascular chambers and microcapsules after implantation.

3.4.2. Development

The extravascular chamber method developed by Algire, Weaver, and Prehn, discussed earlier, in the 1950's for transplanting tissues was a natural starting point from which researchers could develop an extravascular chamber for immunoisolated islet transplantation[28-30]. During the 1970's, Millipore Corporation produced a commercially available extravascular transplantation chamber using the Algire approach[34]. These membranes typically had pore sizes on the order of 450 nm, a size sufficiently small to prevent direct cell-cell contact and therefore promising for allotransplants. Studies by Algire and colleagues demonstrated improved cell viability when encapsulated in these membranes[27, 70, 71]. Although many of the initial experiments involved syngeneic cells, transplant failure occurred nonetheless due to fibroblastic overgrowth of the graft and chamber, highlighting the importance of biocompatibility of the chamber to transplant success[34]. Significant advances have been made since these early experiments, and they have been reviewed extensively elsewhere[34, 72, 73].

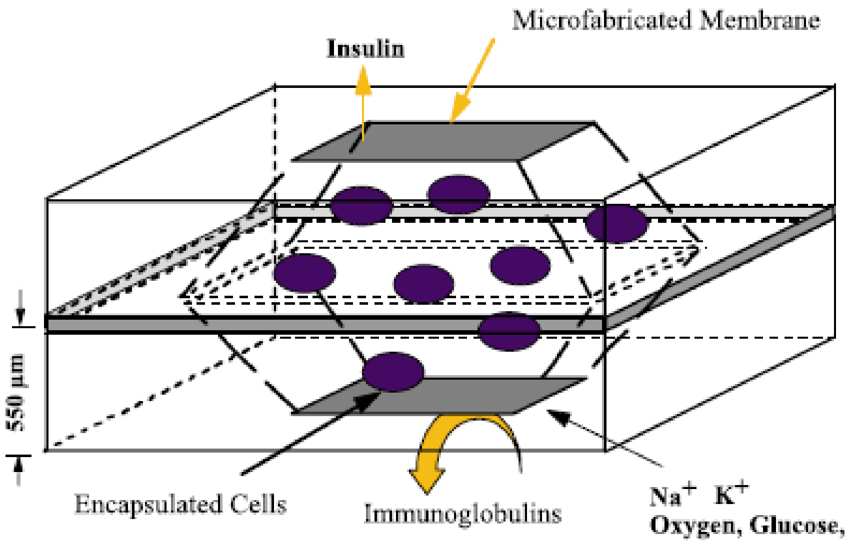

Figure 1 – Extravascular Transplantation Chamber
A device encloses a collection of cells with an immunoisolative membrane. Shown here is a cross-section of a device with cells in between two nanoporous membranes. Re-printed with permission from [74].

3.4.3. Commercialization

In the 1980's and 1990's, extravascular chamber technology became sufficiently advanced that many companies were funded for commercialization purposes. BetaGene partnered with Gore Hybrid Technologies to create a transplantation chamber for xenogenic immortalized pancreatic β-cells that Dr. Newgard, one of the founders, believed would possess better transplant viability. Baxter Healthcare developed a device for xenogenic immortalized pancreatic β-cells with some success in NOD mice[75]. Encelle Inc., recently acquired by Pioneer Surgical Technology, produced a biocompatible transplantation chamber to be implanted intramuscularly[76]. Cytotherapeutics Inc. created a similar transplantation chamber but for the application of Parkinson's treatment using immortalized neurosecretory cells that secrete dopamine and other factors. iMedd, Inc. investigated the use of silicon nanoporous membranes, which will be discussed in more detail later, for cell-based drug delivery based upon studies from the Desai laboratory (Figure 1)[77-79]. Cerco Medical (previously Islet Sheet Medical) is currently developing a transplantation chamber in the geometry of a sheet of islets surrounded by an alginate membrane[80]. Despite all of this activity, as far as these authors are aware, current clinical trials are not underway for cell-based drug delivery using transplantation chambers.

3.4.4. Failure Modes

Despite having the longest development history, extravascular transplantation chambers have not yet achieved clinical success. In the past it has been suggested that host fibroblastic response, poor graft oxygenation, and poor graft nutrition hindered the effectiveness of this immunoisolation approach[34]. However, current extravascular chambers can incorporate materials with improved biocompatibility and diffusion characteristics that may overcome these challenges, as discussed below. The remaining failure mode for extravascular chambers that cannot be overcome is the diffusion delay of glucose and insulin between the transplanted cells and the bloodstream. Further evaluation is required to determine whether this is an insurmountable obstacle preventing clinical success. This evaluation is ongoing for microencapsulated cells, where the diffusion delay of glucose and insulin is similar to that associated with extravascular transplantation chambers. Therefore, if microencapsulated cells demonstrate clinical success, the failure mode associated with the delay of glucose and insulin diffusion between the transplanted cells and the bloodstream should not prevent extravascular transplantation chambers from also achieving clinical success.

Immunoisolation Technology	Advantages	Disadvantages
Intravascular Chamber	1. Vascular access results in decreased diffusion time for glucose and insulin 2. Independent design of cell matrix environment and membrane	1. Blood coagulation leads to transplant failure 2. Increased complications due to invasive surgery 3. Currently limited to polymer membranes
Microcapsules	1. Improved nutrient availability depending on design 2. Less invasive implantation procedure	1. No vascular access results in increased diffusion time for insulin and nutrients 2. Currently limited to polymer membranes 3. Interdependent design of cell matrix environment and membrane
Extravascular Chamber	1. Flexibility of membrane material (i.e. inorganic nanoporous membranes) 2. Independent design of cell matrix environment and membrane 3. Less invasive implantation procedure compared with intravascular chambers	1. No vascular access results in increased diffusion time for insulin and nutrients 2. Limited diffusion depending on chamber design

Table 1 – Advantages and Disadvantages of Immunoisolation Technologies

4. Inorganic Nanoporous Membranes

Material advances inspired by the semiconductor, electronics, sensor and solar power applications have brought about the development of inorganic nanoporous membranes that have demonstrated promise for therapeutic applications such as cell-based drug delivery. Currently, inorganic nanoporous membranes that are useful for cell encapsulation can be manufactured from silicon, aluminum, and titanium. The nature of these membranes makes them useful only for extravascular transplantation chambers. Transplantation chambers compare favorably with microcapsules because of: 1) the ability to independently control the cell matrix environment and the membrane parameters, enabling the design of an environment more likely to achieve proper cell behavior, and 2) the ability to avoid the risk of incomplete cell protection by loading the cell-matrix after the membrane has been fabricated. Additionally, inorganic nanoporous membranes compare favorably with membranes traditionally used for transplantation chambers as well as microcapsules because of: 1) the tighter pore size distribution of inorganic nanoporous membranes, and 2) the decreased diffusion time and variability associated with a thinner and more precisely controllable membrane thickness. The membranes traditionally used for extravascular transplantation chambers as well as microcapsules have been polymer membranes, and will be referred to from now on as such.

4.1. Silicon Nanoporous Membranes

Silicon nanoporous membranes are the most extensively studied of the inorganic nanoporous membranes[81]. The processes for altering the surface of a silicon wafer are well understood as a result of integrated circuit development for computer chips. This precise control has enabled the fabrication of a nanoporous membrane with incredible precision that has proven useful for cell-based drug delivery.

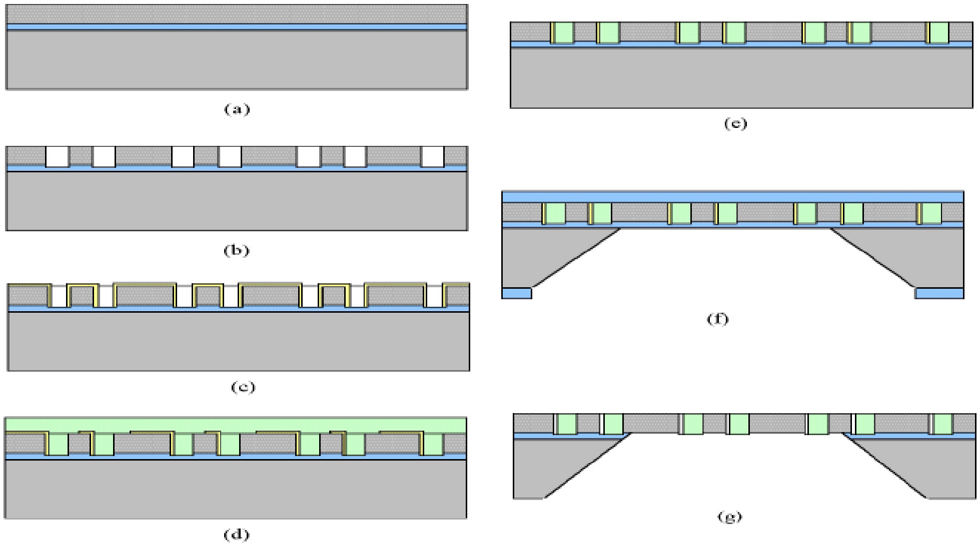

Figure 2 – Silicon Nanoporous Membrane Fabrication

(a) – Support ridges are fabricated from a silicon wafer using lithography; Silicon nitride etch-stop layer is deposited; Polysilicon base layer fills the remainder of the space between support ridges.
(b) – Holes etched through the base layer define the geometry of the pores.
(c) – Sacrificial oxide layer is thermally-grown which defines the width of the pores.
(d) – Sacrificial oxide is selectively etched to reveal anchor points; Plug polysilicon layer is deposited.
(e) – Surface is planarized until sacrificial oxide layer is exposed.
(f) – Nitride protective layer is deposited covering all sides of the wafer; Windows are etched through nitride layer in areas where membrane exposure is desired.
(g) – 80 °C KOH etches exposed silicon up to silicon nitride etch-stop layer.
(HF etch removes all nitride and sacrificial oxide layers – not shown)
Re-printed with permission from [82].

4.1.1. Preparation

Silicon nanoporous membranes are prepared initially from silicon wafers. A comprehensive outline of the history and development of the silicon membrane was previously reviewed by Leoni[74]. Presented here is the most current manufacturing strategy, also previously described (Figure 2)[82, 83]. First, a support ridge structure is photo-lithographically etched to provide mechanical support to the final structure[81]. A low-stress silicon nitride layer is deposited over the top surface of the wafer. The membrane structure will be formed on top of the silicon nitride, which will serve as an etch-stop for future processes. This etch-stop layer is very thin and small in comparison to the depth between support ridges. A polysilicon film, henceforth referred to as the base layer, is deposited on top of the silicon nitride layer, filling the remaining space between support ridges. The thickness of the base layer will determine the overall thickness of the nanoporous membrane.

Holes are then etched through the base layer but not through the nitride etch-stop layer. The geometry of the holes determines the shape of the pores. This geometry is defined by a thermally-grown oxide layer mask and etched using chlorine plasma. Another sacrificial thermally-grown oxide layer is formed, covering all silicon surfaces, but not the nitride etch-stop layer. The thickness of this sacrificial layer will determine the pore size. This oxide layer can be controlled to within 0.5 nm in thickness through thermal oxidation in dry oxygen, enabling pore sizes between 10 and 100 nm as well as tight pore size distributions[83].

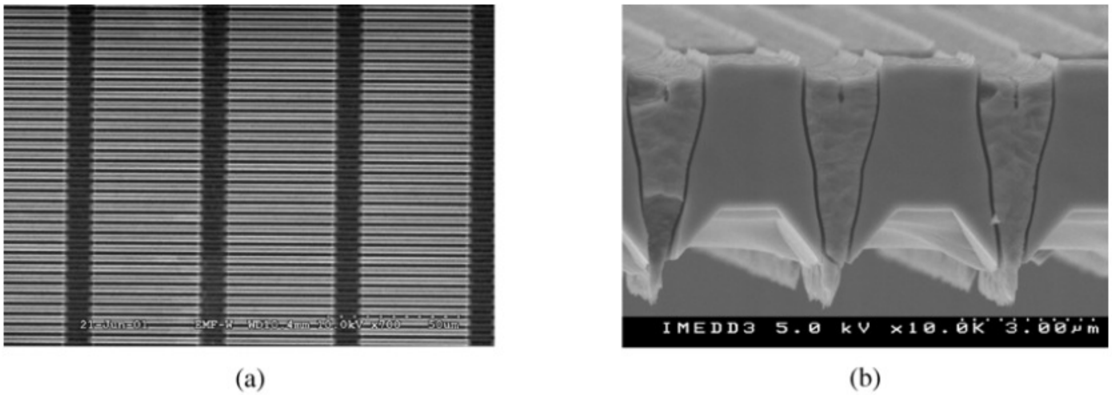

(a)

(b)

Figure 3 – SEM Micrographs of Silicon Nanoporous Membrane
(a) – Top view detail.
(b) – Side view detail.
Re-printed with permission from [84].

The next step involves plugging the holes that were created in the base layer. In order for the plug material to become attached to the base material, anchor points are defined by selective etching of the oxide layer. Another polysilicon layer, henceforth referred to as the plug layer, is then deposited that fills the holes, attaching to the base layer at the anchor points. The surface is then planarized using chemical mechanical polishing to remove the over-filled plug layer until it exists only within the base layer, leaving a smooth surface with the sacrificial oxide exposed.

Subsequently, a nitride protective layer is deposited completely covering both sides of the wafer. This layer is impervious to KOH etching. Windows are etched through the nitride layer in the areas where membrane exposure is desired. Then, an 80˚C KOH etch is performed that will remove the exposed silicon only as far as the nitride etch-stop layer. Finally, a HF etch removes the protective and etch-stop nitride layers as well as the sacrificial oxide layer. The finished product is a silicon nanoporous membrane with highly controllable pore channel widths (Figure 3)[84].

4.1.2. Advantages

The silicon nanoporous membrane has the potential to overcome all of the limitations associated with polymer membranes discussed above. Pore widths of 18 nm have demonstrated significant diffusion resistance to IgG while allowing relatively unrestricted diffusion of insulin and glucose[79, 85]. Furthermore, the highly controllable pore channel width to within 0.5 nm[86] results in a substantially tighter pore size distribution of approximately 5% compared with the 30% distributions that can be associated with polymer membranes[65]. It has been suggested that if only 1% of the pore sizes exceed the desired cut-off, sufficient quantities of antibodies, complement, and cytokines will diffuse to cause immune-mediated death[43]. In order for less than 1% of the pores to exhibit sizes above the desired cut-off, a broader pore size distribution necessitates a smaller nominal pore size. However, a smaller nominal pore size will result in decreased diffusion of insulin, glucose and nutrients, leading to a greater chance of nutrient starvation and poor insulin secretion kinetics. Additionally, 18 nm pore width membranes have demonstrated protection for islets when placed in a serum complement/antibody solution over a 2-week period as measured by improved glucose stimulated insulin secretion compared with unencapsulated islets[87]. Furthermore, *in vivo* studies have confirmed both short-term biocompatibility of the membranes and increased insulinoma cell viability[78]. All of these results support the potential that silicon nanoporous membranes have in providing adequate immunoisolation to encapsulated cells.

Silicon nanoporous membranes offer an additional advantage due to their small thickness of only a few microns. The diffusion of molecules through a membrane depends upon both the pore thickness and shape. Pore thickness impacts the diffusivity of all molecules equally. Pore shape, on the other hand, plays a significant role in altering diffusion in a size discriminatory manner. Ideally, the pore shape even at small thicknesses will completely block IgG yet allow unrestricted insulin and glucose flow. Therefore, the ability to manufacture silicon membranes to a thickness much smaller than that of polymer membranes, which are on the order of 100 μm thick, represents a significant advantage because of increased diffusivity of insulin and nutrients. As it turns out, a 6 μm thick, 18 nm pore width silicon nanoporous membrane has demonstrated favorable IgG diffusion characteristics[79]. For pore sizes that equally restrict IgG diffusion, the silicon membranes' reduced thickness will enable an increased diffusion of insulin and nutrients compared with thicker polymer membranes. Additionally, the thickness of a silicon membrane can be controlled more precisely than that of a polymer membrane. As a result, in addition to providing adequate immunoisolation to encapsulated cells, silicon nanoporous membranes can offer excellent transport characteristics of insulin and nutrients.

4.1.3. Disadvantages

The silicon nanoporous membrane possesses one disadvantage compared with polymer membranes as well as the alumina and titania membranes that will be discussed later. Currently, it is only feasible to manufacture silicon membranes with rectangular pores, whereby the width can be in the nanometer range but the length is limited by that which traditional etching methods allow. The width of the pore and not the length serves to restrict antibody and complement diffusion. When considering diffusion of a protein through a pore, however, the 3-dimensional conformation of the protein must be considered. IgG is a relatively flexible y-shaped molecule that can assume conformations that minimize width and extend length, allowing enhanced diffusion through a rectangular pore compared with a circular pore. This phenomena has been demonstrated by the restricted diffusion of IgG through an alumina nanoporous membrane with 75 nm diameter pores compared with a silicon nanoporous membrane with 49 nm wide pores[88]. The alumina membrane also restricted glucose diffusion more than the silicon membrane; this was likely due in part to the larger alumina membrane thickness. However, the difference in restricted glucose diffusion was less than that for IgG. Therefore, at least part of the decreased IgG diffusion was due to the circular nature of the pores in the alumina, suggesting that a circular pore can provide improved immunoisolation. While currently not easily available, technologies for creating circular nanopores in silicon may someday become commercially available by using more advanced lithographic techniques such as electron-beam or nano-imprint lithography[89]. Until then, the silicon nanoporous membrane, while extensively studied and promising, possesses the disadvantage of containing rectangular-shaped pores.

4.2. Alumina Nanoporous Membranes

Alumina nanoporous membranes, originally developed for electronics and sensor applications, take advantage of the self-organizational behavior of anodized alumina[90]. Soon after discovery of this phenomenon, a process resulting in straight nanoholes through a thin film of alumina was developed, resulting in the creation of a self-organized nanoporous alumina membrane[91]. This technology was adapted to control molecular release through a nanoporous cylindrical alumina membrane embedded within an aluminum-manganese alloy capsule[92]. The alumina membrane can also be formed on flat sheets of aluminum[93]. More recently, the alumina nanoporous membranes have demonstrated promise for cell encapsulation[88].

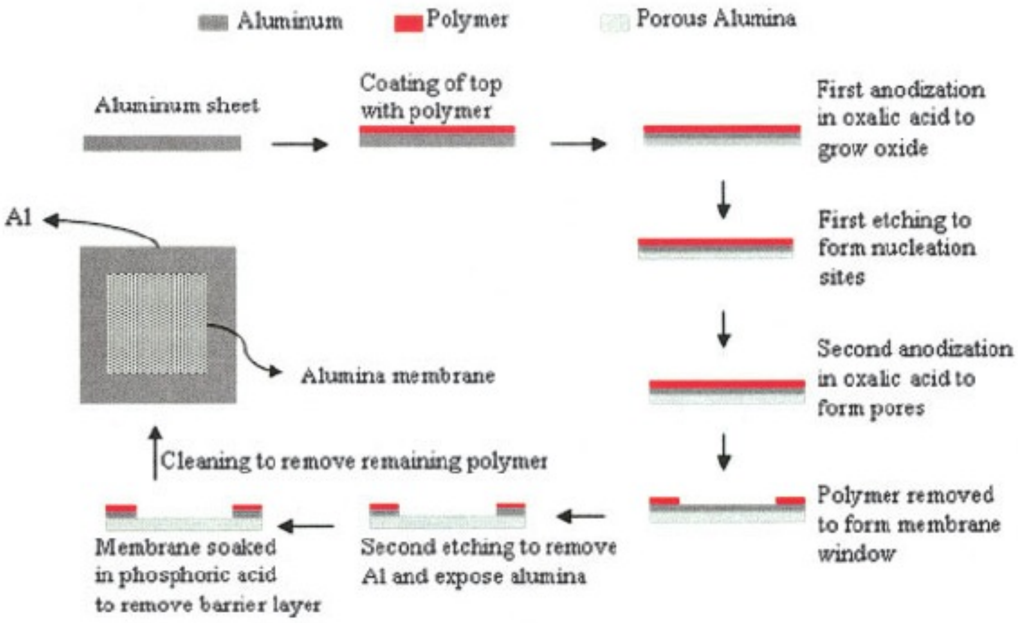

Figure 4 – Alumina Nanoporous Membrane Fabrication
Re-printed with permission from [94]

4.2.1. Preparation

Although nanoporous anodized alumina membrane fabrication depends on the application, a general process for fabrication to be incorporated into a cell encapsulation device is presented here, as adapted from previous reports (Figure 4)[88, 92, 93]. First, an aluminum alloy ($Al_{98.6}Mn_{1.2}Cu_{0.12}$) is cleaned by sonication in acetone and deionized water, and then dried with nitrogen. The next steps described are specific to a membrane formed in a cylindrical aluminum tube from the inside out. Although membranes can be created from the outside of an aluminum tube, they have demonstrated decreased mechanical strength[95]. Furthermore, when prepared from the inside, the membrane exists within a recess and is less susceptible to external damage. To achieve inner-wall membrane formation, the outside of the tube is protected by spin-coating a thin layer of polymer, typically ethyl acetate and butyl acetate (nail polish). Prior to polymer spinning, an oxalic acid anodization process produces a very thin oxide layer that allows for polymer adhesion.

After the polymer has been coated to the outside of the tube, the first anodization process involved in membrane formation occurs in 0.25 M oxalic acid using platinum as the cathode and the polymer-covered aluminum tube as the anode. This process yields a layer of alumina on the inside of the aluminum tube, where the surface is not protected by the polymer. Next, this layer of alumina is etched in a 4% (w/w) chromic acid and 8% (v/v) phosphoric acid mixture for 10 minutes at room temperature. The result is a uniform concave array of nucleation sites that is critical to achieving tight pore size distributions. The organization of nucleation sites depends on the voltage used during the first anodization step.

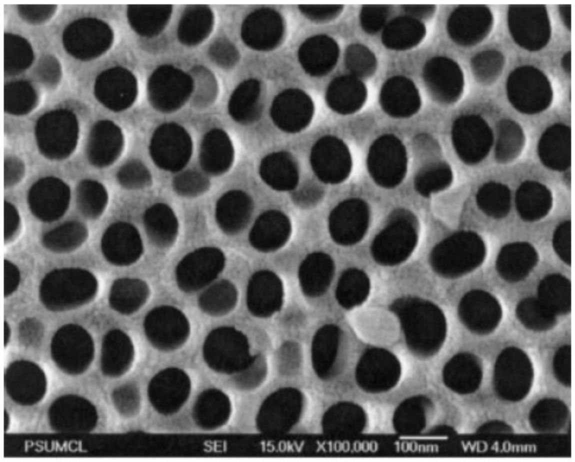

Figure 5 – SEM Micrograph of Alumina Nanoporous Membrane
Re-printed with permission from [94].

The second anodization step involved in membrane formation needs to occur at the same voltage as the first. The duration determines the membrane thickness, and the voltage determines the pore diameter with each applied volt increasing pore diameter by 1.29 nm. The resulting alumina layer will serve as the nanoporous membrane.

In order to expose the nanoporous membrane to the outside of the tube, a window-area is created in the polymer film through the selective application of acetone and a cotton swab. A 10% NaOH solution can be poured for 15 minutes to completely remove the unwanted layer of alumina that is formed during the second anodization step. Parafilm or silicone plugs are capped on the tube ends to protect the inside of the tube from the subsequent etching step. After a thorough rinse in DI water, the unprotected aluminum in the window is etched using a 10% (w/w) HCl and 0.1 M ($CuCl_2$) solution, exposing the transparent alumina membrane. Finally, a 10% (w/v) phosphoric acid solution for 1 ½ hours at room temperature removes the barrier oxide layer on the outside of the nanoporous alumina. After the parafilm or silicone plugs are removed, the result is an aluminum cylinder with a nanoporous alumina membrane window.

More recently, greater flexibility for nanoporous alumina configuration has been achieved by the use of a lithographically-produced photoresist polymer to replace the initial polymer coating[94]. Additionally, nanoporous alumina membranes have been fabricated on flat sheets[90, 91, 93, 94, 96]. As a result, alumina nanoporous membranes can be easily fabricated in a variety of configurations that could be useful as a membrane for immunoisolated cell-based drug delivery (Figure 5) [94].

4.2.2. Advantages

The alumina nanoporous membrane may overcome the limitations associated with polymer membranes discussed above, although it has not been as extensively evaluated as the silicon nanoporous membrane for this application. The pore size distribution within an alumina nanoporous membrane becomes tighter with decreasing pore diameters. A 46 nm pore created from a 40 V anodization process resulted in a 2.35 nm standard deviation, compared with a 5.48 nm standard deviation associated with a 50 V induced 58 nm pore[88]. Although these distributions are greater than those achievable with a silicon nanoporous membrane of the same pore width, they compare favorably with those of polymer membranes.

Additionally, the pore density of an alumina nanoporous membrane can exceed that for both polymer and silicon nanoporous membranes[88]. The ability to increase pore density offers a potential advantage in the design of a cell encapsulation device in the pursuit of balancing the requirements for immunoisolation and nutrient availability. If the pore diameter sufficiently impedes antibody and complement diffusion, the larger pore density will increase the diffusion of insulin, glucose, and nutrients more than it will increase the diffusion of antibodies and complement in a size specific manner. Additionally, alumina nanoporous membranes improve upon polymer membranes by offering greater control over membrane thickness.

Furthermore, the circular nature of the alumina membrane pores offers an advantage for inhibiting diffusion of the flexible IgG molecule. As a result, alumina nanoporous membranes have demonstrated greater diffusion resistance to IgG than silicon membranes[88].

Lastly, the studies evaluating the biocompatibility of alumina nanoporous membranes have been favorable. Alumina has demonstrated bio-inert characteristics in humans for certain applications, enabling its use in hip and knee replacements[97]. More recently, alumina nanoporous membranes have not caused fibroblast cytotoxicity nor complement activation *in vitro.* *In vivo* studies in the same report reveal that membrane-containing capsules are free from fibrous growth and membranes remain intact when implanted in the peritoneal cavity of rats for up to 4 weeks[98]. Tissue samples surrounding the implants do show signs of inflammation, but samples taken from tissue surrounding polyethylene glycol (PEG) coated alumina nanoporous membrane capsules exhibited less severe signs of inflammation which receded after 4 weeks[93, 99]. These results suggest that the inflammation from PEG-coated capsules occurs from the surgery itself, and not from the implanted capsule. *In vivo* studies with encapsulated cells have not yet been performed. In conclusion, the alumina nanoporous membrane offers many promising characteristics that can be applied to immunoisolated cell-based drug delivery.

4.2.3. Disadvantages

One limitation that the alumina nanoporous membrane has compared with the silicon nanoporous membrane is the thickness of the membrane. The alumina nanoporous membrane has been fabricated with thicknesses as small as 70 μm, and although thinner membranes are possible, such modifications will negatively affect membrane strength. As discussed above, a thicker membrane results in delayed diffusion of glucose information to the cells and insulin secretion to the body. The relationship between having an increased pore density but a thicker membrane needs to be more thoroughly evaluated. The advantage of increased pore density could potentially recooperate any diffusion loss due to membrane thickness in comparison to silicon nanoporous membranes. Regarding biocompatibility, it is unclear *in vivo* whether alumina nanoporous membranes can be as stable as either polymer membranes or silicon nanoporous membranes. As a result, despite promising results thus far, further evaluation will be necessary to determine whether the alumina nanoporous membrane is the ideal choice for immunoisolated cell-based drug delivery.

4.3. Titania Nanoporous Membranes

Titanium foil when anodized in certain conditions will cause the growth of an array of nanotubular titania structures from the surface[100-105]. The commercial interests driving the developing of nanotubular titania have been for photovoltaics, sensing, water photolysis, molecular filtration, and tissue engineering[103]. However, when the array of nanotubular titania is released from the substrate from which it is grown, a titania nanoporous membrane is produced that may prove useful for immunoisolated cell-based drug delivery[106].

4.3.1. Preparation

The nanotubular titania can be grown from a titanium foil in several ways. The formation of nanotubular titania described here is adapted from previous reports[100-105, 107]. First, high purity titanium foil (99.97% or higher, thickness approximately 250 μm) is degreased by sonication in acetone, ethanol, and DI water, followed by a DI water rinse and nitrogen drying. The growth of the nanotubular titania occurs with a subsequent potentiostatic anodization in a 2-cell electrode electrochemical cell connected to a dc power supply, using platinum foil as the counter electrode at room temperature. Methods of controlling nanotube diameter and length have recently been elucidated, although this research is still in its infancy and greater optimization will likely occur in the future.

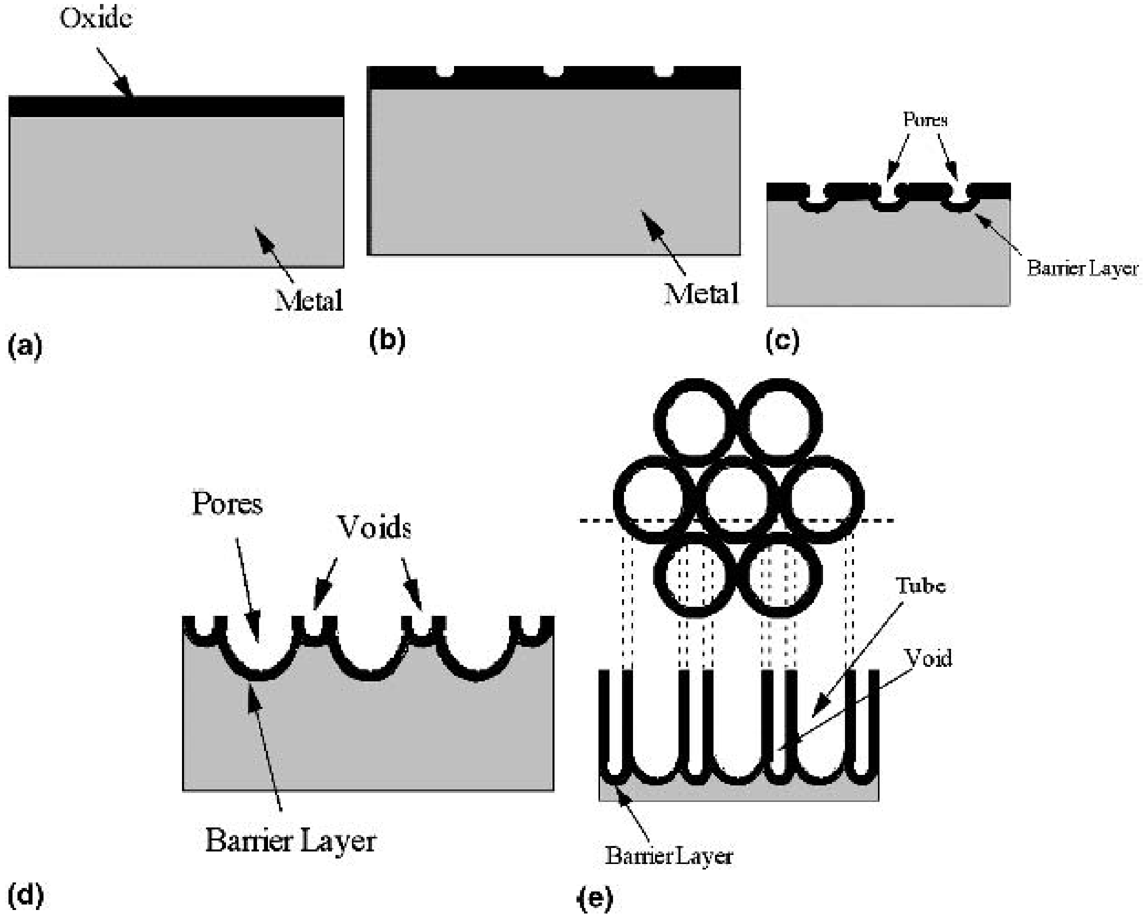

Figure 6 – Titania Nanoporous Membrane Fabrication
(a) – Oxide layer formation
(b) – Pit formation on the oxide layer
(c) – Growth of the pit into scallop-shaped pores
(d) – The metallic part between the pores undergoes oxidation and field-assisted dissolution
(e) – Fully developed nanotubes with a corresponding top view
Re-printed with permission from [107]

The first successful nanotubular titania growth occurred through anodization of titanium foil a 0.5% (w/w) HF solution[102]. Under these conditions, the nanotubular structure is formed at voltages greater than 10 V and less than 40 V. Nanotubes fabricated using this process have diameters ranging from 25-65 nm and thicknesses up to 500 nm[102, 103]. The first event in the anodization process occurs within 10 seconds when the titanium film is covered by a compact oxide film of uneven height. At 30 seconds the oxide film begins to dissolve exposing a continuous nanoporous layer without the presence of any tubular structures. After 8 minutes of continued anodization, the oxide layer is completely removed, exposing discrete emerging nanotubular structures. It has been proposed that nanotubular structure formation occurs by the following mechanism: At sufficiently high anodization voltages, the electric field strength will mobilize titanium ions from the surface in between the pores and facilitate their migration to the oxide/solution interface, resulting in the growth of tubular structures from the titanium surface[102].

Techniques to increase the length of the titania nanotubes have been elucidated. The thickness of the membrane is determined by the equilibrium between the electrochemical formation and dissolution of titania[100]. By inducing localized acidification at the pore bottom the titania dissolution rate is adjusted, allowing greater control over titania length which allows for the fabrication of membrane thicknesses up to 7 μm[103, 108]. Furthermore, the use of non-aqueous organic polar electrolytes during anodization has enabled membrane thicknesses of up to 134 μm[103]. More recently, potentiostatic anodization of titanium foil yielded membrane thicknesses of 1000 μm[106]. With a relatively simple fabrication process allowing for significant design control over the characteristics, titania membranes may prove useful for immunoisolated cell-based drug delivery (Figure 7**Error! Reference source not found.**)[103].

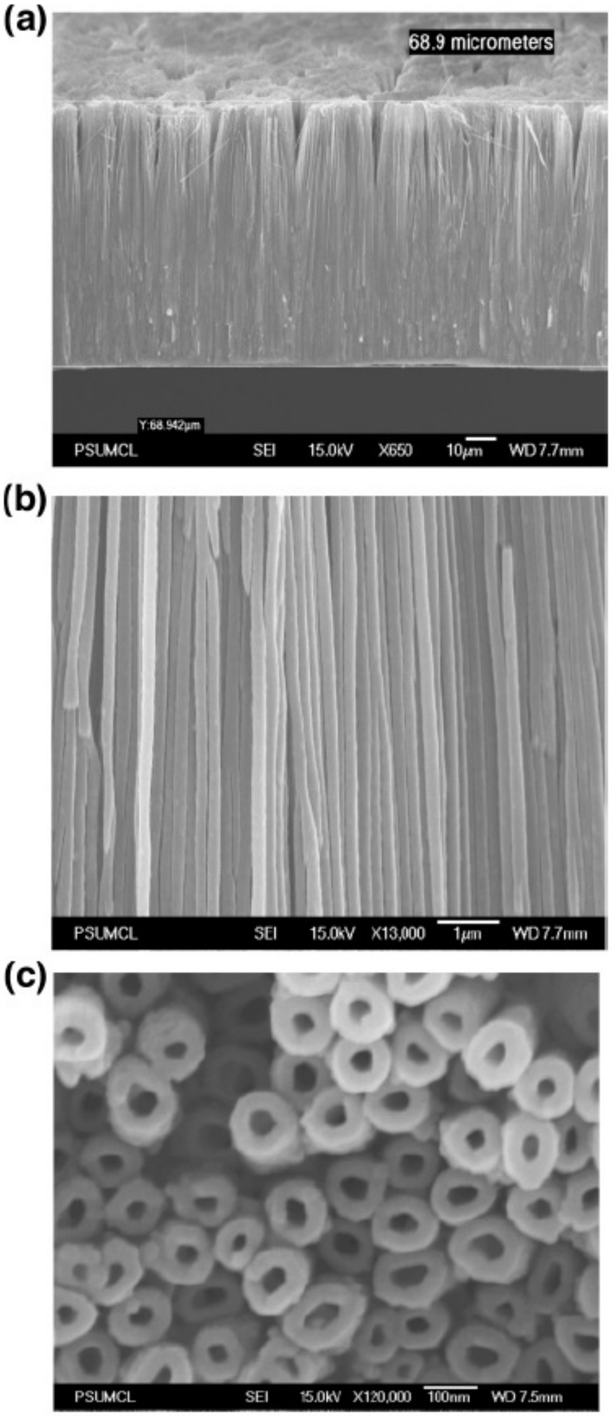

Figure 7 – FESEM Micrographs of Titania Nanoporous Membrane
(a) – Cross-section at lower magnification.
(b) – Cross-section at higher magnification.
(c) – Top-surface image
Re-printed with permission from [103].

4.3.2. Advantages

Nanoporous membranes fabricated from titanium offer a distinct advantage compared to all other membranes mentioned thus far mainly due to their widely accepted biocompatibility. Titanium has been approved by the FDA for use in many kinds of implants, including into the peritoneal cavity as exemplified by Medtronic's Isomed approval in 2000. Alumina has also been approved for some implant indications, such as the recently approved NOVATION™ Ceramic Articulation Hip System by Exactech, Inc. However, accepted implant sites for alumina do not include inside the peritoneal cavity, a promising implant location for a cell encapsulation device. While some of the polymer membranes as well as the alumina and silicon membranes currently appear biocompatible, the regulatory process associated with receiving approval for marketing those materials as biocompatible will likely be more rigorous than that for titanium.

Another distinct advantage that titania has over all other membranes discussed here is the proven ability to fabricate over a wide range of thicknesses. This design variability compares favorably with silicon nanoporous membranes which have thinner membranes as well as alumina nanoporous membranes which have thicker membranes. Control over this design variable will enable more flexibility in optimizing the diffusion requirements for immunoisolation and nutrient availability for cell encapsulation applications. It is important to note that adequate mechanical stability has not yet been evaluated for thin titania membranes. Nonetheless, if the titania membranes are patterned into a thicker titanium substrate, similar to the ridge support structure associated with thin silicon nanoporous membranes, it is feasible that titania nanoporous membranes can be made mechanically stable even at small thicknesses. Finally, for the same reasons discussed above regarding the alumina nanoporous membrane, the titania nanoporous membranes provides an advantage because of the circular nature of the pores and the increased achievable pore density. In conclusion, the titania nanoporous membranes are an excellent choice for incorporation into cell-based drug delivery devices.

4.3.3. Disadvantages

The titania nanoporous membrane development is still in its infancy. Many qualities necessary for the successful application of titania nanoporous membranes to cell encapsulation have not yet been evaluated, such as durability *in vivo*, immunoisolation characteristics, compatibility with implanted cells, and pore size distribution. It is premature to comment on the disadvantages of the titania membrane until further evaluation and fabrication optimization has been performed.

Membrane Material	Advantages	Disadvantages
Polymer	1. Circular pore geometry 2. High pore density 3. Biocompatible 4. Inexpensive	1. Broad pore size distribution 2. Broad thickness distribution 3. Thick membrane
Silicon	1. Tight pore size distribution 2. Tight thickness distribution 3. Proven fabrication of channel widths as small as 10 nm. 4. Thin membrane 5. Biocompatible	1. Low pore density 2. Rectangular pores 3. Expensive
Alumina	1. Tight pore size distribution 2. Tight thickness distribution 3. Circular pore geometry 4. Inexpensive	1. Thick membrane 2. Fabrication of pore diameters as small as 10 nm has not been proven 3. Biocompatibility unclear
Titania	1. Tight pore size distribution 2. Tight thickness distribution 3. Circular pore geometry 4. Biocompatible 5. Material is FDA approved for implant into the peritoneal cavity 6. Inexpensive	1. A thin membrane has not yet been proven to be adequately mechanically robust 2. Fabrication of pore diameters as small as 10 nm has not been proven

Table 2 – Advantages and Disadvantages of Polymer and Inorganic Nanoporous Membranes

5. Conclusion

The field of cell-based drug delivery has come a long way towards overcoming the challenges that have limited successful clinical treatments. Several challenges remain, however, including attaining a sufficiently available cell supply, means of maintaining cell viability for a therapeutically useful duration, and minimizing the delay of glucose-stimulated insulin secretion. Immunosuppressed cell transplantation does not adequately overcome the cell supply issue and leaves the patient with undesirable complications. Immunoisolated cell transplantation via intravascular transplantation chambers has not overcome the coagulation issues associated with graft failure. Microencapsulated cell transplantation is the only immunoisolated cell-based drug delivery approach being evaluated in clinical trials. However, all microcapsules comprise a polymer membrane with inherent limitations including broad pore size distributions, thick membrane walls, and interdependency of membrane and cell matrix design. Extravascular transplantation chambers, on the other hand, allow both for the independent design of the cell matrix and membrane as well as the incorporation of inorganic nanoporous membranes. Currently, inorganic nanoporous membranes can be fabricated from silicon, alumina, and titania. Additionally, recent research has elucidated new inorganic nanoporous materials that could someday be investigated for use in an extravascular transplantation chamber[109, 110]. The inorganic nanoporous membranes possess pore size distributions much tighter than that of polymer membranes, providing a better chance at appropriately balancing the requirements for immunoisolation and nutrient availability. Inorganic nanoporous membranes also have displayed promising biocompatibility characteristics as well as allow for the cell matrix environment to be independently designed from the membrane. Additionally, the silicon and titania nanoporous membranes can comprise smaller and more accurate thicknesses, offering improved blood-glucose control by decreasing the delay with which insulin regulates the blood-glucose level. Therefore, the inorganic nanoporous membrane-enclosed extravascular transplantation chamber offers great promise for developing a widely-available treatment for insulin dependent diabetes mellitus.

Chapter 3 – Methods

Materials

The following materials and chemicals were used as received: microscope cover glass (12 mm circles, 1 ox; Fisher Scientific, Pittsburgh, PA), 3” silicon <111> p-type wafer (Addison Engineering, San Jose, CA), 3-aminopropyltriethoxysilane (APTES; Sigma-Aldrich, St. Louis, MO), glutaraldehyde (solution grade I 50%; Sigma-Aldrich, St. Louis, MO), SU-8 2010 and SU-8 developer (Microchem, Newton, MA), Sylgard 184 silicone elastomer kit (base and cross-linker; Dow Corning, Midland, MI), methoxypoly(ethylene glycol) amine (mPEG-amine, MW 5000; Fluka, Buchs, Switzerland), sodium cyanoborohydride (Sigma-Aldrich, St. Louis, MO), ethanol (A.C.S. Reagent >99.5%; Sigma-Aldrich, Sheboygan Falls, WI), isopropanol (IPA; VWR International, Westchester, PA), ethanol (A.C.S. Reagent; Sigma-Aldrich, Sheboygan Falls, WI), fluorescein isothiocyanate-bovine serum albumin (FITC-BSA; Sigma-Aldrich, St. Louis, MO), mouse laminin (1 mg/mL; Invitrogen, Carlsbad, CA), fetal bovine serum (FBS; Hyclone Laboratories, South Logan, UT), 2-mercaptoethanol (Sigma-Aldrich, France), sodium-pyruvate, penicillin/streptomycin, RPMI-1640 with HEPES, 0.05% trypsin-EDTA and l-glutamine (UCSF Cell Culture Facility, San Francisco, CA), goat serum (Sigma-Aldirch, St. Louis, MO), dipotassium phosphate (Sigma-Aldrich, Japan), sodium chloride (Sigma-Aldrich, St. Louis, MO), Tween 20 (Sigma-Aldrich, St. Louis, MO), mouse monoclonal anti-insulin IgG (SPM139, Santa Cruz Biotech, Santa Cruz, CA), rabbit anti-C-Peptide (#4593, Cell Signaling, Boston, MA), donkey anti-mouse IgG Alexa Fluor 488 (Invitrogen, Eugene, OR), goat anti-rabbit IgG Alexa Fluor 633 (Invitrogen, Eugene, OR), Alexa Fluor 568 phalloidin (Invitrogen, Eugene, OR), and SlowFade Gold antifade reagent with DAPI (Invitrogen, Eugene, OR).

Cleaning of glass cover slips

Glass cover slips were sonicated in a 70:30 ethanol:Milli-Q water (Millipore, Bedford MA) solution for 10 minutes, then dried with nitrogen. Following this, cover slips were cleaned in oxygen plasma at 175-200 W and 0.5 mTorrr for 30 seconds (Plasmaline, TCGAL Corporation).

Preparation of aldehyde-terminated glass cover slips

Clean dry plasma-treated glass cover slips were silanized in a freshly prepared solution of APTES (2% v/v) in 95:5 ethanol:Milli-Q water for 30 minutes, followed by 10 dips in a freshly prepared solution of 70:30 ethanol:Milli-Q water (Milli-Q water only for Chapter 4). The cover slips were then submerged in a second freshly prepared solution of 70:30 ethanol:Milli-Q water (Milli-Q water only for Chapter 4) and sonicated for 20 seconds. Cover slips were then dried with nitrogen before placement on a glass petri dish on a hot plate set to 120°C for 1 hour. The cover slips were then placed in a vacuum chamber at room temperature for at least 24 hours before use. The amine-terminated cover slips were sonicated for 10 minutes in 70:30 ethanol:Milli-Q (Milli-Q water only for Chapter 4) water before incubation for 1 hour at room temperature in 10% glutaraldehyde in phosphate-buffered saline (PBS). The aldehyde-terminated cover slips were sonicated again for 10 minutes in 70:30 ethanol:Milli-Q water and then dried with a stream of N_2.

Preparation of PDMS stamp for microcontact printing of laminin

PDMS stamps were fabricated through a multi-step process that uses photolithography and micropatterning techniques. Firstly, a negative photoresist SU-8 2010 was spin cast onto a silicon wafer at 2000 rpm for 1 minute yielding a thickness of approximately 13 μm as determined by profilometry (Ambios XP-2, Ambiostech, Santa Cruz, CA). SU-8 films were pre-baked on a hot-plate at 95°C for 3 minutes. SU-8 films were subsequently patterned by exposure to UV light through a transparency mask defining the desired features to guide cell patterning. Patterned SU-8 films were post-baked at 95°C for 4 minutes and then immersed in SU-8 developer for 2 minutes to remove un-crosslinked SU-8. Wafers were subsequently rinsed with SU-8 developer, IPA, and dried with a stream of N_2. Lastly, the wafers were baked at 150°C for 15-20 minutes.

An inverse pattern of the silicon wafer was prepared with PDMS. The base and curing agent were mixed at a 10:1 by mass and deposited onto the micropatterned wafers. The PDMS film was then de-gassed under vacuum for 1-2 hours to remove all bubbles, and then cured at 70°C for at least 2 hours at atmospheric pressure. Once cured, the PDMS was cut and peeled from the silicon master.

Covalent attachment of laminin by microcontact printing

Following exposure of PDMS stamps to O_2 plasma for 30 seconds at 175-200 W and 0.5 mTorr, the surface was covered with a solution of 200 μg/mL laminin in PBS and incubated for 30 minutes at room temperature. A Kimwipe was used to wick away excess solution before drying the remaining liquid with N_2. Immediately after drying, the PDMS stamps were carefully placed on the aldehyde-terminated cover slip with a 10 g weight for 30 minutes at room temperature. The stamps were then carefully peeled off, leaving printed laminin.

Covalent attachment of PEG

After PDMS stamping of laminin on aldehyde-terminated cover slips, the cover slips were covered with 25 μL of 3 mM mPEG-amine in methanol and excess sodium cyanoborohydride (>8 mM) to quench unreacted aldehyde groups (sodium cyanoborohydride was exposed separately for 1 hour after >12 hours of exposure to mPEG-amine for Chapter 5 only. This two-step reaction enabled greater pattern uniformity). Cover slips were incubated overnight (>12 hours) in a chemical fume hood due to hydrogen cyanide gas production, subsequently sonicated for 5 minutes in methanol, and lastly rinsed with methanol before being dried with N_2.

Fluorescent imaging of cover slips

Cover slips with printed laminin were exposed to a 50 μg/mL (20 μg/mL for Chapter 4) fluorescein isothiocyanate-bovine serum albumin (FITC-BSA) solution before PEG functionalization for 20 minutes, sonicated in PBS for 5 minutes, rinsed with Milli-

Q water, and dried with nitrogen before images were taken with a wide-field fluorescent microscope (Olympus BX60).

Cell culture and seeding onto microcontact printed slides

INS-1 (832/13) cells were cultured with RPMI-1640 medium supplemented with 25 mM HEPES, 10% FBS, sodium-pyruvate, penicillin, streptomycin, and 2-mercaptoethanol [111]. Cells were trypsinized in a 0.05% trypsin–EDTA solution, re-suspended in the above media and 1 mL of the cell solution was seeded onto the patterned cover slips within a 12-well plate. The cells were cultured in an incubator at 37°C with 5% CO_2.

Insulin Secretion Studies

After cells have achieved confluency on the patterns, the culture medium from the wells containing patterned cover slips was removed and replaced with culture medium containing 5 mM glucose. 18-20 hours after exposure to 5 mM glucose the cells were rinsed with a HEPES balanced salt solution described elsewhere[111] with 0.2% essentially fatty acid free BSA and 0 mM glucose. Each cover slip was rinsed with 1 mL of solution. After rinsing, each cover glass was incubated in 1 mL of the same solution for 2 hours. After the incubation period passed, all of the medium was removed and replaced either with the same 0 mM glucose solution to simulate basal insulin secretion conditions or a 15 mM glucose version of the solution created by adding D-glucose in the appropriate amount to simulate glucose stimulated insulin secretion conditions. After two hours, the solution was mixed thoroughly and sampled for later analysis.

Fixing of cells for imaging

Cells were fixed with a solution of 3.7% formaldehyde in PBS solution for 15 minutes. After thoroughly rinsing with PBS, the cells were permeabilized with 0.5% Triton X-100 solution for 15 minutes and rinsed again with PBS.

Immunocytochemistry

After fixing and permeabilizing, the cells were immunostained for insulin, c-peptide and/or GAPDH. Cover slips were placed on top of 20 μL drops of solution containing 1 μg/mL of rabbit anti-c-peptide and either 2 μg/mL mouse monoclonal anti-insulin or 2 μg/mL mouse monoclonal anti-GAPDH with 5% goat serum in buffer (13 mM dipotassium phosphate, 150 mM sodium chloride and 0.2% Tween 20, pH 7.5; same buffer used as follows unless otherwise specified). The cover slips were left on the drops overnight at 4°C. The cover slips were then rinsed thoroughly with buffer prior to placement on another 20 μL drop of solution containing 10 μg/mL of both donkey anti-mouse IgG Alexa Fluor 488 and goat anti-rabbit IgG Alexa Fluor 633 for 1 hour at room temperature. The cells were rinsed with buffer thoroughly before staining the actin cytoskeleton with Alexa Flour 568 Phalloidin (165 nM in PBS) for 30 minutes, followed by a second PBS rinse. SlowFade Gold antifade reagent with DAPI was deposited (3 μL) onto a microscope slide and then a cover glass was placed on top of the drop. Nail polish was used to adhere the cover glass to the microscope slide.

Spinning disk confocal microscopy (Nikon Eclipse Ti-E motorized inverted microscope with Yokogawa CS22 Spinning Disk Confocal from Solamere Technology Group, Acquisition with Micro-Manager) was used to visualize the clusters. The cell border of 0.25 μm-thick z-stacks were defined by the phalloidin and image intensity data within the confines of this volume was used for analysis using NIS-Elements. Lack of significant photobleaching was confirmed by evaluating 5 subsequent identical images for intensity differences at the laser power settings used.

Measurement of Insulin Expression

Insulin messenger ribonucleic acid (mRNA) expression was evaluated using an Applied Biosystems StepOnePlus Real-Time Polymerase Chain Reaction (PCR) System. Cells were lysed with TRIzol (Invitrogen) and total RNA was extracted with chloroform (Sigma A.C.S. grade >99.8%). cDNA was synthesize with iScript cDNA Synthesis Kit (Biorad). Reverse transcriptase-PCR (RT-PCR) was performed using SYBR green FAST mix (Applied Biosystems). The expression level of insulin 2 was normalized against β-actin using a standard curve method (See **Error! Reference source not found.** for primers), and the results were analyzed with the Version 2.0 software.

Measurement of Insulin Secretion

An ultrasensitive rat insulin ELISA (Mercodia) was used to measure the insulin content of each sample. Briefly, 25 μL of insulin standards or unknown samples were placed with 100 μL of peroxidase-conjugated anti-insulin antibodies in microwells coated with anti-insulin antibodies and incubated for 2 hours on a shaker at ~700 rpm.

A washing step removed unbound enzyme-labeled antibody, and then 200 mL of 3,3',5,5'-tetramethylbenzidine was added to each well. 50 μL of sulfuric acid was added to each well to stop the reaction after color had developed. The absorbance value at 450 nm which correlates to the amount of bound insulin was measured using a spectrophotometer.

Surface Characterization

The static water contact angle of the prepared cover slips at each surface chemistry stage were measured as the average of three independently prepared slides using a Tantec model CAM-Micro goniometer. Static water contact angle measurements are displayed as averages ± equipment measurement error, which was larger than the standard deviations. All IR spectra were obtained using a Nicolet Nexus (Thermo Electron Corporation, Hayward, CA). Germanium Attenuated Total Reflection Fourier Transform Infrared Spectroscopy (GATR-FTIR) with wire-grid polarizer was detected with a deuterated triglycine sulfate detector (DTGS) and analyzed using OMNIC version 7.0 software. Spectra were obtained in the range 800-3200 cm^{-1} at a resolution of 8 cm^{-1}. All spectra were acquired with an atmospheric background. Chemical characterization was performed using a Surface Science Instruments S-Probe monochromatized X-ray photoelectron spectrometer (XPS), with a Al(k-α) radiation (1486 eV) probe.

Coating of cover slips

Clean dry plasma-treated glass cover slips were incubated with 20 μg/ml Matrigel (BD Biosciences), mouse laminin (Invitrogen), porcine gelatin (Sigma), rat tail collagen I

(Sigma) or fibronectin (Gibco) for 30 min. Cover slips were then sonicated in phosphate-buffered saline (PBS) for 5 min, rinsed with Milli-Q water and dried with N2.

hESC culture and differentiation

Undifferentiated CyT49 hESC were grown as described previously[19] with minor modifications to the original protocol. The day before passaging hESCs, mitomycin-C-treated mouse embryonic fibroblast feeder cells (MEFs; Millipore Specialty Media) were plated onto gelatin-coated (Sigma-Aldrich) 60 mm dishes (Falcon) at a density of 5000 cells/cm2. Biweekly, the hESCs were passaged enzymatically with Accutase (Esgro) according to the manufacturer's protocol, and seeded at a density of 50000-100000 cells/cm2. Daily, the hESCs received fresh hESC medium that was supplemented with 10 ng/ml FGF2 (R&D Systems), but did not contain activin A. Differentiation was conducted in 12-well plates (Falcon) that contained the microcontact-printed glass cover slips (Fisherbrand) described above. Prior to differentiation, the hESCs were seeded at a density of 25000 cells/cm2 in MEF-conditioned hESC medium supplemented with 10 ng/ml FGF2, and washed once with PBS 72 h post passaging. Differentiation into definitive endoderm was carried out using DMEM/F12 that was conditioned by CHO cells secreting recombinant activin A[112]. For the first 24 h, this conditioned medium was supplemented with 2 mg/ml bovine serum albumin fraction V (BSA-V; Sigma), 0.5×N2 and 0.5×B27 medim supplements (Invitrogen), 50 ng/ml Wnt3a (R&D Systems), and 100 nM wortmannin (Sigma). Subsequently, the differentiating cells were incubated for an additional 48 hours in the medium described above, without wortmannin and

Wnt3a. To generate primitive gut tube-like tissue, the cells were incubated for 72 hours in RPMI 1640 (Invitrogen) with 2% (vol/vol) FBS (VWR Hyclone) and 50 ng/ml KGF. For the generation of posterior foregut tissue, cells at the primitive gut tube stage were incubated for 72 hours in DMEM/F12 with 1×N2, 300 nM (-)-indolactam V (Calbiochem), 2 mg/ml BSA-V, and 10 ng/ml FGF10 (R&D Systems). To generate pancreatic endoderm, the posterior foregut cells were incubated for 72 hours in DMEM (Invitrogen) with 1×B27. Where indicated, the definitive endoderm-like aggregates were dislodged from the microcontact-printed cover slips by pipetting, transferred to low-attachment 12-well plates (Falcon) to keep them in suspension, and subjected to the differentiation procedure described above. All media were refreshed daily.

Immunofluorescence microscopy (Chapter 6)

Cells were fixed and stained as described previously[113], using the primary antibodies mouse anti-OCT4 (1:200; Santa Cruz), goat anti-SOX17 (1:1000, R&D Systems), rabbit anti-HNF1b (1:100, Santa Cruz), mouse anti-ALB (1:500, Sigma-Aldrich), goat anti-PDX1 (1:10000, Abcam), mouse anti-NKX6.1 (1:50, Hybridoma F55A10-c), in combination with the secondary antibodies FITC-conjugated donkey anti-mouse, Cy3-conjugated donkey anti-goat, FITC-conjugated donkey anti-rabbit (all 1:200, Jackson ImmunoResearch Inc), Alexa Fluor 647-conjugated donkey anti-mouse (1:200, Invitrogen Life Technologies). The cells were counter-stained with DAPI (Roche) or ToPro3 (Invitrogen Life Technologies) and mounted in VectaShield (Vector Laboratories Inc). Images were captured using SL and SP2 confocal laser scanning microscopes (Leica

Microsystems), and processed with Paint Shop Pro XI (Corel)) and ImageJ 1.43u to reconstruct the three-dimensional (3-D) image of the cluster.

Flow cytometry

Cells were trypsinized and fixed as described [11], and permeabilized for 15 min in PBS with 0.4% Triton X-100 and 1% BSA (Sigma-Aldrich). Then, the cells were stained with the primary and secondary antibodies indicated above, and sorted using an LSR II Flow cytometer (BD Biosciences). The data were obtained with FACSDiva 6.1.3 (BD Biosciences), and processed with WinMDI 2.9.

Quantitative real-time PCR (Chapter 6)

hESCs and definitive endoderm cells were collected from 12-well plates (Falcon). RNA was extracted using TRIzol reagent (Invitrogen). Concentrations of total RNA were measured using the NanoDrop ND-1000 Spectrophotometer (NanoDrop Technologies Inc), and 300-500 ng of this RNA was used in a reverse transcription (RT) reaction with a Superscript III cDNA Synthesis kit (Invitrogen). SYBR Green master mix (Qiagen) RT-PCR reactions were set up in duplicate using 300-500 ng cDNA with 300 nM forward and reverse primers summarized in Table 1 in an Applied Biosystems 7900. Relative expression values were normalized relative to the housekeeping gene GUSB, and the values from the definitive endoderm samples were compared to those of the undifferentiated hESCs.

Table 1. RT-PCR Primers.

OCT4	Forward: 5′-TGG GCT CGA GAA TGT G-3′ Reverse: 5′-GCA TAG TCG CTG CTT GAT CG-3′
SOX7	Forward: 5′-ACG CCG AGC TCA GCA AGA T-3′ Reverse: 5′-TCC ACG TAC GGC CTC TTC TG-3′
SOX17	Forward: 5′-GGC GCA CGA GAA TCC AGA-3′ Reverse: 5′-CCA CGA CTT GCC CAG CAT-3′
FOXA2	Forward: 5′-GGG AGC GGT GAA GAT GGA-3′ Reverse: 5′-TCA TGT TGC TCA CGG AGG AGT A-3′
GUSB	Forward: 5′-ACG CAG AAA ATA TGT GGT TGG A-3′ Reverse: 5′-GCA CTC TCG TCG GTG ACT GTT-3′
INSULIN 2	Forward: 5′-GAA GTG GAG GAC CCA CAA GT-3′ Reverse: 5′-AGT GCC AAG GTC TGA AGG TC-3′
β-ACTIN	Forward: 5′-CAA CCG TGA AAA GAT GAC CCA GA-3′ Reverse: 5′-ACG ACC AGA GGC ATA CAG GGA C-3′

Chapter 4 – Patterning of Mono and Multi-layered Pancreatic β-cell Clusters

Abstract

Cluster-size dependent behavior of pancreatic β-cells has direct implications in islet transplantation therapy for type I diabetes treatment. Control over the cluster-size enables evaluation of cluster-size dependent function, ultimately leading to the production of β-cell clusters with improved transplant efficacy. This work for the first time demonstrates the use of microcontact printing-based cell patterning of discrete two and three-dimensional clusters of pancreatic β-cells. Both single and multiple cell layers are confined to a 2D area by attaching to patterns of covalently linked laminin and not adhering to surrounding polyethylene glycol. Cell clusters were successfully formed within 24 hours for printed patterns in the range 40-120 μm, and simple modulation of the initial cell seeding density leads to the formation of multiple cell layers. Semi-quantitative fluorescence microscopy, x-ray photoelectron spectroscopy, and fourier-transform infrared spectroscopy were used to extensively characterize the surface chemistry. This technique offers unprecedented control over cell cluster shape and size and provides an effective tool to study not only the cluster-size dependent behavior of pancreatic β-cells, but also has potential applicability to numerous other cell lines.

1. Introduction

Type I diabetes is characterized by the absence of insulin production from the pancreas. The current standard of care requires frequent monitoring of a patient's blood-glucose level by measuring blood obtained from a finger-prick. Current technologies for delivering an appropriate amount of insulin also depend on diligent patient compliance. There have been significant efforts towards improving therapy by transplanting islets that comprise a majority of functional glucose-responsive insulin-secreting pancreatic β-cells[114]. Since the Edmonton protocol showed 7 islet transplant recipients with insulin independence for a full year in 1999[16], numerous centers now offer this therapy to patients with severe type I diabetes. Approximately 80% of patients receiving this treatment achieve insulin independence within the first year[115]. However, long-term clinical success is limited and numerous challenges remain before this therapy can be applied to a larger population[114]. In particular, the size-dependent behavior of pancreatic β-cell transplanted clusters is a major challenge[116], as islets lose their vasculature upon explantation and do not sufficiently revascularize after transplantation[117]. As a result, cells on the inside of larger clusters are typically nutrient-deprived and insulin secretion declines as the size of an islet exceeds 50-100 μm[116].

It is well established that the sensitivity of pancreatic β-cells to secrete insulin in response to glucose stimulation is highly dependent on cell-cell contact. For example, β-cell pairs and monolayers have a greater glucose stimulated insulin secretion (GSIS) response than single β-cells[118, 119], and 3-D β-cell clusters secrete greater insulin than β-cell monolayers[120]. Mechanistic evaluations have revealed the importance of junction proteins, such as Cx36[121, 122] and E-cadherins[119], on insulin production from β-cells. One β-cell model predicts a lower limit of four β-cells in contact with each other to achieve coordinated insulin secretion[123]. These studies therefore emphasize the need to optimize β-cell cluster size to maintain cell function and maximize cell response.

Immobilization of cell-adhesive proteins on a surface to defined areas can be achieved through a process called microcontact printing and was originally developed by the Whitesides group in 1994[124]. Since then, the process has successfully produced cell patterns from a variety of cell types including endothelial cells[125, 126], fibroblasts[127], and HeLA cells[128]. Various surface chemistry techniques have been developed on gold[124-126, 129, 130], silver[125], silicon oxide/glass[130], and applicable to multiple substrates[131], where the chemistry plays a critical role in cell adhesion. A tool that achieves controlled and reproducible 3D cell clusters of arbitrary size can have significant impact in the understanding of pancreatic β-cell function. While the hanging-drop technique has enabled the creation of 3D cell clusters of a specific size[132], the creation of varied 3D cell cluster sizes has not been shown.

This study develops and characterizes an approach for pancreatic β-cell patterning in the range 40-120 μm by utilizing microcontact printing of proteins. The rat insulinoma cell line 832/13 was used because it exhibits glucose stimulated insulin secretion at physiologically relevant glucose concentrations[111]. Here, the cell-adhesive protein laminin was printed as it is a common ligand for α3β1 integrins that are expressed by 832/13 cells as well as primary β-cells[133]. Variations of cell seeding densities were used to promote the formation of multilayered cell clusters, allowing the effect of cluster size to be studied while maintaining constant area of attachment. The approach presented here demonstrates a method that effectively controls cluster size, potentially providing an avenue to better understand pancreatic β-cell behavior and function that has major implications for islet transplantation therapy.

2. Results and Discussion

2.1. Covalent attachment of laminin and PEG

Patterning of laminin on glass cover slips through microcontact printing is presented in Figure 8. Briefly, patterned SU-8 (Figure 8A-C) on silicon is used as a mold to create a polydimethylsiloxane (PDMS) stamp that adsorbs a monolayer of laminin solution (Figure 8D & E) and then stamped and transferred onto a functionalized glass cover slip (Figure 8F & G). This method creates discrete regions of protein defined by the mask used in the lithographic process. Aldehyde linker chemistry is employed to covalently attach laminin to the glass cover slip as represented in Figure 9. Quenching of exposed non-printed aldehydes was achieved using mPEG-amine. Sodium cyanoborohydride is then used to reduce the Schiff base formed between the amine and the aldehyde into a stable imine bond[134].

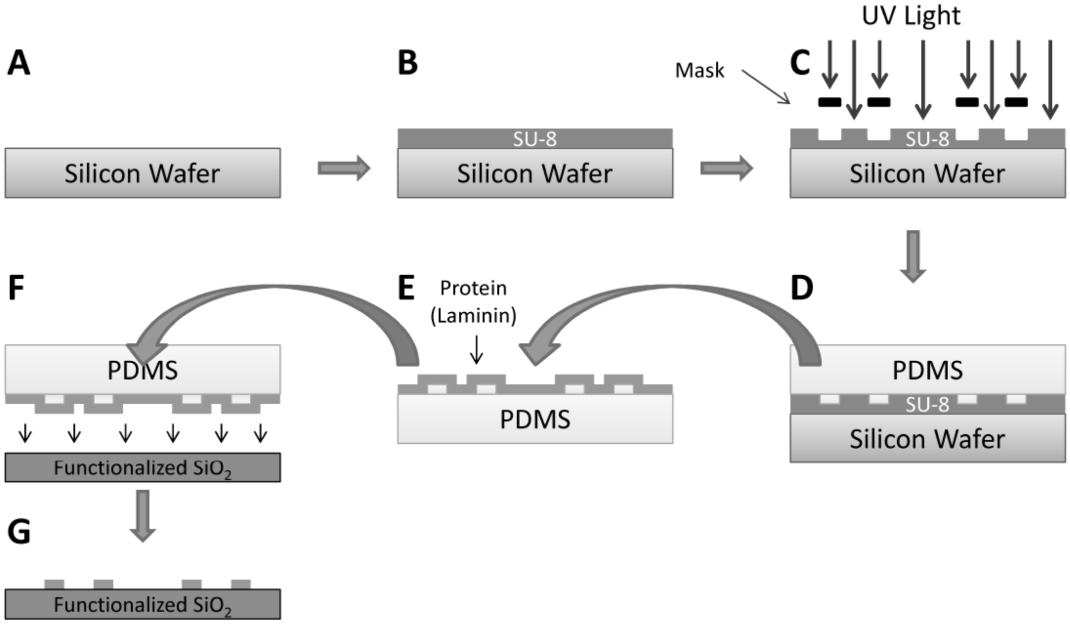

Figure 8 – Microcontact Printing

A clean silicon wafer (A) is spin-cast with SU-8 (B) followed by selective photopolymerization of SU-8 by UV light (C). PDMS is deposited and cured on top of the SU-8 microfabricated mold (D), is subsequently peeled off, and the patterned PDMS is incubated in a protein solution (E). Dried protein solution on the PDMS is then stamped (F) and transferred to a functionalized glass cover slip (G).

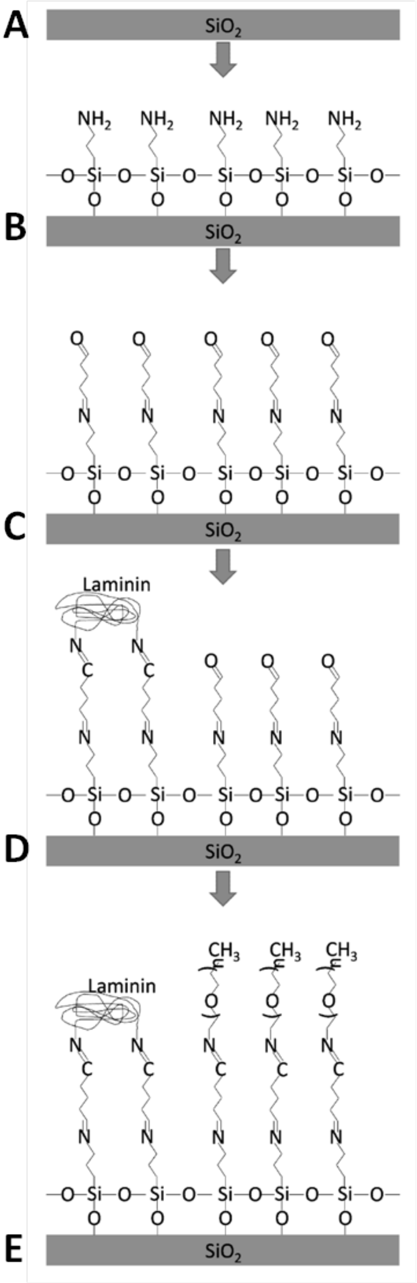

Figure 9 – Covalent Attachment of Laminin and PEG

Glass cover slip is cleaned with oxygen plasma (A), and APTES is deposited to form an exposed amine (B). Glutaraldehyde incubation results in an exposed aldehyde (C). Amines located within the amino acids of the printed protein bind to the exposed aldehydes (D) and mPEG-amine passifies the remaining aldehydes after sodium cyanoborohydride reduction reduces the Schiff bases to stable imines (E).

Characterization of covalent attachment of laminin patterns and PEG were performed on functionalized glass cover slips for contact angle and cell attachment and on silicon wafers for XPS and FTIR characterization. Table 1 shows static water contact angles for each functionalization step. Oxygen plasma thoroughly cleaned the substrates as verified by excellent hydrophilicity. The surface increased in hydrophobicity after APTES deposition and then had greater hydrophilicity after PEG deposition, both consistent with what has been reported elsewhere[130, 135].

Layer	θ_{sta} [°]
O_2 Plasma Cleaned	<5
APTES	40 ± 2
Glutaraldehyde	50 ± 2
Printed Laminin	57 ± 2
PEG	26 ± 2

Table 3 – Static water contact angles for functionalized glass cover slips

Typical FTIR spectra of the step-wise surface functionalization are shown in Figure 10. Upon exposure to an oxygen plasma (Figure 10A), the silicon surface shows characteristic peaks at 1050 cm^{-1} and 840 cm^{-1}, which correspond to the expected Si-O stretching and bending, respectively. Incubation of the silicon surface with APTES (Figure 10B) resulted in the appearance of a small peak corresponding to N-H bending vibration at 1650 cm^{-1} and a larger peak at 1157 cm^{-1} related to a C-N stretch. Subsequent addition of glutaraldehyde (Figure 10C) resulted in an increase in the C=O stretching vibration and the disappearance of the small N-H bending vibration. This result is consistent with the reaction between glutaraldehyde and an amine and the addition of a carbonyl functional group.

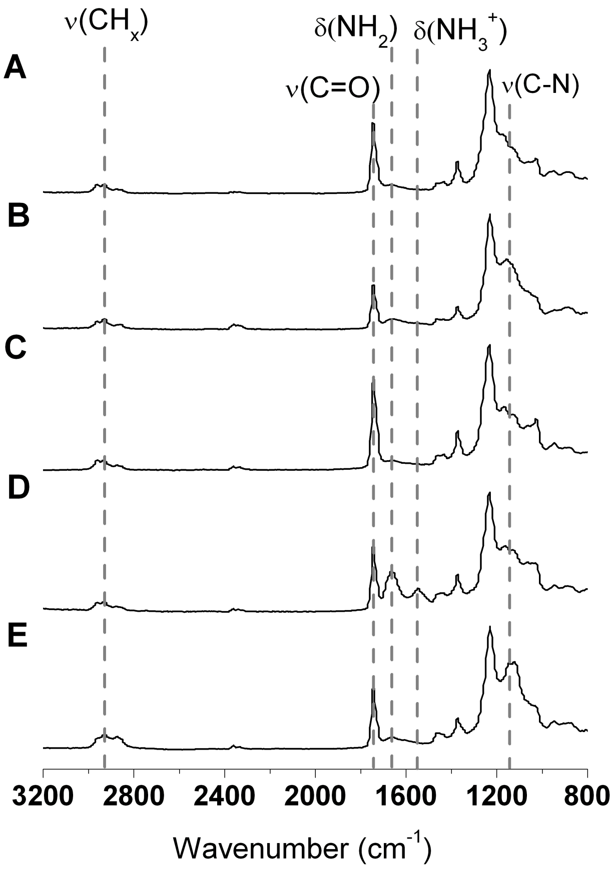

Figure 10 – FTIR Spectra of Functionalized Cover Slips
FTIR spectra of (A) O_2 plasma treated Si, (B) APTES derivatized Si, (C) glutaraldehyde modified, (D) laminin printed, and (E) PEG functionalized.

In Figure 10D the peaks at 1650 cm^{-1} and 1540 cm^{-1} are attributed to NH_2 and NH_3^+ bending vibrations, respectively. These two distinctive peaks are due to the large presence of amine groups within the protein laminin. Incubation of the glutaraldehyde-modified surface with mPEG-amine and subsequent reduction with sodium cyanoborohydride resulted in the appearance of a strong C-N peak, characteristic of

Schiff base reduction. For all spectra, C-H stretching vibrations at 2850-2960 and bending vibrations at 1460 cm^{-1} are observed. These peaks are attributed to adsorbed adventitious carbon species during sample transport and storage, in addition to the surface functionalization that contains CH, CH_2 and CH_3 bonds.

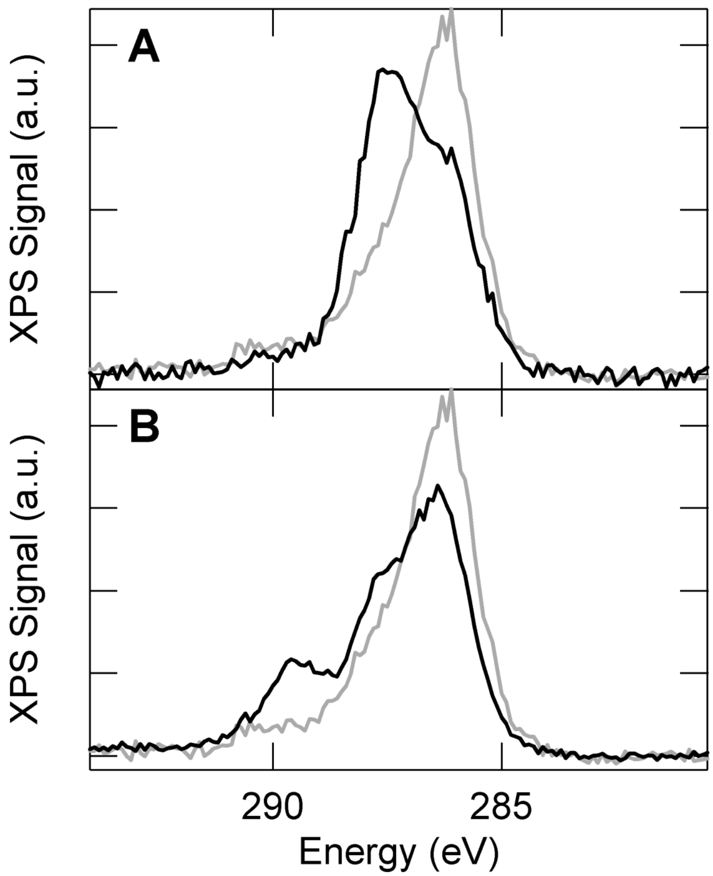

Figure 11 – XPS of Functionalized Cover Slips

X-ray photoelectron spectra of the C 1s region for surfaces functionalized with APTES and glutaraldehyde (light), APTES, glutaraldehyde and mPEG-amine (dark, A), and APTES, glutaraldehyde and laminin (dark, B)

To further characterize the relative chemical composition of the surfaces, the carbon 1s peak was monitored using x-ray photoelectron spectroscopy (XPS) (Figure 11).

For samples coated with glutaraldehyde functionalized APTES, a primary peak centered at 286 eV can be attributed to carbon-carbon bonding of the primarily alkyl coating. Compared to an expected energy of ~284 eV for carbon-carbon bonding, the measured spectra is slightly shifted to higher energy due to charging. This effect was consistent amongst all samples and can be attributed to the poor conductivity of these substrates. A low intensity tail at higher energy (~290 eV) is also observed and likely corresponds to carbon-nitrogen bonding associated with APTES.

When evaluating PEG and laminin functionalization, it is informative to compare the observed spectra relative to a glutaraldehyde/APTES functionalization. Upon PEG deposition, the peak at 286 eV is attenuated and a secondary peak at higher energy (287.5 eV) becomes more prominent. This shift is consistent with carbon-oxygen bonding and provides good evidence for effective PEG deposition. Functionalization of the surface with the protein laminin leads to a more complex spectra, which can be subdivided into three characteristic peaks. These peaks can be associated with carbon-carbon (main peak at 286 eV), carbon-oxygen (peak shoulder at 287.5 eV), and carbon-nitrogen (secondary peak at 289.5 eV) bonding within the coating, which is consistent with laminin coating and demonstrates protein deposition.

To determine the effectiveness of the PEG functionalization, the propensity of protein attachment to PEG was evaluated using semi-quantitative fluorescence analysis of FITC-BSA. Figure 12A shows fluorescent images before the deposition of PEG. FITC-BSA adsorbs strongly to the exposed aldehyde and comparatively less so to the laminin patterns. Upon covalent attachment of PEG, protein adsorption is strongly attenuated in unpatterned areas (Figure 12B). The quantified intensities of fluorescence are shown in Figure 12C. Interestingly, PEG deposition does not affect the ability of printed laminin to adsorb FITC-BSA, suggesting that the laminin adheres completely to the underlying aldehyde surface and prevents any attachment of PEG. Furthermore, the significant decrease in FITC-BSA adsorption following PEG deposition indicates that PEG is effectively preventing protein adsorption.

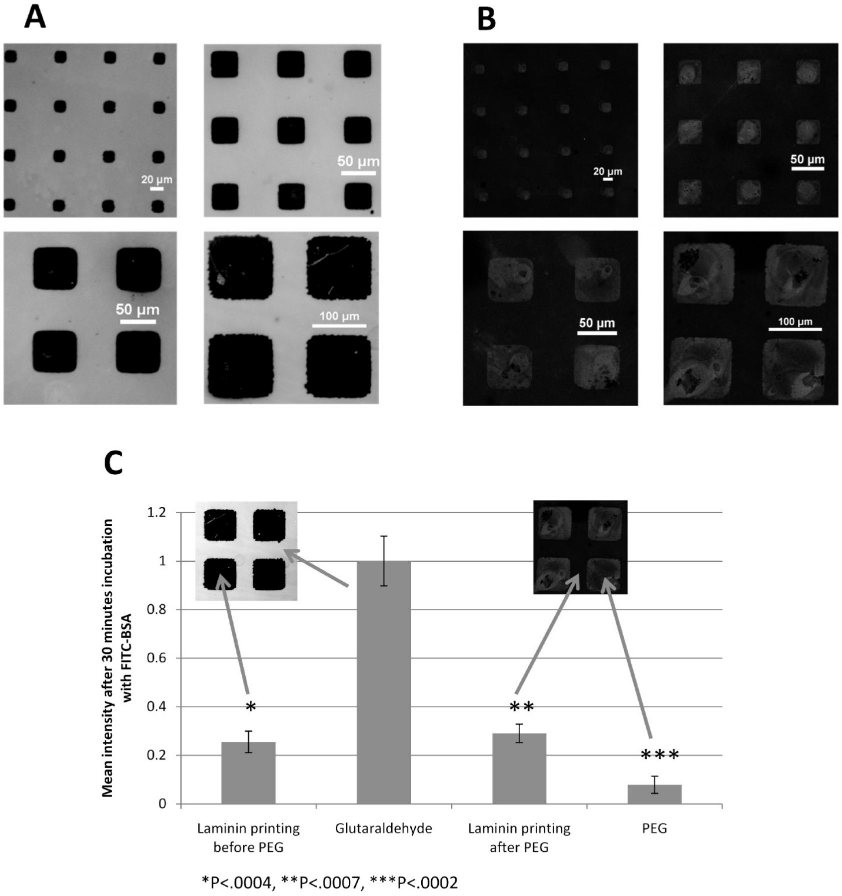

Figure 12 – Fluorescent Visualization and Characterization of Laminin Patterns
Glass cover slips are incubated with 20 µg/mL FITC-BSA for 30 minutes before (A) and after PEG deposition (B). 120 µm printed laminin cover slips were incubated with FITC-BSA before and after PEG deposition and imaged with a spectral confocal microscope (C). The images were analyzed semi-quantitatively and the data is presented as an average of n=3 samples ± standard deviation. P-values are calculated from a 1-tailed student's t-test.

2.2. Effect of seeding density on mono vs. multi-layered cluster formation

To assess the effect of seeding density, 60 μm square laminin features were prepared and seeded seeded with INS-1 (832/13) insulinoma cells at two representative seeding densities. The resulting cluster formations on the laminin patterns for 8,000 and 80,000 cells/cm^2 are shown in Figure 13A and Figure 13B, respectively. After initial attachment, cells migrate across the surface and form connections to other cells. Cell clusters eventually release from the PEG surface. Only partial cluster attachment to laminin is required for the remaining cells in that cluster to migrate and become confined to the area defined by the printed laminin. When printed patterns are too small for monolayer attachment of initially formed clusters the cells layer upon each other. This phenomenon occurs when cells are seeded at 80,000 cells/cm^2, but it is not observed when cells are seeded at 8,000 cells/cm^2. This effect is possibly due to the lower seeding concentration initially forming cell clusters small enough to fit in one layer on 60 μm patterns, and only reaching confluency after cells proliferate over time. At the higher seeding density, larger clusters are formed initially that cannot be accommodated by the 2D area, leading to multilayered clusters. From this we postulate that requirements for achieving multi-layered clusters include: (1) initial cell attachment to both adherent and non-adherent areas, (2) cell-cell attachment prior to the detachment of cells from non-adhesive areas, (3) and a cell seeding concentration at which initially formed clusters are too large to fit on each pattern.

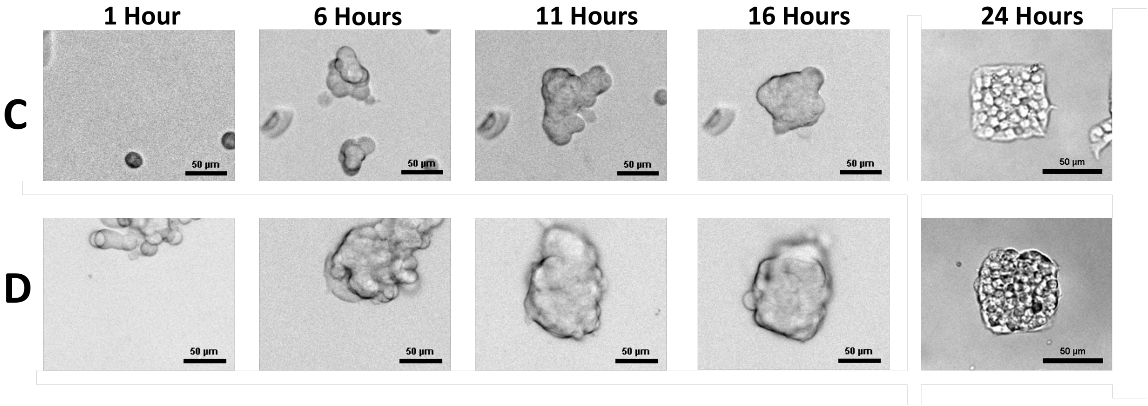

Figure 13 – Formation of Pancreatic β-cell Clusters

Brightfield images illustrating formation of cell clusters on cover slip seeded at 8,000 cells/cm^2 (A) and 80,000 cells/cm^2 (B). All images show live cells except for the 24 hour time point, which occurred after the cells had been fixed.

After 24 hours, cell clusters conform to the outlines defined by laminin patterns. A representative image of a mono-layered cluster and a multi-layered cluster is shown in Figure 14, where cells were fixed and stained for actin, nuclei, and insulin. These images show that higher cell seeding densities produce multiple cell layers confined to a 2D area. Furthermore, insulin immuno-staining verifies maintenance of insulin-production capability after patterning. The ability to produce both mono and multi-layer cell patterns and evaluate cluster-size dependent insulin production and distribution in response to physiological conditions, such as glucose stimulated insulin secretion, will potentially lead to the determination of optimal pancreatic β-cell cluster size for transplants.

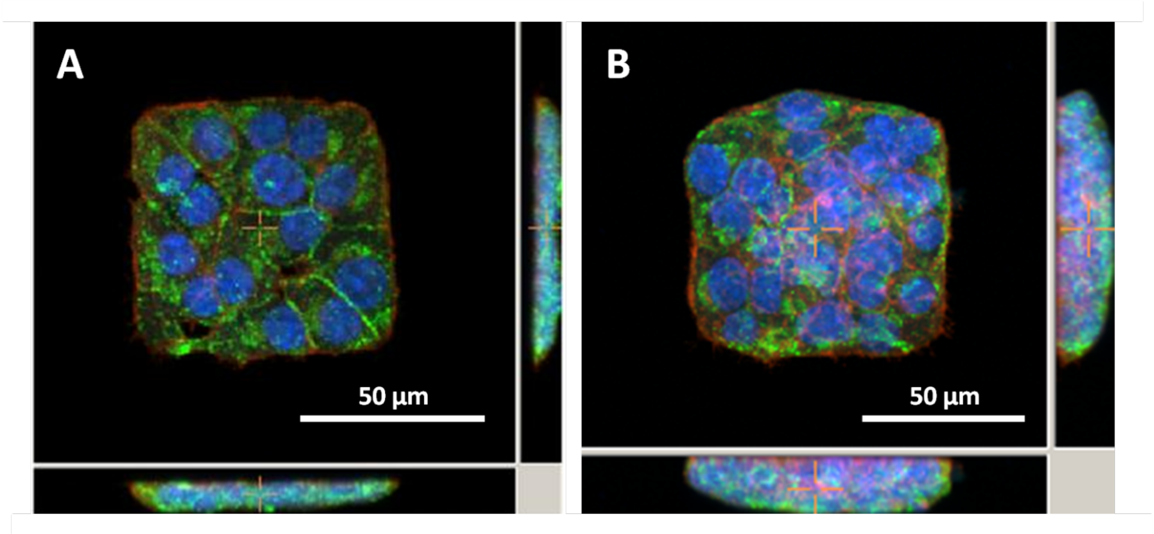

Figure 14 – Confocal Images of Mono and Multi-layered Pancreatic β-cell Clusters
Fluorescent images of 832/13 insulinoma cells forming monolayers (A) or multilayers (B). Red – F-actin phalloidin stain, Blue – DAPI nuclear stain, Green – anti-insulin Alexa 488 immunostain. (Cross-sections of central images are shown to right and below)

2.3. Effect of concentration of adherent area

The formation of mono-layered and multi-layered clusters is also influenced by the percentage of adherent area. Figure 15 shows bright-field images of live cells taken 24 hours after seeding at 80,000 cells/cm^2 on 40, 60, and 120 µm square laminin patterns. The separation between laminin islands are maintained at 50 µm as the laminin pattern size changes. As the pattern size increases, so does the available area for cells to adhere: 20%, 30%, and 50% of the area contains laminin for 40 µm, 60 µm and 120 µm patterns, respectively. In this case, the concentration of cells is held constant. On the smaller laminin patterns, attached cells have less adherent area to attach to resulting in the 40 µm patterns having almost all multi-layered clusters. In contrast, the 120 µm patterns are single-layered clusters and there is still area available in the pattern after 24 hours. Interestingly, the 60 µm patterns have a combination of mono and multi-layered clusters. The size of the clusters initially formed at seeding density 80,000 cells/cm^2 appears to be between 60 and 120 μm. Evidently, the formation of multi-layered clusters can also be achieved while maintaining cell seeding concentration by reducing the percentage of adherent area.

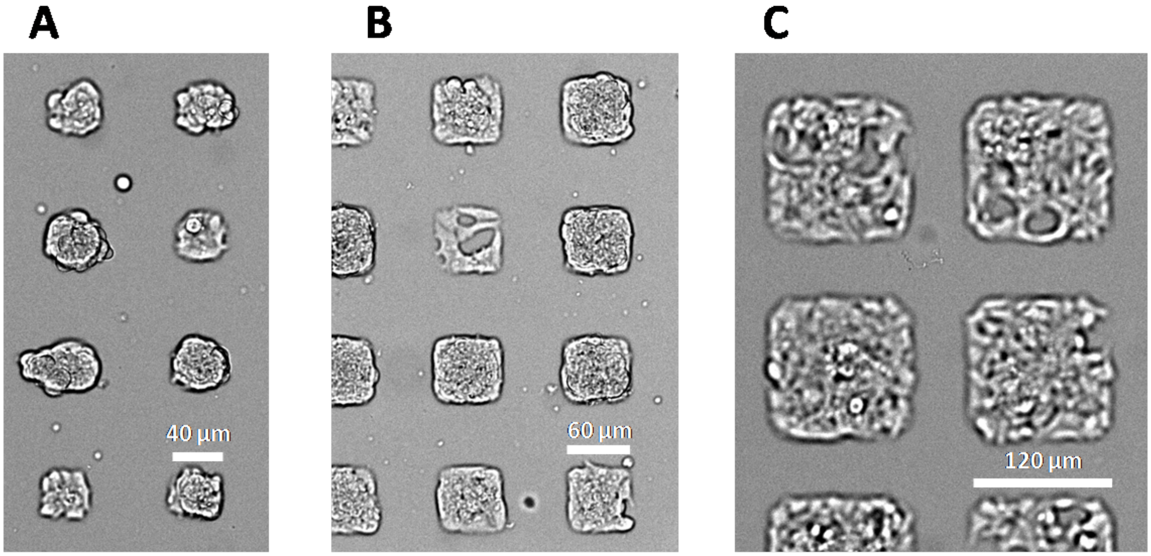

Figure 15 – 40, 60, and 120 μm Pancreatic β-cell Clusters
Bright-field microscopy of fixed 832/13 insulinoma cells on 40 (A), 60 (B) and 120 μm (C) laminin islands, demonstrating variation in mono- and multi-layer cell clusters.

3. Conclusion

We have demonstrated the first example of pancreatic β-cell patterning able to form both mono and multi-layered cell patterns, where previous use of cell patterning techniques for the evaluation of cell clusters has been limited to monolayers. Photolithographic and microcontact printing techniques were employed to develop this technique for patterning three-dimensional cell clusters. Extensive characterization including XPS, FTIR, and fluorescence microscopy confirmed the success of this method and was used to optimize cell patterning. The patterning technique described here enables the systematic evaluation of the effect that cluster size has on insulin production and viability for pancreatic β-cells.

Chapter 5 – Effect of Size on Insulin Production from Size-Controlled Insulin Secreting Cell Clusters

Abstract

An effective cure for type I diabetes from the transplantation of encapsulated pancreatic β-cell clusters has so far produced sub-optimal clinical outcomes. Previously, efforts have not controlled the size of transplanted clusters, a parameter implicated in affecting long-term viability and the secretion of therapeutically sufficient insulin. Here we demonstrate a method based on covalent attachment of patterned laminin for fabricating uniformly size-controlled insulin-secreting cell clusters. We show that cluster size within the range 40-120 μm in diameter affects a variety of therapeutically relevant cellular responses including insulin expression, content, and secretion. Our studies elucidate two size-dependent phenomena: (1) as the cluster size increases from 40 μm to 60 μm, glucose stimulation results in a greater amount of insulin produced per cell; and (2) as the cluster size increases beyond 60 μm, sustained glucose stimulation results in a greater amount of insulin secreted per cell. Our study describes a method for producing uniformly sized insulin-secreting cell clusters, and since larger cluster sizes risk nutrient availability limitations, our data suggests that 100-120 μm clusters could provide optimal viability and efficacy for encapsulated β-cell transplants as a treatment for type I diabetes.

.

1. Introduction

Development of a bioartificial pancreas began in 1933 when tissue containing insulin-secreting cells was first transplanted as a potential diabetes treatment[136]. Nearly eighty years later, human trials currently underway in New Zealand evaluating encapsulated islet transplants without immunosuppression report significant reductions in hypoglycemic events, but have yet to achieve reliable insulin independence. Transplantations of unencapsulated human cadaveric β-cell containing islets are currently available and provide at least one year of insulin independence for 80% of recipients[115]. While these pancreatic β-cells are able to sense glucose and secrete insulin at the appropriate level needed for glucose homeostasis, debilitating immunosuppression is required[14] and the availability of cadaveric islets is extremely limited[137]. Significant advances in encapsulation technologies over the past several decades promise to obviate the need for immunosuppression[138, 139]. Additionally, animal sources[140, 141] and human stem cell sources[142, 143] are being cultivated to overcome supply limitations. While these developments promise to overcome some of the limitations preventing wide-scale adoption of this therapeutic approach, efforts to control the size of transplanted clusters have been lacking.

Two independent size requirements must be satisfied in order to achieve viable islet transplants with sufficient insulin secretion. First, very small clusters do not exhibit therapeutically appropriate insulin secretion because of its dependence on sufficient cell-cell contact. For example, pancreatic β-cell pairs and monolayers secrete greater insulin per cell after glucose stimulation than isolated β-cells[118, 120]. Furthermore, glucose-dependent calcium oscillations, a characteristic of appropriately functioning islets, occur more frequently in cell clusters compared with isolated cells[144]. Second, excessively large clusters suffer from nutrient availability limitations. Relying solely on passive diffusion, oxygen and nutrient requirements are attained only when cells are within 200 μm from a capillary[145]. In fact, necrosis has been observed on the inside of large isolated islets[62]. As expected from these results, islets smaller than 150 μm in size exhibit improved insulin secretion and viability in clinical studies than larger islets[116]. While cell encapsulation in a material with pore sizes small enough to inhibit the passage of antibodies protects transplants from the immune response[78], the same material also inhibits the growth of new blood vessels and prevents access to perfusion that is essential for nutrient availability throughout large islets in the native pancreas[146]. Despite significant evidence supporting the impact that cluster-size may have on insulin secretion and viability of encapsulated transplants, to date there appears no study that either explicitly explores the insulin response to varying cluster-sizes or presents a method for fabricating uniformly sized clusters.

Here, we used the covalent microcontact printing of laminin, as described previously[147], to fabricate size-controlled patterned insulin-secreting cell clusters. The rat insulinoma cell line INS-1 (832/13) was selected for evaluation due to its dose-dependent glucose stimulated insulin secretion within physiologically relevant glucose conditions[111]. We anticipate the use of stem cells to overcome supply limitations to clinical translation, as stem cells may be grown indefinitely prior to differentiation.

Separately, we have demonstrated successful differentiation of size-controlled human embryonic stem cell clusters along the pancreatic lineage, as well as detachment of these clusters which may be necessary prior to transplantation[148]. Our data suggests the existence of an optimal cluster size after evaluating its impact on insulin expression, content, and secretion from uniformly sized 40-120 μm insulin-secreting cell clusters. Successful production of size-controlled insulin-secreting clusters that appropriately balance the need for cell-cell contact and nutrient availability is a necessary step towards achieving long-term insulin independence for the millions that suffer from type I diabetes.

2. Results

2.1. Fabrication of uniformly size-controlled insulin-secreting cell clusters

Insulin-secreting cells were uniformly patterned in size-controlled clusters onto glass coverslips using a modified version of a technique previously described by us[147]. Laminin, a cell-adhesive protein, is first covalently microcontact printed from a lithographically-created polydimethylsiloxane stamp onto an aldehyde-functionalized coverslip. Subsequent incubation with a fluorescent protein enables visualization of the areas surrounding the laminin pattern (Figure 16a). To create cell patterns, laminin stamping is followed by the covalent attachment of polyethylene glycol, a cell-repulsive polymer, to the remaining available aldehydes. Cells seeded onto these coverslips conform to varying laminin patterns with remarkable precision (Figure 16b).

Furthermore, this technique enables pattern uniformity across the entire coverslip as visualized by 40 μm (Figure 16C), 60 μm (Figure 16D), and 120 μm (Figure 16E) circular cell patterns that are fixed and stained for nuclei and f-actin. We observed that the intensity of the nuclear stain, DAPI, linearly correlates with the number of nuclei within a given cluster (Figure 17A). A histogram representation reveals a Gaussian distribution of the numbers of cells in a cluster on a given coverslip (Figure 17B). The average number of cells in a cluster increases with the size of the laminin pattern; 6.61 ± 1.01 for 40 μm clusters, 15.71 ± 0.70 for 60 μm clusters, and 55.40 ± 2.25 for 120 μm clusters (n=3, data presented as average ± standard deviation, see Figure 17C).

2.2. Effect of Cluster Size on Insulin mRNA Expression and Secretion

After achieving confluency on patterned coverslips, insulin-secreting cells were subjected to glucose-stimulated insulin secretion (GSIS). The cells were first immersed in a 5 mM glucose solution, reducing insulin secretion to basal levels. 18-20 hours later, the cover slips were washed with a buffer containing no glucose, no amino acids, and no fatty acids to prevent insulin production, and the media was replaced with the same glucose-free buffer. After 2 hours of glucose starvation, coverslips were stimulated with a 15 mM glucose buffer, without amino acids or fatty acids in order to isolate the effect of glucose-dependent insulin production. Proinsulin mRNA expression, normalized to β-actin mRNA expression, was evaluated for 40 μm, 60 μm, and 120 μm clusters before, 15 minutes after, and 1 hour after glucose stimulation. While no difference was observed prior to glucose stimulation, normalized proinsulin mRNA expression was almost 2-fold greater (P<.021) after 15 minutes of stimulation for the 60 μm and 120 μm clusters compared with the 40 µm clusters (Figure 18A). After 1 hour of stimulation, expression levels were the same across all measured cluster sizes.

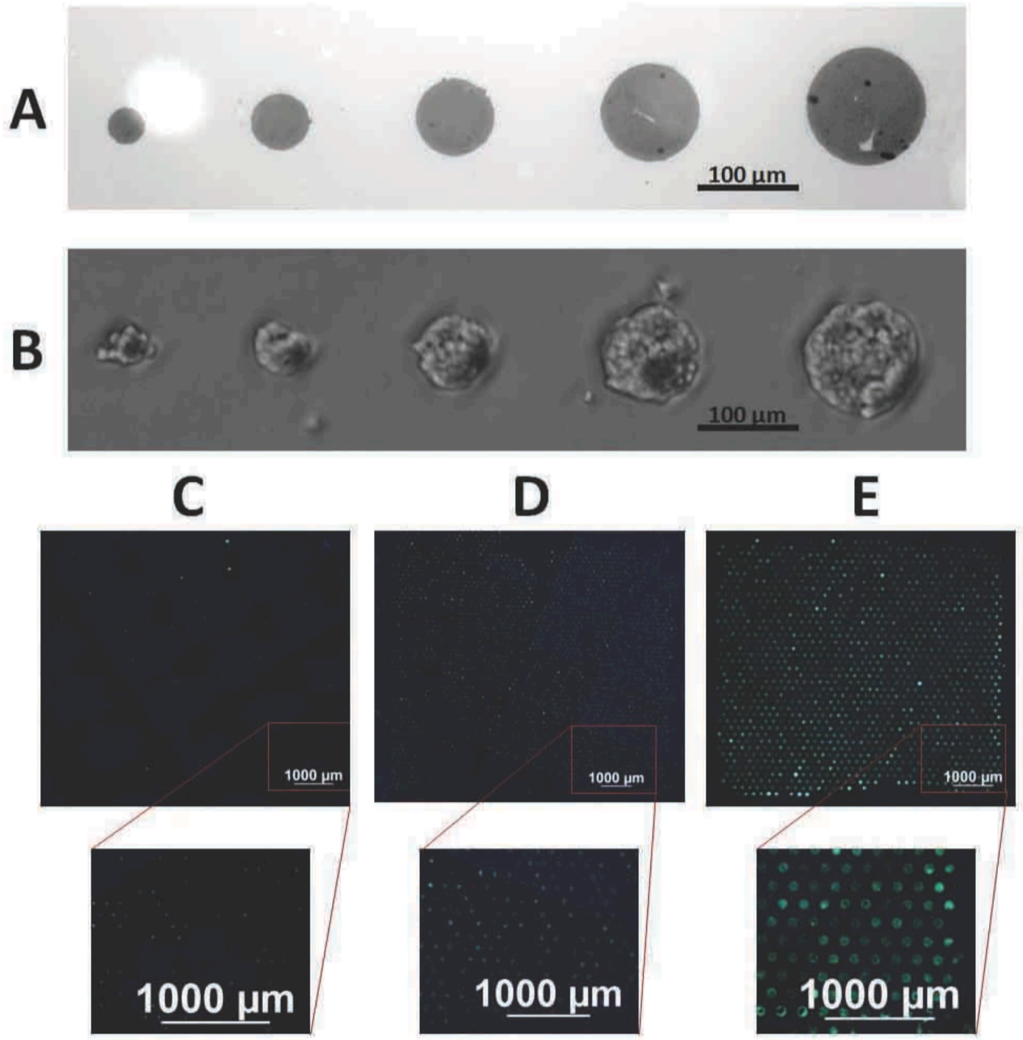

Figure 16 – Cells seeded on patterned laminin become uniform size-controlled clusters.

After covalent printing of laminin to aldehyde coverslips, the coverslips are incubated with 50 µg/mL fluorescein isothiocyanate-conjugated bovine serum albumin which bind to the available aldehydes, enabling fluorescent visualization of 40, 60, 80, 100, and 120 µm circular patterns (A). Attachment of methoxypolyethylene glycol-amine and subsequent sodium cyanoborohydride reduction enables 832/13 rat insulinoma cells to selectively bind to the laminin islands, verified using bright-field microscopy (B). Fluorescent staining of nuclei (DAPI, blue) and f-actin (Alexa Fluor 488 Phalloidin, green) verifies uniformity of 40 µm (C), 60 µm (D), and 120 µm (E) patterns after seeded cells achieve confluency.

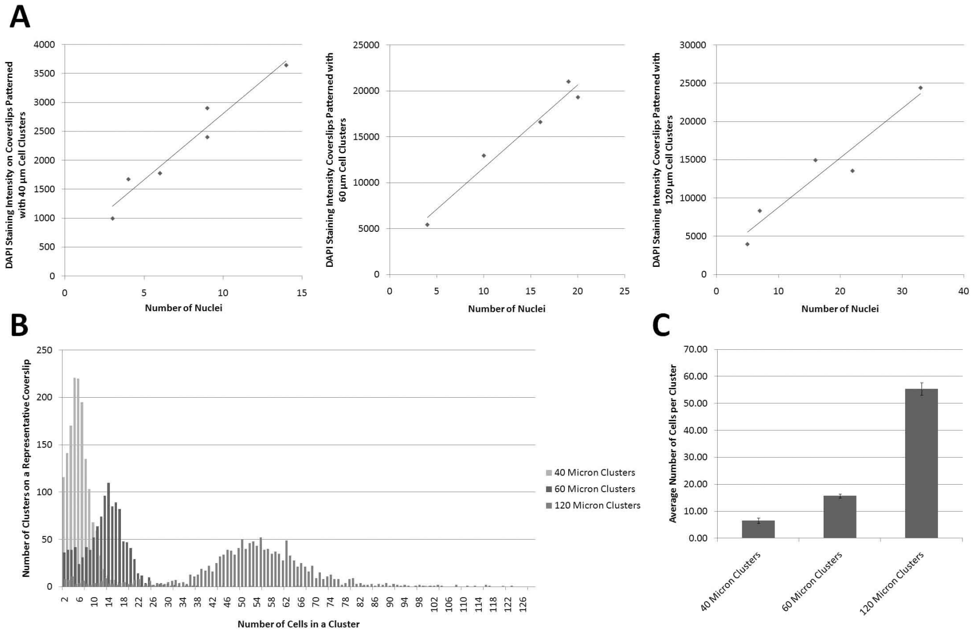

Figure 17 – Establishment of linear correlation between the number of nuclei and the nuclear stain in wide-field images and characterization of the number of cells within a cluster at different cluster sizes.

The location of a cell cluster is determined through a binary threshold on the channel representing the f-actin stain. Within an individual cluster, the total intensity of the channel representing the DAPI stain is plotted as a function of the number of nuclei that are manually counted. Representative correlations are linear for all sized clusters (A – 40 µm – left, R^2 = 0.9432; 60 µm – center, R^2 = 0.9611, 120 µm – right, R^2 = 0.9181). Representative distributions of cluster sizes on a given coverslip reveal a Gaussian distribution (B). The average number of cells per cluster increases with the size of the pattern (C – n=3 coverslips, data is presented as an average ± standard deviation).

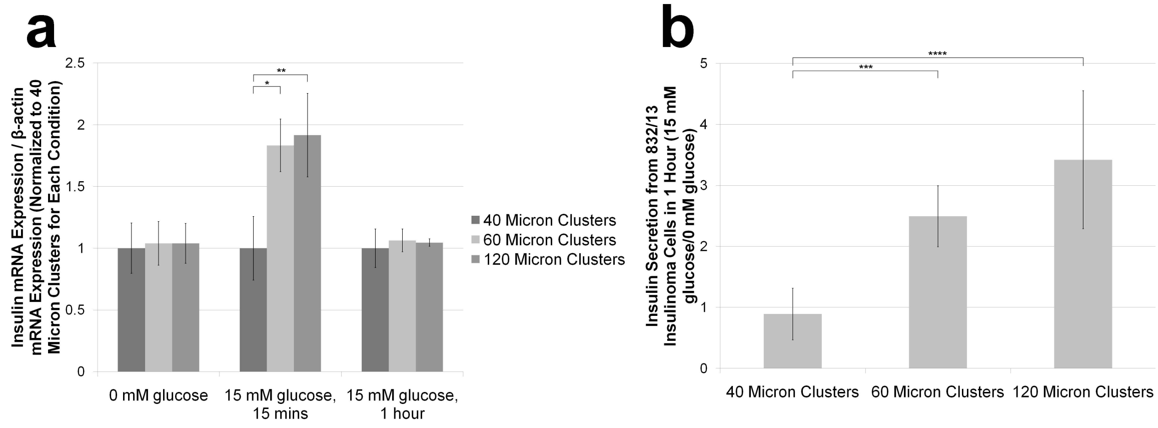

Figure 18– Normalized proinsulin mRNA expression and normalized insulin secretion increases with larger cluster sizes.

*(a) RT-PCR was used to determined normalized insulin 2 mRNA expression for 40, 60, and 120 μm patterned confluent clusters 15 minutes after and 1 hour after 832/13 insulinoma cells were exposed to GSIS (data normalized to the average of the 40 μm clusters for each glucose condition). Additionally, (b) the impact of glucose stimulation on insulin secretion from 40 μm, 60 μm, and 120 μm clusters was determined by normalizing measured insulin secretion over 1 hour from clusters stimulated with 15 mM glucose (n=3) to clusters stimulated with 0 mM glucose that mimics basal secretion levels (n=3) for each cluster size. Data is presented as an average ± standard deviation. *P = .013, **P = .020, ***P = .013, ****P=.022, as determined by a type 2 student's t-test, two-tailed. Statistical significance for the comparison of multiple groups was confirmed for each group indicated with an * using a Holm-Sidak test with α=.05 after performing an analysis of variances (ANOVA).*

Additionally, the effect of cluster size on insulin secretion was evaluated after GSIS. Samples were taken from wells containing coverslips patterned with 40, 60, and 120 μm insulin-secreting cell clusters subjected to glucose starvation and then either continued glucose starvation or glucose stimulation for 1 hour. Glucose stimulation did not result in greater insulin secretion from 40 μm clusters compared with unstimulated clusters. Glucose stimulation resulted in 2.5-fold greater insulin secretion for 60 μm clusters and nearly 3.5-fold greater insulin secretion for 120 μm clusters, compared with unstimulated clusters of the same size (Figure 18B).

2.3. Effect of Cluster Size on C-peptide Content

C-peptide content from patterned 832/13 insulinoma cells was evaluated as a surrogate for insulin content to distinguish the portion of insulin content that is the result of de novo insulin synthesis by first establishing colocalization of insulin and c-peptide immunofluorescence. Each insulin molecule requires the production of a c-peptide molecule for assembly[149, 150]. Positive c-peptide staining is used to verify the presence of de novo insulin synthesis as opposed to exogenously introduced insulin[151]. After achieving confluency on a 40 μm pattern, the cell clusters were fixed, permeabilized, and immunostained for insulin and c-peptide. Immunofluorescent images were obtained for both the 488 nm insulin channel and the 633 nm c-peptide channel (Figure 19a and b). Merging the channels reveals near perfect colocalization (Figure 19c). To eliminate ambiguity over the source of insulin, c-peptide content will be used to indicate insulin content hereafter.

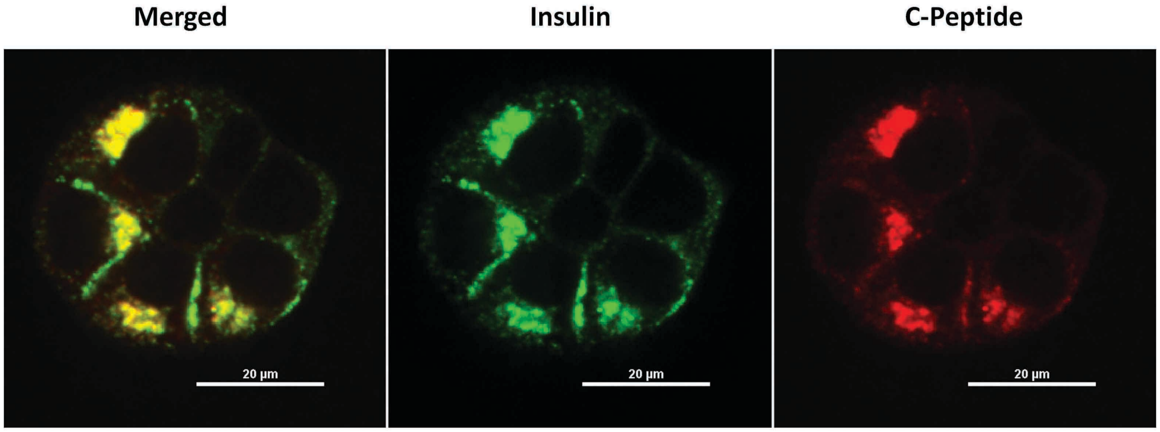

Figure 19– Colocalization of insulin and c-peptide.
832/13 insulinoma cells are grown to confluency on a 40 μm circular laminin pattern. The cells are fixed, permeabilized, and immunostained for insulin (Alexa Fluor 488, green) and c-peptide

(Alexa Fluor 633, red). The merged image on the left verifies colocalization of insulin and c-peptide.

Coverslips with cell clusters ranging from 40-120 μm in diameter were exposed to GSIS and the effect of cluster size on normalized c-peptide content was evaluated using immunocytochemistry. Before, 15 minutes after, and 1 hour after glucose stimulation, the cell clusters were fixed, permeabilized, immunostained for c-peptide to determine insulin content, f-actin to define the border of the cell cluster and dsDNA to label the nuclei. After image acquisition, the total intensity of c-peptide was determined within the confines of the cell cluster defined by a binary threshold on the channel representating the f-actin stain. The nuclei in several images were counted, and a linear correlation was established between the total nuclear staining intensity and the number of nuclei (Figure 20). Quantified c-peptide intensity was therefore normalized to nuclear stain intensity. Combining 40, 60, 80, 100 and 120 μm diameter clusters on a single cover slip isolated the effect of cluster size during analysis from other experimental variables.

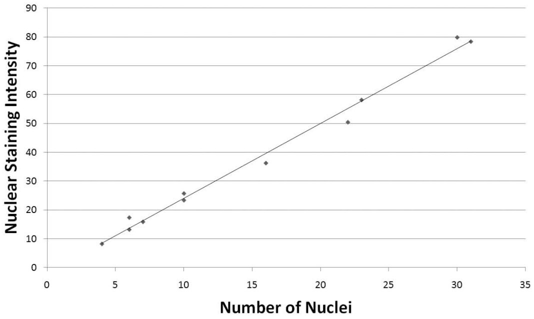

Figure 20– Establishment of linear correlation between the number of nuclei and the nuclear stain in confocal images.

The number of nuclei within 832/13 insulinoma cell clusters on 60 μm laminin patterns are both counted manually and using image analysis. The confines of each cluster are defined using a binary threshold of the f-actin channel, and the total quantified nuclear stain within a given cluster is plotted with respect to the number of nuclei in that same cluster when counted manually, revealing a linear correlation (n=11, R^2=0.9901).

Representative confocal images at each glucose condition are displayed in Figure 21. For this analysis, clusters that appeared in a monolayer were analyzed in order for the effect of lateral cell-cell contact to be isolated from any impact that multiple cell layers would contribute. Qualitatively, cluster size did not appear to affect c-peptide content prior to glucose stimulation. However, after 15 minutes of glucose stimulation, c-peptide content in the 40 μm clusters appeared less than that present in the other cluster sizes. Interestingly, after 1 hour of stimulation at 15 mM glucose, the 40 μm and 60 μm clusters had accumulated greater c-peptide content than the larger cluster sizes. Quantitatively, normalized c-peptide staining intensity for 40, 60, 80, 100 and 120 μm circular cell clusters over the three glucose conditions under evaluation are presented in Figure 22A. After glucose starvation for 2 hours, cluster size had no impact on insulin content. However, 15 minutes after glucose stimulation, cells in 40 μm clusters contained less c-peptide than any of the larger cluster sizes. C-peptide content 15 minutes after glucose stimulation was not affected by monolayered cluster sizes between 60-120 μm. Interestingly, 1 hour after glucose stimulation, the smaller sized (40 μm and 60 μm) clusters contained greater c-peptide content than the larger sized (100 μm and 120 μm) clusters.

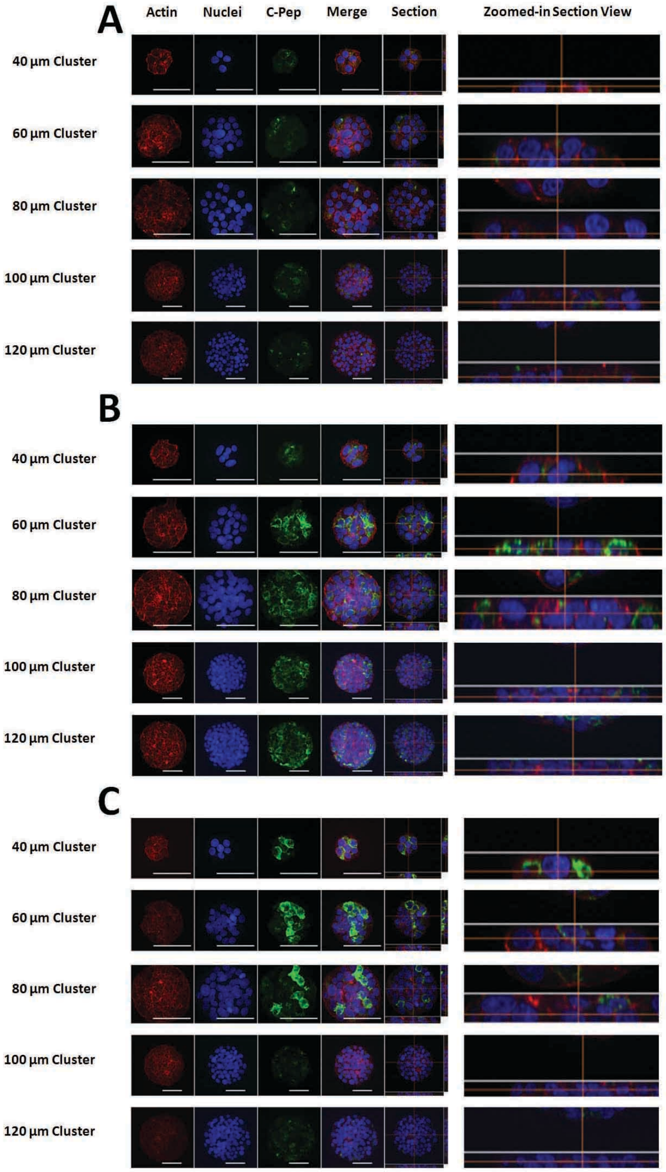

Figure 21– Confocal images of monolayered insulin-secreting cell clusters illustrate the effect that cluster size has on c-peptide content under different glucose conditions.

832/13 insulinoma cells are grown to confluency on coverslips that have a combination of 40, 60, 80, 100 and 120 µm patterns. Cell clusters are fixed just prior (A), 15 minutes after (B), and 1 hour after (C) glucose stimulation, permeabilized, and stained for f-actin, nuclei, and c-peptide. Confocal z-stack images are taken throughout each cluster. A maximum intensity projection enables visualization of staining throughout the z-stacks (actin, nuclei, c-pep, and merge). One representative slice of the z-stack is displayed to the right of the maximum intensity projections (section), and the zoomed in section view verifies that the cell clusters are in a monolayer. Scale bar = 50 µm.

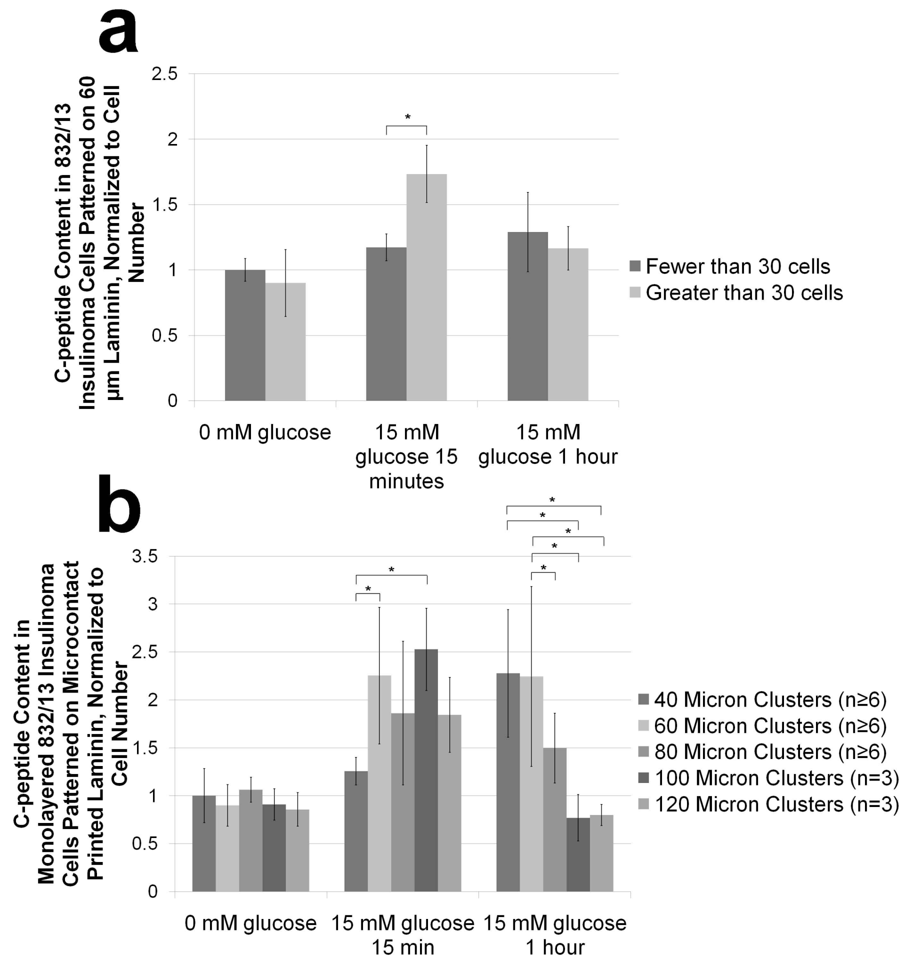

Figure 22– Semi-quantitative immunocytochemistry reveals effects of cluster size on normalized c-peptide content under different glucose conditions.

*832/13 insulinoma cell clusters are fixed, permeabilized and stained for c-peptide, f-actin and nuclei before, 15 minutes after, and 1 hour after glucose stimulation. Confocal images are acquired and total intensity of c-peptide staining is normalized to the nuclear stain. Normalized c-peptide intensity in monolayered clusters on a single coverslip containing 40, 60, 80, 100 and 120 µm are compared to each other for each glucose condition (A – data is normalized to the average of the 40 µm clusters before glucose stimulation). When cells are seeded at 100,000 cells/cm^2 and allowed to grow for 48 hours, 60 µm circular patterned coverslips have both monolayered (<30 cells) and multilayered (>30 cells) clusters. Normalized c-peptide intensity is also evaluated between monolayered and multilayered clusters for each glucose condition (B – data is normalized to the average of monolayered clusters before glucose stimulation). Data is presented as an average ± standard deviation. Statistical significance is indicated with an * and was established using the Student-Newman-Keuls Test with a α=.05 after performing an ANOVA.*

The effect that multiple cell layers has on c-peptide content was evaluated by comparing monolayered and multilayered cell clusters confined to a 60 μm diameter. As previously described, multilayer formation can occur when initially formed clusters contain too many cells to fit in one layer on the printed laminin and pile on top of each other as they retreat from the cell-repulsive PEG[147]. Coverslips that contained only 60 μm circular patterns were seeded with insulin-secreting cells at 100,000 cells/cm^2 and allowed to grow for approximately 48 hours which enabled the formation of both mono and multilayered cell clusters on a single cover slip. While no c-peptide content differences were observed prior to glucose stimulation, c-peptide content in multilayered 60 μm clusters exceeded that of monolayered 60 μm clusters after 15 minutes of glucose stimulation (Figure 22B). Representative images qualitatively confirm this effect (Figure 23). This difference disappeared after stimulation was sustained for one hour.

3. Discussion and Conclusions

This study suggests that as insulin-secreting cell cluster size increases from 40 μm to 120 μm, the insulin response to glucose stimulation is affected at two separate threshold sizes: the first results in greater insulin expression and translation shortly after glucose stimulation, and the second results in more efficient insulin secretion after sustained glucose stimulation. After expression and subsequent translation, a number of post translational steps occur resulting in the storage of mature insulin and c-peptide awaiting secretion[152]. One previous simulation of β-cell behavior speculated that a minimum of 4 β-cell-β-cell contacts are required for insulin bursting coordination, and that this coordination improves upon addition of several more β-cells before reaching a plateau[123]. Characterization of our cell patterns revealed that 40 μm patterns contained on average between 6 and 7 cells per cluster, and 60 μm patterns contained on average between 15 and 16 cells per cluster (Figure 17C). Our data supports this study's suggestion that insulin production behavior is affected by the number of β-cells in contact with each other, as well as the approximate number of cells required to effect such changes.

The existence of a second threshold cluster size enabling more efficient insulin secretion was less expected, and further exploration will be required prior to speculation of a responsible mechanism. Nonetheless, as the cluster size increased from 60 μm to 100 μm, c-peptide content after 1 hour of glucose stimulation decreased in a size-dependent fashion, with no additional decrease between 100 μm and 120 μm clusters. Instead of a concurrent reduction in insulin secretion over this time period, cells in 120 μm clusters on average responded with greater insulin secretion (~3.5-fold) compared with cells in 60 μm clusters (~2.5-fold), although this result was not significant (Figure 18B). These two observations, when taken together, suggest that the larger cluster sizes secrete insulin more quickly, with less storage, after sustained glucose stimulation.

We realize that evaluation of insulin secretion included a portion of clusters with more cells than those used in content analyses, some of which were multilayered in nature (Figure 17). We have also demonstrated that multilayered 60 μm clusters contain more c-peptide 15 minutes after glucose stimulation than monolayered 60 μm clusters (Figure 22B). However, multilayered clusters did not contain reduced c-peptide compared with monolayered clusters after 1 hour of sustained glucose stimulation, supporting the proposal that a second size-dependent threshold enabling more efficient insulin secretion exists, and that multilayered 60 μm clusters do not exceed this threshold. After considering all of these factors, our data suggests that 120 μm cell clusters secrete insulin more rapidly during sustained exposure to glucose after expression and translation than 60 μm cell clusters. Furthermore, since 100 μm clusters exhibited similarly low c-peptide content after sustained glucose simulation, the threshold size for achieving more rapid insulin secretion is likely between 80 and 100 μm.

Multiple methods exist that would enable subsequent transplantation of these patterned clusters. First, the clusters could be transplanted in a patterned sheet, similar to a concept described previously and still in development [80]. This approach would require cell patterning to occur on a biocompatible substrate, or the transfer of patterned clusters to a biocompatible material. Second, microcapsules can encapsulate size-controlled clusters that are dislodged either naturally over time[148] or with exposure to collagenase-dispase (Figure 32). Lastly, size-controlled clusters may improve the clinical outcomes of immunosuppressed transplantation. The insulinoma cells used in this study are not ideal candidates for transplantation, in part due to the immortalized nature of the cell line. We considered the use of primary β-cells from MIP-GFP mice, but the number of cells necessary for these studies would require the use of hundreds of animals. Instead, we are separately investigating the differentiation of human embryonic stem cells, which can be proliferated indefinitely prior to differentiation, into 120 μm size-controlled clusters along the pancreatic lineage, which become 100 μm spherical clusters when released[148]. Regardless of the encapsulation approach, incorporation of size-controlled clusters into encapsulated transplantation therapy promises to overcome one of the few remaining challenges impeding this therapy from achieving successful outcomes.

In conclusion, we describe a method for fabricating uniformly size-controlled insulin-secreting cell clusters through covalent microcontact printing of laminin on aldehyde-functionalized coverslips. We demonstrate that cluster-size affects the insulin response to glucose stimulation in a therapeutically relevant manner. Finally, the results of our studies suggest that, among the sizes evaluated here, 100-120 μm clusters demonstrate the greatest promise for encapsulated transplantation therapy for treating type I diabetes.

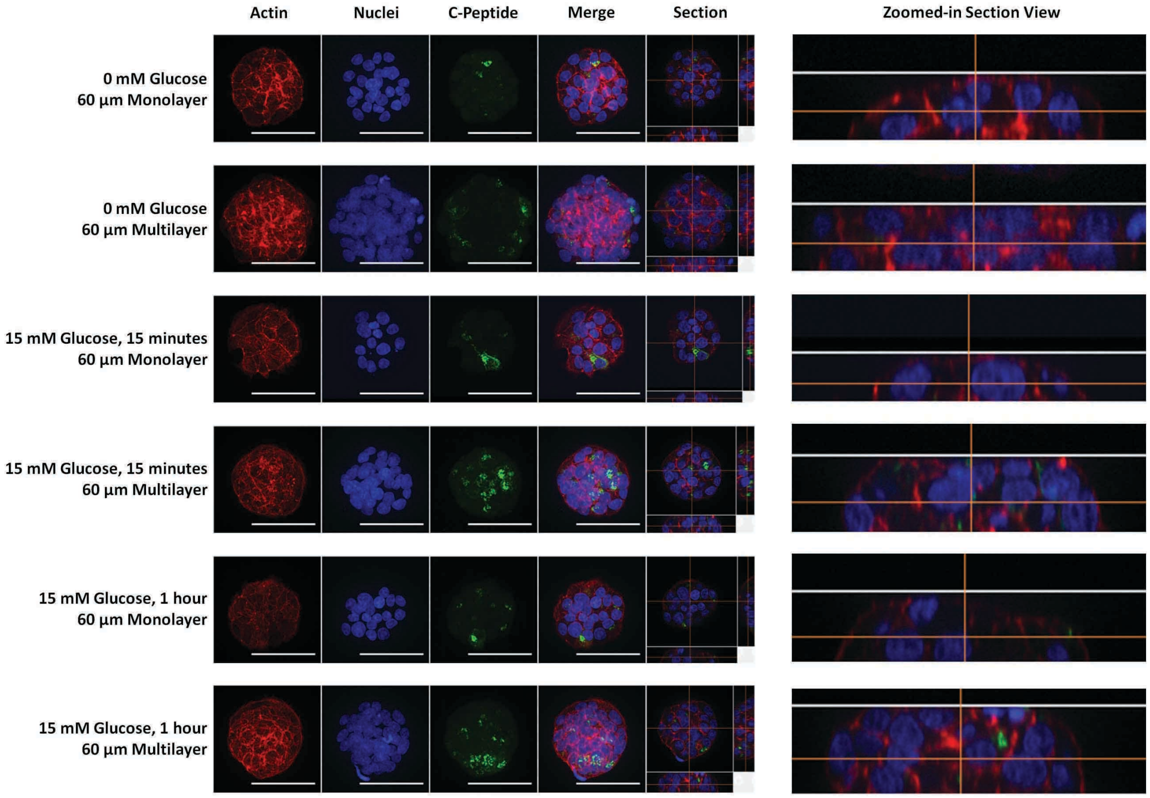

Figure 23– Confocal images of monolayered and multilayered insulin-secreting cell clusters illustrate the effect that multiple cell layers has on c-peptide content under different glucose conditions.

832/13 insulinoma cells are grown to confluency on coverslips that only have 60 µm patterns. Cell clusters are fixed, permeabilized, and stained for f-actin, nuclei, and c-peptide. Confocal z-stack images are taken throughout each cluster. A maximum intensity projection enables visualization of staining throughout the z-stacks (actin, nuclei, c-pep, and merge). One representative slice of the z-stack is displayed to the right of the maximum intensity projections (section), and the zoomed in section view verifies that the cell clusters are either in a monolayer or in multiple layers. Scale bar = 50 µm.

Chapter 6 – Differentiation of Human Embryonic Stem Cells Into Pancreatic Endoderm in Patterned Size-Controlled Clusters

Abstract

Pancreatic β-cells function optimally when clustered in islet-like structures. However, nutrient and oxygen deprivation limits the viability of cells at the core of excessively large clusters. Hence, production of functional β-cells from human embryonic stem cells (hESCs) for patients with diabetes would benefit from the growth and differentiation of these cells in size-controlled aggregates. In this study, we controlled cluster size by seeding hESCs onto glass cover slips patterned by the covalent microcontact-printing of laminin in circular patches of 120 μm in diameter. These were used as substrates to grow and differentiate hESCs first into SOX17-positive/SOX7-negative definitive endoderm, after which many clusters released and formed uniformly sized three-dimensional clusters. Both released clusters and those that remained attached differentiated into HNF1β-positive primitive gut tube-like cells with high efficiency. Further differentiation yielded pancreatic endoderm-like cells that co-expressed PDX1 and NKX6.1. Controlling aggregate size allows efficient production of uniformly-clustered pancreatic endocrine precursors for in vivo engraftment or further in vitro maturation.

1. Introduction

The elevated blood glucose that characterizes diabetes mellitus results from the loss of insulin-producing β-cells from the islets of Langerhans in the pancreas (type 1 diabetes mellitus) or from a relative deficiency of insulin production in a setting of reduced insulin sensitivity (type 2 diabetes mellitus). Transplantation of cadaveric pancreata or the β-cell-containing islets thereof offers the only cure for patients dependent on exogenous insulin[16]. However, immune-mediated damage to the transplanted β-cells and insufficient revascularization[117] leading to nutrient and oxygen-deprivation, especially inside large islets, limits islet survival. As a consequence, the long-term benefits of these grafts are limited; most recipients remain insulin-independent for less than two years[17]. Besides, current numbers of donor organs cannot provide enough material for all patients.

The potential of human embryonic stem cells (hESCs) to differentiate into any somatic cell type, including glucose-responsive insulin-producing cells[142], offers a possible solution to the shortage of transplantable cells. Unfortunately, current *in vitro* differentiation protocols do not generate homogeneous populations of functional β-cells (for review, see [143]). Furthermore, these protocols rely on consecutive exposures of hESCs to various factors, either in an adherent monolayer format or after an embryoid body-formation step, which is associated with spontaneous differentiation into various undesired cell types. In addition, the size of end-stage clusters varies greatly, and is difficult to control.

The sensitivity of β-cells to external glucose levels, and their responsive insulin release, is highly dependent on cell-cell contact. Notably, clusters comprising multiple β-cells have a greater glucose-stimulated insulin release than single β-cells[118, 119]. Furthermore, β-cells secrete more insulin when in three-dimensional aggregates than in monolayers[120]. In addition, nutrient deprivation is observed in transplanted islets with diameters exceeding 100 μm[116]. Therefore, hESC-derived β-cells will most likely function optimally after transplantation when clustered in multicellular structures that are approximately 100 μm in diameter, a size that is large enough for efficient glucose-responsive insulin secretion, yet small enough to prevent nutrient starvation of cells residing in the core.

Here, we report a procedure to derive definitive endoderm cells from hESCs with high efficiency, while culturing them on covalently-bound laminin circular patches of 120 μm in diameter. Subsequent exposure to keratinocyte growth factor converted these adherent aggregates into highly homogeneous clusters comprising mainly HNF1β$^+$ primitive gut tube-like cells. Furthermore, cells in these clusters differentiated into PDX1$^+$/NKX6.1$^+$ pancreatic endoderm upon consecutive exposure to additional factors. In addition, the primitive gut tube-like clusters could be dislodged mechanically, without enzymatic treatment, after which they balled up into uniform ~100 μm-diameter spheres that retained the ability to form pancreatic endoderm-like cells co-expressing PDX1 and NKX6.1. Since the size of transplanted islets impacts insulin secretion and viability[116], the generation of hESC-derived pancreatic progenitors in spherical clusters of controllable size and cell number could, as proof of concept, contribute to developing a renewable, long-lasting treatment for type I diabetes.

2. Results

2.1. *Maintenance of hESCs on laminin-coated glass cover slips*

To develop methods for growing hESCs in controlled cluster sizes, we first tested for culturing conditions that allowed for adherence and growth on glass cover slips in the absence of MEFs. Since hESCs have an epithelial character[153] and express integrins α2, α6, β1, and β4[113, 154, 155], laminin was chosen for a scaffold protein. Glass cover slips were coated non-covalently with laminin or laminin-containing Matrigel in the absence of MEFs.

Static water contact angle measurements were performed by a technique that assesses the hydrophobicity of a surface to verify laminin attachment. Clean, dry, plasma-treated cover slips are hydrophilic and exhibited water contact angles near zero degrees (n=3). Laminin or matrigel coating rendered the surfaces more hydrophobic and resulted in a water contact angles of 30.7±1.2 and 30.0±1.0, respectively (n=3). Since laminin is the dominant matrix component of Matrigel, their water contact angles are expected to be similar.

The buoyancy of the generally hydrophobic laminin-coated cover slips was reduced by incubating them overnight in serum-containing medium, which coincidentally increased the affinity of the hESCs for the treated cover slips. Using these laminin-coated surfaces and MEF-conditioned medium supplemented with FGF2, hESCs could be maintained for at least three days without loss of the pluripotency marker OCT4 (Figure 24A). Moreover, hESCs grew at slightly higher densities in these conditions than in the same medium on Matrigel-coated cover slips (Figure 24B) or cover slips coated with gelatin, collagen I or fibronectin (Figure 25A-C). This difference in cell density may have resulted from a higher fraction of cells attaching to the laminin-coated surface than to the Matrigel-coated surface after passaging.

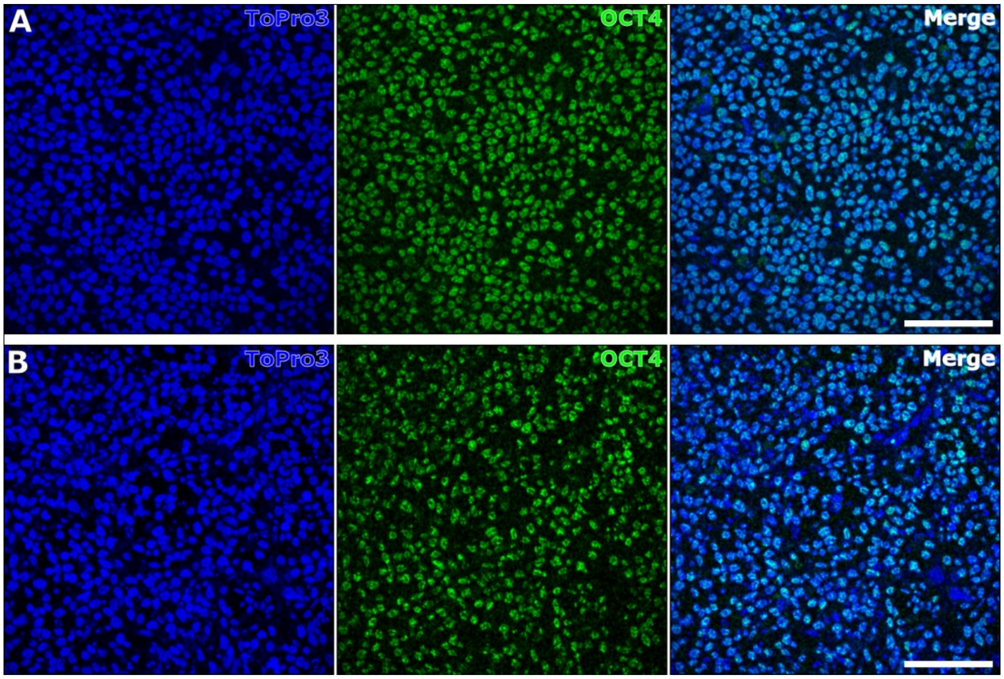

Figure 24 – hESCs grown on laminin- or Matrigel-coated glass retain OCT4 expression.
Confocal fluorescence microscopic imaging is shown for OCT4 (green) in hESCs that were plated without feeder cells on glass cover slips coated with laminin (A) or Matrigel (B). Nuclear staining with ToPro3 is shown in blue. Scale bars, 100 μm.

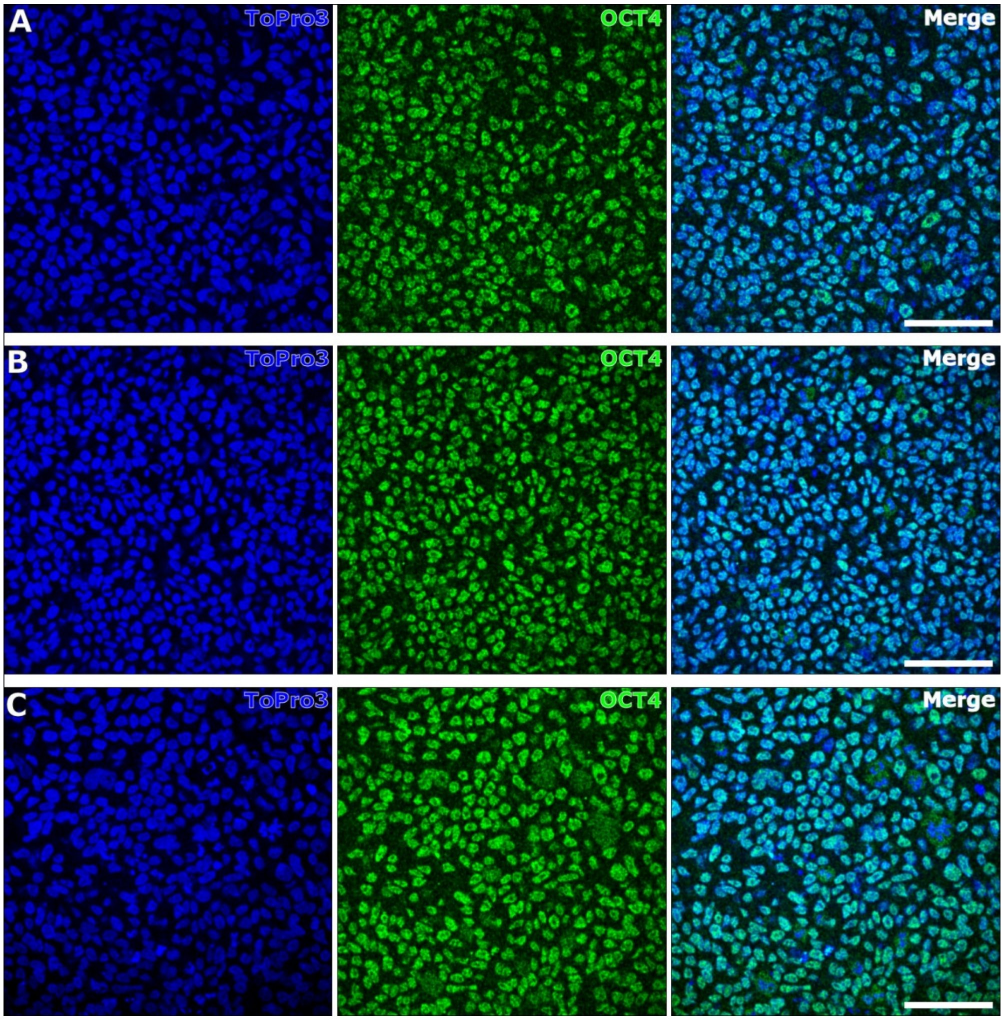

Figure 25 – hESCs grown on gelatin-, collagen I or fibronectin-coated glass retain OCT4 expression.

Confocal fluorescence microscopic imaging is shown for OCT4 (green) in hESCs that were plated without feeder cells on glass cover slips coated with gelatin (A), collagen I (B) or fibronectin (C). Nuclear staining with ToPro3 is shown in blue. Scale bars, 100 μm.

2.2. Maintenance of hESCs on microcontact-printed glass cover slips

To control cluster size, glass cover slips were microcontact-printed with covalently-bound laminin in circular patterns of 120 μm in diameter with a spacing of 200 μm in between. Because laminin attachment quenches the aldehydes on the glass surface, and laminin binds poorly to BSA[147], FITC-BSA incubation at 50 μg/ml for 20 min enabled visualization of the unquenched aldehydes on the glass surface between the patterns and confirmed correct laminin patterning (Figure 26A and B). Finally, to render the glass surface in between the patterns resistant to cell attachment, the remaining aldehydes were then passivated with mPEG-amine. Thorough characterization of cover slips patterned with this method and each step in the functionalization process have been reported previously[147].

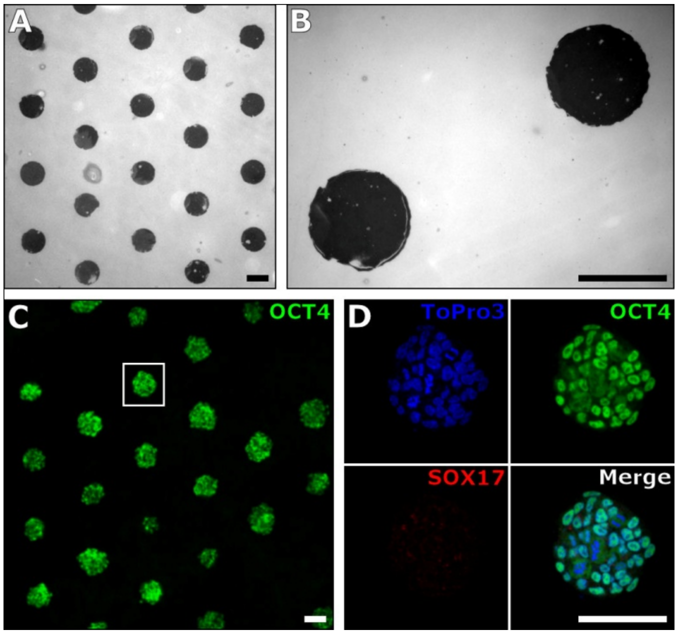

Figure 26 – hESCs grown on patches with microcontact-printed laminin retain OCT4 expression.

Fluorescence microscopic imaging of FITC-BSA bound to the surface between the microcontact-printed 120 μm-diameter circular laminin patches verifies the pattern organization (A and B). Feeder-free hESCs grown for three days on these laminin-coated patches retained expression of the pluripotency marker OCT4 (C and D, green) but did not express the endoderm marker SOX17 (D, red). Nuclear staining with ToPro3 is shown in blue. Scale bars, 100 μm.

After laminin-patterning and mPEG-amine attachment, hESCs were seeded without MEFs on the cover slips at a density of 25000 cells/cm^2, which corresponds to an effective seeding density of ~28000 cells per microcontact-printed glass cover slip. After three days in culture, the patches averaged 36.2 cells (SD=11.2, n=86) growing in compact colonies. The cells in these adherent clusters were positive for the pluripotency marker OCT4, but negative for the endoderm marker SOX17 (Figure 26C and D). When maintained on these laminin patches for more than three days, the cells continued to proliferate (cells in the metaphase and anaphase can be discerned in Figure 26D, top left panel), forming multi-layered cell aggregates that outgrew the 120 μm circular patches and detached during medium refreshment over the next few days.

2.3. Differentiation of hESCs on microcontact-printed glass cover slips

First, we tested whether hESCs could differentiate into definitive endoderm when using medium conditioned by activin A-secreting CHO cells[112] instead of medium supplemented with purified activin A. Subjecting hESCs that were grown on gelatin-coated culture plastic to this modified Stage 1 generated definitive endoderm with high efficiency. At the end of day 3, ~84% of the cells stained for the endoderm marker SOX17 (Figure 3A) as assessed by flow cytometry, and few of these SOX17$^+$ cells (~2.5%) retained high levels of the pluripotency marker OCT4. In contrast, the majority of untreated cells grown under control conditions in unconditioned medium for the same period continued to express high levels of OCT4, and only ~1% expressed SOX17 (Figure 27B). Analysis of the treated cells by immunofluorescence microscopy confirmed these flow cytometry data, showing rare OCT4⁺ cells scattered among the SOX17⁺ majority (Figure 27C).

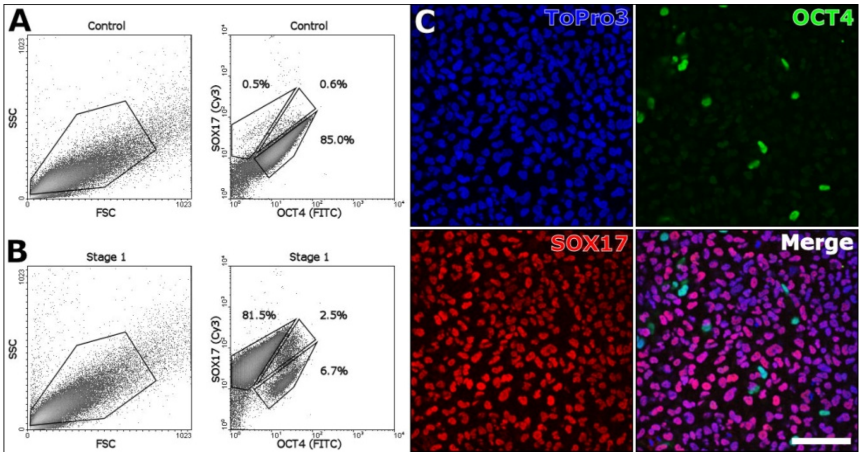

Figure 27 – Differentiation of hESCs into definitive endoderm with high efficiency. *Flow cytometry analysis of hESCs that were differentiated for three days (A and B) shows that OCT4 expression sharply decreased, and SOX17 emerged, when the hESCs were incubated for three days with medium conditioned by activin A-secreting CHO cells (B). In contrast, OCT4 expression was retained when hESCs were differentiated in unconditioned medium (A). Confocal laser scanning microscopy confirmed the differentiation of the treated cells, showing that only a few cells expressed OCT4 (C, green), while the majority upregulated SOX17 (C, red). (C) Nuclear staining with ToPro3 is shown in blue. Scale bars, 100 μm.*

RNA expression analysis by real-time RT-PCR confirmed that the hESCs had differentiated into definitive endoderm. After 3 days of treatment, *OCT4* transcript levels fell dramatically (Figure 28A), whereas *SOX17* (Figure 28B) and *FOXA2* (Figure 28C) mRNA levels increased; *SOX7* mRNA levels were very low in hESCs as well as in the differentiated cells (Figure 28D), indicating that the cells had converted to definitive endoderm rather than visceral endoderm.

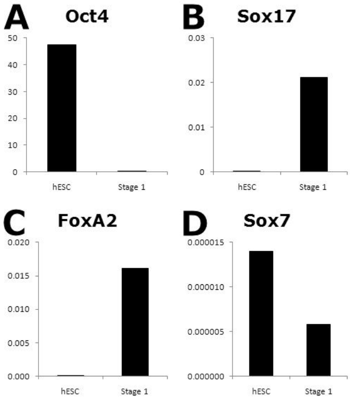

Figure 28 – qPCR data of hESC-derived definitive endoderm.
mRNA levels of OCT4 (A), SOX17 (B), FOXA2 (C), and SOX7 (D) from hESCs and hESC-derived definitive endoderm (Stage 1) were compared by real-time RT-PCR.

Since this differentiation procedure efficiently generated definitive endoderm, we applied the same conditions to the hESCs grown on microcontact-printed cover slips 72 h after plating. When subjected to the conditions for Stage 1, all the cells in each adherent cluster expressed SOX17 on the third day, whereas OCT4 staining was reduced to nearly undetectable levels (Figure 29A).

The Stage 1 cells growing on microcontact-printed cover slips were then sequentially subjected to the succeeding differentiation stages to move them along the pancreatic differentiation lineage. Expression of HNF1β, a marker of the primitive gut tube (i.e. Stage 2), was observed when the cells from Stage 1 were incubated for 3 days with KGF (Figure 29B). Upregulation of HNF1β was associated with a reduction in SOX17 levels, as has been reported previously[19]. Notably, the liver marker albumin was not detected (inset in Figure 29B), suggesting that these cells were not committed to the hepatic lineage.

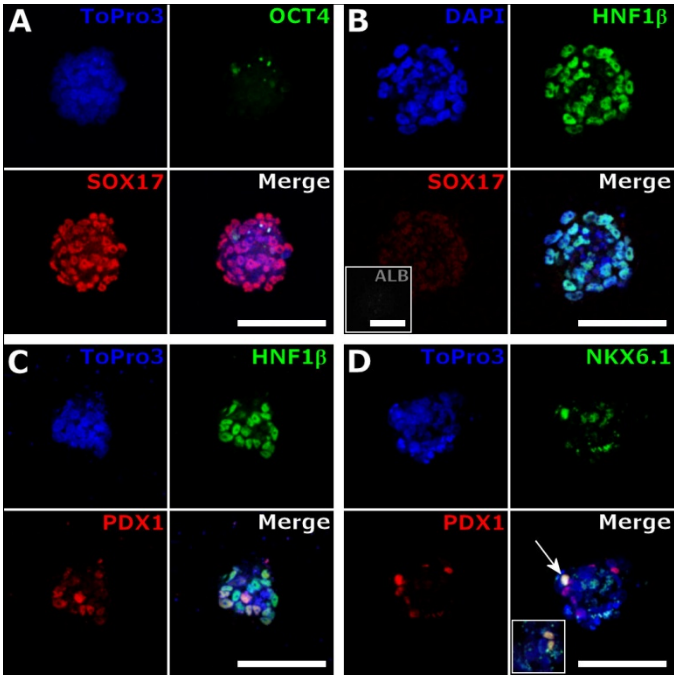

Figure 29 – Differentiation of hESCs into pancreatic endoderm on circular laminin-coated patches.

Confocal microscopic imaging demonstrates hESCs growth and differentiation on circular laminin-coated patches of 120 μm in diameter (A-D). (A) At Stage 1, the cells differentiated to definitive endoderm, as shown by downregulation of OCT4 (green) and upregulation of SOX17 (red). Most of the cells adopted primitive gut tube-like characteristics by the end of Stage 2 (B), as evidenced by upregulation of HNF1β (green), reduction in SOX17 expression (red), and absence of ALB (inset in bottom-left panel; grey). (C) At Stage 3, some of the HNF1β$^+$ cells (green) co-expressed PDX1 (red), thereby resembling posterior foregut cells. Pancreatic endoderm-like cells, marked by the co-expression of NKX6.1 (green) and PDX1 (red) were seen at Stage 5 (D), and usually occurred as single cells (indicated by an arrow in the bottom right panel) or doublets (inset in bottom right panel) in the clusters. Nuclear staining with ToPro3 (top left, bottom left, and bottom right panels) and DAPI (top right panel) is shown in blue. Scale bars, 100 μm.

To further differentiate these cells along the pancreatic pathway to Stage 3 cells, they were incubated for 3 days with a combination of (-)-indolactam V, FGF10, BSA-V, and N2[156]. Not all the cells positive for HNF1β co-expressed PDX1 at the end of Stage 3 (Figure 29C), suggesting that only a portion of these cells had adopted posterior foregut-like properties.

During Stage 4, the cells were maintained in B27-containing medium, resulting in the appearance of NKX6.1$^+$ cells among those positive for PDX1 (Figure 29D). Pancreatic endoderm cells, marked by the co-expression of PDX1 and NKX6.1, were rare and limited to one or two cells per cluster.

2.4. Suspension growth and adherence of detached definitive endoderm clusters

Although some clusters remained attached throughout the entire differentiation protocol, the majority detached after Stage 1. The spherical clumps of cells had a uniform diameter of approximately 100 μm (Figure 31A). When transferred to low-attachment culture plates in the conditions used for Stage 2, the cells in these clusters expressed HNF1β (Figure 31B), as observed for the adherent clusters (Figure 29B). Three-dimensional analysis revealed that essentially all cells in these spherical structures adopted a primitive gut tube-like identity (Figure 31C), suggesting that Stage 2 differentiation in suspension is as efficient as that for adherent cells.

When kept in suspension for an extended time, while proceeding to the subsequent stages, the clusters clumped together, forming larger aggregates of various shapes and sizes. In these suspended clusters, only a few PDX1$^+$ cells were found, some of which were positive for NKX6.1 (Figure 30). On the other hand, when the suspended definitive endoderm clusters were allowed to adhere, and were exposed to the conditions for Stage 3 for three days, PDX1$^+$ posterior foregut-like cells were localized at the centers of the newly adherent clusters (Figure 31D), and were surrounded by an

HNF1β⁺ monolayer. PDX1⁺ cells residing in this HNF1β⁺ monolayer were scattered as single cells or pairs, with the highest density close to the center. Notably, these adherent clusters adopted a colony-like architecture and had lost their original 100 μm-diameter spherical shape.

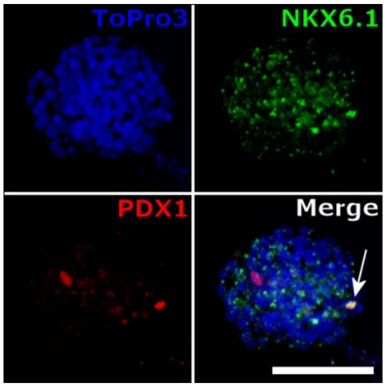

Figure 30 – Suspension differentiation of hESCs into pancreatic endoderm.
Confocal microscopic imaging is shown of hESCs differentiated in suspension into pancreatic endoderm-like cells that co-express of NKX6.1 (green) and PDX1 (red) at Stage 5 (indicated by an arrow). Nuclear staining with ToPro3 is shown in blue. Scale bars, 100 μm.

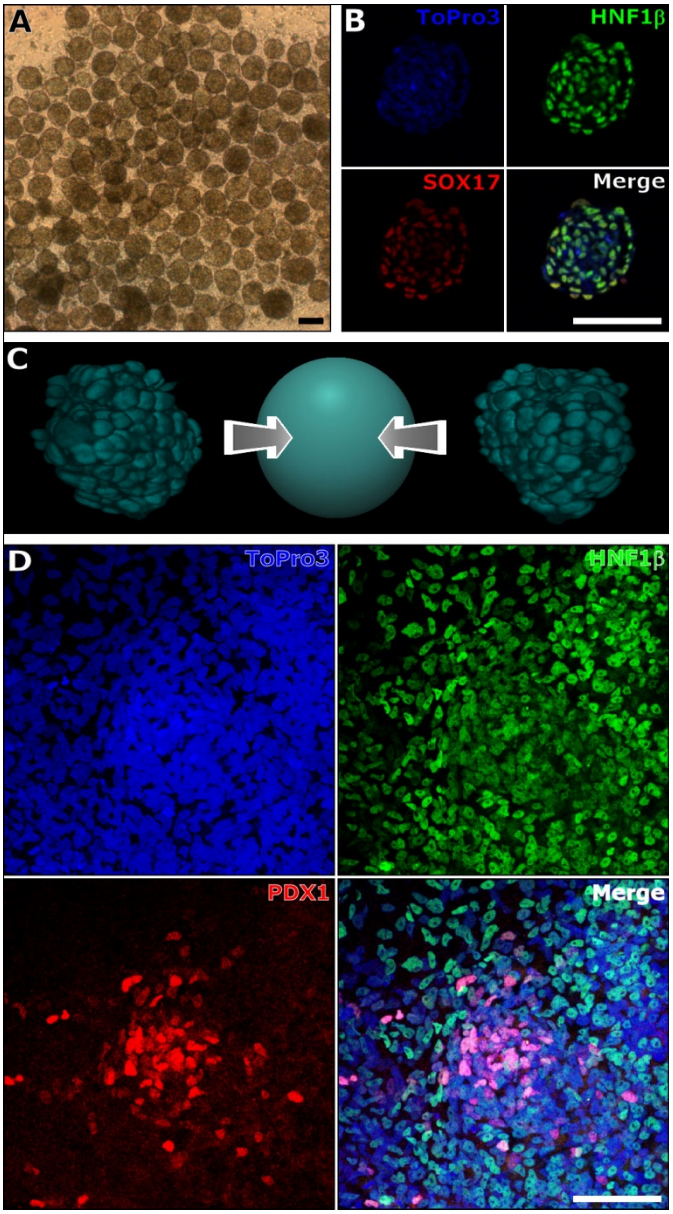

Figure 31 – Suspension differentiation of hESCs into primitive gut tube cells, and into posterior foregut cells after replating.

(A) A bright-field microscopic image is shown of differentiating clusters that dislodged spontaneously after Stage 1. (B) Confocal microscopic images are shown at Stage 2 of a suspended cluster, all cells of which express HNF1β (green) and low levels of SOX17 (red). (C) Side views of a 3-D reconstruction of a cluster similar to that shown in (B); the arrows aimed at the sphere indicate the point of view. (D) A confocal microscopic image is shown of a cluster that was plated at the onset of Stage 3 after having been in suspension during Stage 2. Like others, cells from this cluster express HNF1β (green), with PDX1⁺ cells (red) at the center of the colony-like structure. Nuclear staining with ToPro3 is shown in blue. Scale bars, 100 μm.

3. Discussion

After the demonstration of efficient formation of definitive endoderm[157] and pancreatic endocrine cells from hESCs, efforts have been focused on improving the yield and purity of β-cell-like derivatives, resulting in diverse protocols for generating insulin-producing cells (for reviews, see [143, 158]). However, these insulin-producing cells differentiated in vitro from hESCs do not secrete insulin in response to glucose as normal β-cells do, and share characteristics with a terminal lineage of pancreatic endocrine cells seen early in normal pancreatic development. Only when transplanted at the pancreatic endoderm-equivalent stage (Stage 4) and maintained for several months, do in vitro-generated endocrine precursors mature into glucose-responsive insulin-secreting cells exhibiting characteristics of true β-cells[142]. The failure of the in vitro protocols to generate true β-cells could result from the absence of interacting cells from other lineages (mesoderm and ectoderm) present in the developing pancreatic bud during normal embryonic development of the pancreas. Remarkably, the site of transplantation did not make any substantial difference in the efficacy of pancreatic endoderm maturation[142], thus, a process as simple as vascularization might be sufficient to allow the generation of glucose responsive β-cells.

Although the site of transplantation may not have been critical, the size of transplanted cell clusters was, since 150×150 μm chunks of in vitro-generated pancreatic endoderm gave optimal generation of physiologically regulated β-cells in the transplantation model[142]. In line with this observation, aggregated β-cells release insulin more efficiently than do isolated β-cells[118, 119], and they secrete more insulin from three-dimensional aggregates as opposed to single layers of cells[120]. The optimal cluster size for the differentiation of functional β-cells from hESC-derived pancreatic endoderm-like cells, while avoiding the starvation of cells at the core, needs to be determined. Control over cluster size can be achieved through the patterning of a variety of materials, such as PVA[159], alkanethiolates[125], and laminin[147]. Our studies here have demonstrated the feasibility of controlling cell number as well as colony shape and pattern, using covalently patterned laminin, before initiating an in vitro differentiation procedure.

Transplantation of pancreatic endoderm generated from hESCs or induced pluripotent cells with subsequent differentiation to mature β-cells in vivo could be considered for the treatment of diabetes in human. However, our current laboratory setting for generating cell clusters on microcontact-printed surfaces would be difficult to expand sufficiently to generate enough cells for human trials. In addition to scale-up, preventing massive detachment of the aggregates during the differentiation process would increase the yield of transplantable material significantly. The reduced affinity of the differentiating aggregates for the microcontact-printed substrate may result from changes in the range of anchoring proteins, such as integrins, expressed as the cells undergo further differentiation. Knowledge of the attachment proteins expressed by these cells could be used with the microcontact-printed method to generate ideally constituted and patterned growth surfaces.

Cell detachment may also result from a weakening of the laminin from the glass cover slip. Previously, Fourier transform infrared characterization on cover slips that were patterned using this method verified the attachment of laminin to the underlying aldehyde. However, in-depth analysis of the spectrum revealed a significant spike, which represents an amine, suggesting that multiple layers of laminin had attached[147]. As a result, while a portion of the laminin had bound covalently, the rest could have attached through weaker interactions. Although to a lesser extent than was found in this study, we have observed 832-13 insulinoma cells detaching from microcontact-printed laminin after several days in cell culture conditions, and found that overlaying with low-melting point agarose or other gels could hold the cells in place (data not shown). However, these gels adhere poorly to the PEGylated glass surface, and limit the diffusion of large molecules, like growth factors. Alternatively, a protocol that allows efficient differentiation in suspension once definitive endoderm has been formed would overcome this problem entirely.

4. Conclusion

We have shown the utility of controlling cell cluster size in differentiating hESCs into definitive endoderm and primitive gut tube-like cells with high efficiency, and subsequent differentiation into pancreatic endoderm. To do so, we microcontact-printed patches of laminin onto glass cover slips to serve as an attachment and growth substrate for the hESCs. Optimization and scale-up of this process might yield enough tissue for transplantation studies in diabetic mouse models. Controlling cluster size promises to produce a cellular architecture that enables sufficient nutrient availability as well as physiological insulin secretion. Microcontact-printing provides a feasible approach to the production of cell clusters of desired size for both optimal production and post-transplantation function.

Chapter 7 – Release of Pancreatic β-cell Clusters and ECM Evaluation

1. Introduction

While the majority of this dissertation has focused on techniques to create precise cluster sizes and using those techniques to evaluate the cell behavior and differentiation towards a cell-based type I diabetes therapy, clinical translation requires that these clusters be isolated and interacting with a suitable extracellular environment. Within the past decade, researchers have uncovered significant evidence highlighting the profound impact that the extracellular environment has on cell behavior. These effects can roughly be broken down into three categories: soluble factors, biochemical interactions, and mechanotransduction. With respect to pancreatic β-cells, soluble factors such as IL-1β and TNF-α are implicated in impaired glucose stimulated insulin secretion [160] as well as cell damage [161], while glucose and oxygen availability are necessary to maintain viability and insulin secretion. The impact of biochemical interactions is observed by increased spreading, adhesion, viability and proliferation of INS-1 cells when cultured on collagen I and collagen IV compared with other ligands [133]. Lastly, the impact that matrix stiffness has on cell behavior was made clear in a study demonstrating a direct correlation between substrate stiffness and mesenchymal stem cell fate[162].

Earlier chapters of this dissertation have explored techniques to reduce cell cluster size as a means to achieve greater nutrient availability. The motivation was to improve the soluble factor impact on transplanted cell clusters, although it is possible that non-vascularized clusters made small enough for sufficient nutrient availability to be achieved by diffusion alone will reduce cytokine-mediated cell death as well. However, differentiated embryonic stem cell clusters or patterned clusters from any other cell source will require detachment from the glass coverslip prior to transplantation, and incorporation into a suitably stiff and appropriate biochemical environment to achieve successful outcomes.

This chapter describes methods to detach patterned cell clusters and begins an evaluation of the impact that collagen I concentration, a favorable extracellular matrix ligand[133], has on pancreatic β-cell behavior. The contents of this chapter are intended to serve as a starting place for further evaluation, or to be taken in combination with published literature during clinical translation efforts.

2. *Release of patterned clusters from glass coverslips*

Two methods for releasing patterned cell clusters from microcontact printed laminin have demonstrated successful outcomes. After seeding, cell clusters initially achieve attachment strengths that retain them on the glass coverslip. These cells are attached via covalently bound laminin ligands which can be degraded using the enzyme dispase. A collagenase-dispase solution effectively degrades the intermediate laminin and enables cell clusters to detach over time (Figure 32). The collagenase-dispase does not appear to impact the interaction that cells have within the cluster. As an example, the sparsely populated 120 μm cluster in the bottom right becomes a small cluster as the cells clump together upon releasing from the coverslip. The long-term impact of collagenase-dispase exposure on cell behavior would require further evaluation if this technique is utilized.

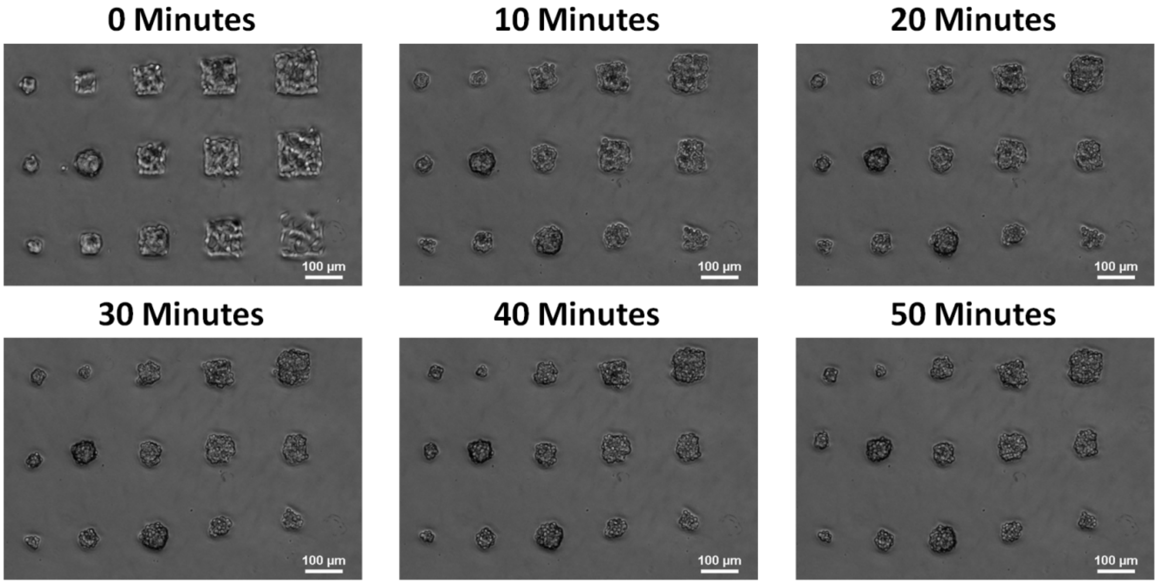

Figure 32 – Release of 832/13 cells on printed laminin using collagenase-dispase

Laminin is printed in square patterns 40, 60, 80, 100 and 120 µm in size on a glass coverslip which enables formation of 832/13 cell clusters of similar sizes. The clusters are exposed to a 1 mg/mL collagenase-dispase solution and time-lapse bright-field microscopy captures images of the clusters as they lose their adhesion to the glass while retaining cell-cell connections.

A second method to release cell clusters from printed laminin becomes apparent after allowing several days of incubation. When 832/13 cells are patterned, excessive proliferation due to the use of an immortalized cell line eventually leads to cell overgrowth of the laminin patterns. However, after the patterned embryonic stem cells described in Chapter 6 differentiate they stop proliferating. Sometime prior to stage 2 of the differentiation protocol, the cell clusters spontaneously lift from the surface, resulting in uniform spheres floating in the culture medium (Figure 31A). Incorporation of released clusters into an ECM material remains the next step for this project, and ideally the material would retain the spacing between clusters to enable sufficient nutrient availability. Vigorous pipetting has resulted in the release of clusters, but the cluster spacing is necessarily lost using this technique.

3. Collagen concentration affects stiffness and permeability

In order to generate increased extracellular matrix stiffness, type I rat tail collagen gels were made in three concentrations: 1, 2, and 3 $^{mg}/_{mL}$. The permeability of the gels were evaluated by evaluating phenol red diffusion through gels formed on transwell semipermeable membranes. Fick's 1st law was employed to extrapolate the diffusivity of each gel to phenol red (Figure 33). The stiffness of different concentrations of collagen was evaluated by formation on a parallel plate rheometer. Elastic moduli were extrapolated from the stress v. strain curve generated (Figure 34). While stiffness was significantly altered as a function of collagen concentration, the affect on permeability to phenol red was not as significant.

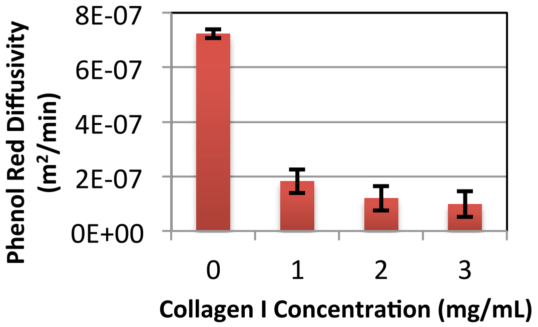

Figure 33 – Collagen I Permeability
Gels were created inside a transwell plate with a semipermeable membrane. The transwell plates were placed into a 12-well plate filled with PBS. Phenol red was introduced on top of the gel, and

concentrations of phenol red in the well-plate over time were used to extrapolate diffusivity. Data is presented as average ± standard deviation.

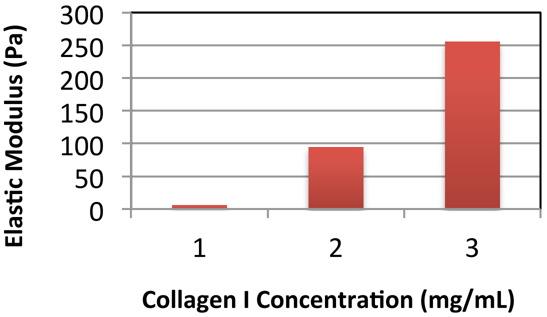

Figure 34 – Collagen I Stiffness

Gels were created in a parallel plate rheometer, reconstituted in PBS and 1N NaOH at 37˚C. After 30 minutes, gel formation occurs. Stress vs. strain measurements were used to extrapolate elastic moduli.

4. Collagen concentration affects metabolic activity

Cell viability is an important indicator for the suitability of an extracellular matrix material. As a result, a metabolic activity assay (MTT) was used to evaluate cells seeded at the same concentration in different concentration collagen gels. From a pure nutrient availability standpoint, one would expect the higher concentration gel to result in lower cell viability, if the permeability was rate-limiting. The equations governing nutrient availability are shown below:

$R_{ma} = \Sigma\, [D_{ma(eff)} \cdot (\Delta C_i/\Delta X_i)]$, from $i=1$ to $i=N_{cap}$
$D_{ma(eff)} = D_{ma} / [\theta \cdot (1+K_p)]$[163]
Rate of nutrient delivery throughout matrix ≡ R_{ma}
Number of cells within matrix ≡ N_{cap}
Effective matrix diffusivity ≡ $D_{ma(eff)}$
Intrinsic matrix diffusivity ≡ D_{ma}
Partition Coefficient ≡ K_p
Tortuosity ≡ θ

Larger concentration gels will have higher tortuosity values, which result in lower matrix diffusivity values and consequently a reduced rate of nutrient delivery. After incubating 832/13 cells in collagen gels of 1, 2, and 3 mg/mL in concentration for 1, 3, 5, or 7 days in normal cell culture media, these cells were subject to GSIS and evaluated for metabolic activity (Figure 35). Interestingly, there is a greater viability measured in the 2 mg/mL Collagen over the first few days than either the 1 mg/mL or the 3 mg/mL concentrations. It is impossible to extrapolate which factors are responsible for this observation, as the availability of collagen ligands, nutrient permeability, and matrix stiffness have opposing effects and differ at each concentration.

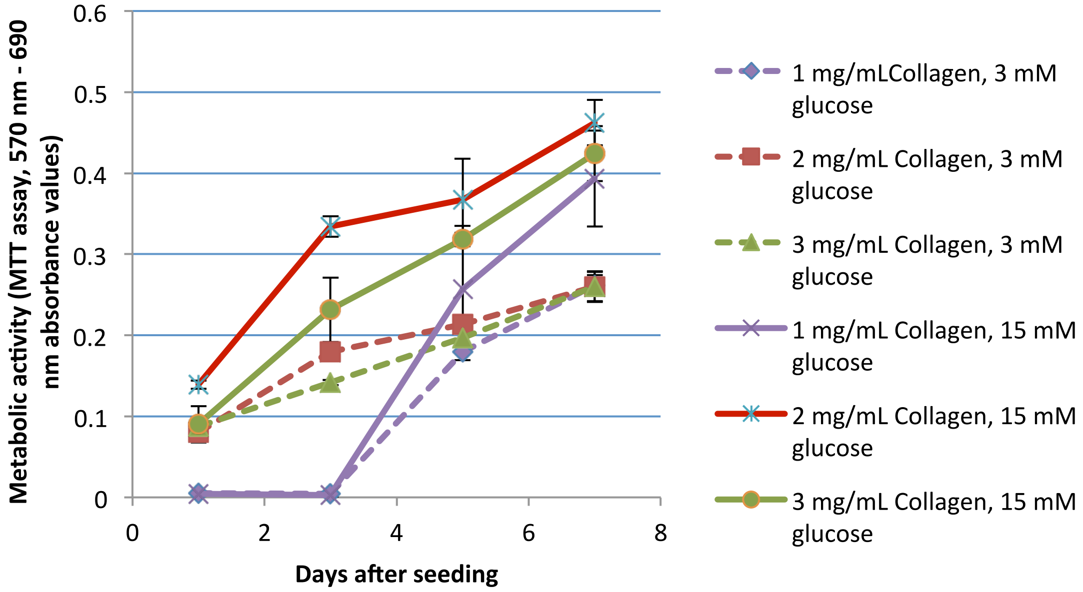

Figure 35 –Effect of Collagen Concentration on 832/13 Insulinoma Cell Viability
Pancreatic β-cells (832/13) were seeded into collagen gels of varying stiffness and evaluated for metabolic activity using an MTT assay at days 1, 3, 5 and 7. Cells were subject to glucose stimulated insulin secretion (GSIS) and stimulated with either 3 or 15 mM glucose without amino acids or fatty free acids for 2 hours prior to evaluation.

Interestingly, the 1 mg/mL collagen matrix did not support initial cell viability. It appears that after an initial period of slow proliferation, the cells reached a plateau of viability that was relatively independent from the concentration gel in which they were embedded. The persistent proliferation of this cell line is to be expected given its immortality.

5. Collagen concentration affects insulin secretion

Collagen gels were further evaluated with respect to their effect on insulin secretion from 832/13 insulinoma cells. Only the 2 and 3 mg/mL collagen gels were included in this evaluation because the likely source for clinical translation will be non-immortal and will require initial viability in its extracellular environment. After incubation in normal cell culture media, cell-seeded collagen gels were subject to GSIS as described in Chapter 2 at 3 and 15 mM glucose. After the samples were obtained from the wells, an MTT assay was performed on each set of cells. The secreted insulin was measured using an insulin ELISA and the values were normalized to viability values corresponding to the same sample (Figure 36). In the cell clusters stimulated at 15 mM glucose, statistically significant results were obtained between medium clusters and large clusters for both the 2 and 3 mg/mL collagen concentrations. These results are consistent with what has been reported throughout this dissertation, although less control over size was utilized in this experiment. Further evaluation of 3-dimensional insulin production and viability from more precisely engineered cell clusters will yield more rigorous results. Nonetheless, these results verify that 832/13 cells maintain their ability to secrete insulin as a function of glucose in 2 and 3 mg/mL collagen I gels, and to do so to a greater extent when cell clusters have grown to a sufficiently large size.

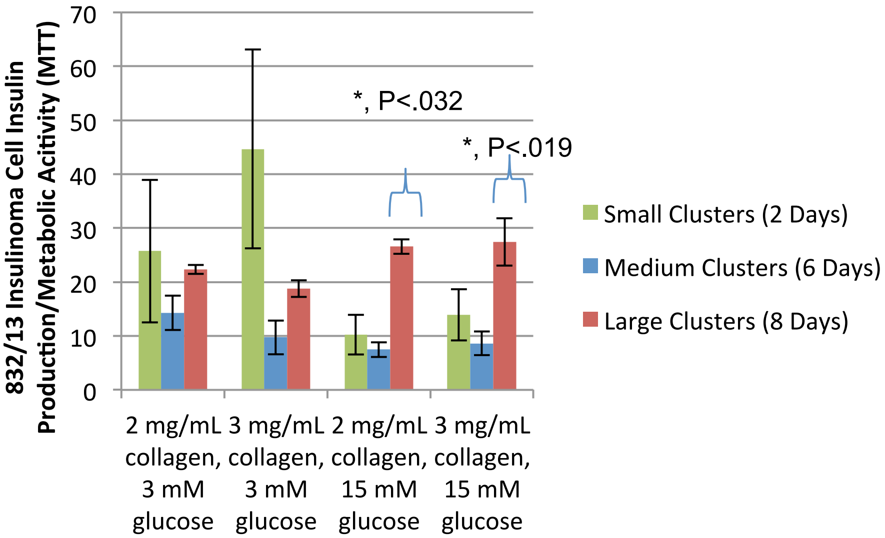

Figure 36 – Effect of Collagen I Concentration on 832/13 Insulin Secretion

832/13 insulinoma cells were seeded at a concentration of 10^6 cells/mL into collagen gels of 2 and 3 mg/mL. After exposure to GSIS at 3 and 15 mM glucose, insulin values obtained from an insulin ELISA were normalized to MTT values of the same sample for clusters grown for 2, 6, and 8 days.

Chapter 8 –Future Direction

The results from the work presented here will provide future researchers and developers of encapsulated transplantation technology with a basis from which to potentially improve the clinical outcomes for this therapy. However, significant work remains before successful clinical translation occurs and the potential benefits of controlling cluster size are evaluated and potentially realized. First, as described earlier, a cell source other than the insulinoma cell line INS-1 (832/13) would be preferable for a clinical trial, and these cells may or may not exhibit the same size-dependent insulin production behavior revealed from the studies. Anticipation of an alternate cell source motivated our study evaluating the differentiation of human embryonic stem cells in patterned clusters, but our process did not yield fully glucose-responsive insulin-secreting cells. Previously, human embryonic stem cells have only achieved characteristics of a fully functional pancreatic β-cell after *in vivo* implantation for 3 months[142]. Therefore, the obvious next step for this project is to transplant detached 120 μm patterned pancreatic precursor cell clusters differentiated human embryonic stem cells using a similar procedure to determine whether they become glucose-responsive insulin-secreting cells. Alternatively, development of an *in vitro* differentiation protocol that successfully achieves the end differentiation goal could avoid the need for *in vivo* differentiation, and efforts to elucidate such a protocol would also be worthwhile. In the case that the patterned human embryonic stem cell clusters can differentiate into fully glucose-responsive insulin-secreting cells, the size of the cluster may also provide optimal viability and insulin secretion behavior, which would represent an extremely exciting step in the development of this therapy.

In order for size-control to realize its full potential, insulin-secreting cell clusters should be encapsulated in a material that avoids the need for immunosuppression. Size-control may not provide as significant a benefit for unencapsulated transplantation therapy that is already able to achieve insulin independence[16]. Therefore, the desired application of the work presented here would be incorporation into an encapsulating environment as described in Chapter 2. Development of new encapsulating environments was not performed because of the widely available approaches, many of which already satisfy the biocompatibility, nutrient availability and immunoisolating requirements that encapsulated transplantation will require. In order to prepare size-controlled clusters for encapsulation, the importance of the extracellular matrix environment on the behavior of insulin-secreting cells was evaluated in Chapter 7, and further work will be required to determine the optimal environment for these cell clusters.

While optimism regarding the benefit that size-control will have on transplant viability and efficacy is suggested by these results, there remains one unaccounted for factor that has been implicated in transplant failure: cytokine-mediated rejection. This rejection pathway is not dealt with in this dissertation. The most advanced encapsulated transplantation trials use alginate microencapsulated porcine islets, and human cytokines will have weaker affinity for porcine cytokine receptors, which might inhibit cytokine-mediated rejection. Alternatively, it is possible that an ideal extracellular environment, as evaluated in Chapter 7, around encapsulated human insulin-secreting cell clusters might prevent the cells from releasing factors that cause cytokine production. Regardless of the approach, continued effort to overcome this rejection pathway will require further effort before high confidence in consistent long-term insulin independence can be expected from encapsulated transplantation therapy.

In conclusion, a technique for fabricating uniform size-controlled insulin-secreting cell clusters was developed and characterized. Evaluation of size-dependent insulin production behavior enabled by this technique suggests an optimal cluster size of 100-120 μm. A renewable cell source, human embryonic stem cells, was then differentiated from 120 μm patterned clusters along the pancreatic lineage with moderate success. Detachment of cell clusters, a necessary step prior to transplantation, was demonstrated with multiple techniques. Lastly, the effect of different extracellular matrix environments for detached cell clusters was evaluated. This dissertation suggests that encapsulated size-controlled clusters of glucose-responsive insulin-secreting cells derived from a renewable supply may improve outcomes for the treament of type I diabetes, and has the potential to provide an effective cure.

References

1. Perlow, M.J., *Brain grafting as a treatment for Parkinson's disease.* Neurosurgery, 1987. **20**(2): p. 335-42.
2. Roberts, T., U. De Boni, and M.V. Sefton, *Dopamine secretion by PC12 cells microencapsulated in a hydroxyethyl methacrylate--methyl methacrylate copolymer.* Biomaterials, 1996. **17**(3): p. 267-75.
3. Machluf, M., et al., *Microencapsulation of Leydig cells: a system for testosterone supplementation.* Endocrinology, 2003. **144**(11): p. 4975-9.
4. Dixit, V. and G. Gitnick, *Transplantation of microencapsulated hepatocytes for liver function replacement.* J Biomater Sci Polym Ed, 1995. **7**(4): p. 343-57.
5. Banting, F.G., Best, C.H., Collip, J.B., Campbell, W.R., Fletcher, A.A., *Pancreatic extracts in the treatment of diabetes mellitus: preliminary report.* CMAJ, 1922. **12**(3): p. 141-146.
6. Minino, A.M., et al., *Deaths: final data for 2004.* Natl Vital Stat Rep, 2007. **55**(19): p. 1-119.
7. Catargi, B., *Current status and future of implantable insulin pumps for the treatment of diabetes.* Expert Rev Med Devices, 2004. **1**(2): p. 181-5.
8. Gray, D.W., *Encapsulated islet cells: the role of direct and indirect presentation and the relevance to xenotransplantation and autoimmune recurrence.* Br Med Bull, 1997. **53**(4): p. 777-88.
9. de Vos, P., et al., *Association between macrophage activation and function of micro-encapsulated rat islets.* Diabetologia, 2003. **46**(5): p. 666-73.
10. Bertuzzi, F., et al., *Tissue factor and CCL2/monocyte chemoattractant protein-1 released by human islets affect islet engraftment in type 1 diabetic recipients.* J Clin Endocrinol Metab, 2004. **89**(11): p. 5724-8.
11. Piro, S., et al., *Bovine islets are less susceptible than human islets to damage by human cytokines.* Transplantation, 2001. **71**(1): p. 21-6.
12. Voltarelli, J.C., et al., *Autologous nonmyeloablative hematopoietic stem cell transplantation in newly diagnosed type 1 diabetes mellitus.* Jama, 2007. **297**(14): p. 1568-76.
13. Gummert, J.F., T. Ikonen, and R.E. Morris, *Newer immunosuppressive drugs: a review.* J Am Soc Nephrol, 1999. **10**(6): p. 1366-80.
14. Penn, I., *Post-transplant malignancy: the role of immunosuppression.* Drug Saf, 2000. **23**(2): p. 101-13.
15. Bretzel, R.G., *Current status and perspectives in clinical islet transplantation.* J Hepatobiliary Pancreat Surg, 2000. **7**(4): p. 370-3.
16. Shapiro, A.M., et al., *Islet transplantation in seven patients with type 1 diabetes mellitus using a glucocorticoid-free immunosuppressive regimen.* N Engl J Med, 2000. **343**(4): p. 230-8.
17. Ryan, E.A., et al., *Five-year follow-up after clinical islet transplantation.* Diabetes, 2005. **54**(7): p. 2060-9.
18. Efrat, S., *Cell replacement therapy for type 1 diabetes.* Trends Mol Med, 2002. **8**(7): p. 334-39.
19. D'Amour, K.A., et al., *Production of pancreatic hormone-expressing endocrine cells from human embryonic stem cells.* Nat Biotechnol, 2006. **24**(11): p. 1392-401.
20. Gray, D.W., *Comment on "reversal of diabetes in non-immunosuppressed rhesus macaques by intraportal porcine islet xenografts precedes acute cellular rejection".* Xenotransplantation, 2004. **11**(5): p. 394-5.

21. Lacy, P.E., J.M. Davie, and E.H. Finke, *Prolongation of islet allograft survival following in vitro culture (24 degrees C) and a single injection of ALS.* Science, 1979. **204**(4390): p. 312-3.
22. Rogers, S.A., et al., *Islet cell engraftment and control of diabetes in rats after transplantation of pig pancreatic anlagen.* Am J Physiol Endocrinol Metab, 2004. **286**(4): p. E502-9.
23. Hammerman, M.R., *Transplantation of embryonic organs - kidney and pancreas.* Am J Transplant, 2004. **4 Suppl 6**: p. 14-24.
24. Eventov-Friedman, S., et al., *Embryonic pig pancreatic tissue transplantation for the treatment of diabetes.* PLoS Med, 2006. **3**(7): p. e215.
25. Mandel, T.E., *Fetal islet xenotransplantation in rodents and primates.* J Mol Med, 1999. **77**(1): p. 155-60.
26. Bisceglie, V.V., *Uber die antineoplastiche Immunitat.* E. Krebsforch, 1933. **40**(141).
27. Algire, G.H. and F.Y. Legallais, *Recent developments in the transparent-chamber technique as adapted to the mouse.* J Natl Cancer Inst, 1949. **10**(2): p. 225-53, incl 8 pl.
28. Algire, G.H., J.M. Weaver, and R.T. Prehn, *Growth of cells in vivo in diffusion chambers. I. Survival of homografts in immunized mice.* J Natl Cancer Inst, 1954. **15**(3): p. 493-507.
29. Prehn, R.T., J.M. Weaver, and G.H. Algire, *The diffusion-chamber technique applied to a study of the nature of homograft resistance.* J Natl Cancer Inst, 1954. **15**(3): p. 509-17.
30. Weaver, J.M., G.H. Algire, and R.T. Prehn, *The growth of cells in vivo in diffusion chambers. II. The role of cells in the destruction of homografts in mice.* J Natl Cancer Inst, 1955. **15**(6): p. 1737-67.
31. Moskalewski, S., *Isolation And Culture Of The Islets Of Langerhans Of The Guinea Pig.* Gen Comp Endocrinol, 1965. **44**: p. 342-53.
32. Lanza, R.P., J.L. Hayes, and W.L. Chick, *Encapsulated cell technology.* Nat Biotechnol, 1996. **14**(9): p. 1107-11.
33. Maki, T., *Islet transplantation in the future: Use of a bioartificial pancreas.* Journal of Hep Bil Pancr Surgery, 1996. **3**: p. 275-279.
34. Scharp, D.W., N.S. Mason, and R.E. Sparks, *Islet immuno-isolation: the use of hybrid artificial organs to prevent islet tissue rejection.* World J Surg, 1984. **8**(2): p. 221-9.
35. Slater, N.J., A.T. Raftery, and G.H. Cope, *The ultrastructure of human abdominal mesothelium.* J Anat, 1989. **167**: p. 47-56.
36. Chick, W.L., A.A. Like, and V. Lauris, *Beta cell culture on synthetic capillaries: an artificial endocrine pancreas.* Science, 1975. **187**(4179): p. 847-9.
37. Knazek, R.A., et al., *Cell culture on artificial capillaries: an approach to tissue growth in vitro.* Science, 1972. **178**(56): p. 65-6.
38. Orsetti, A., et al., *[Implantation of a bio-artificial insulin distributor in dogs, using islets of Langerhans from different animal species].* C R Seances Soc Biol Fil, 1978. **172**(1): p. 144-50.
39. Sun, A.M., et al., *The use, in diabetic rats and monkeys, of artificial capillary units containing cultured islets of Langerhans (artificial endocrine pancreas).* Diabetes, 1977. **26**(12): p. 1136-9.
40. Tze, W.J., et al., *Implantable artificial endocrine pancreas unit used to restore normoglycaemia in the diabetic rat.* Nature, 1976. **264**(5585): p. 466-7.
41. Sullivan, S.J., et al., *Biohybrid artificial pancreas: long-term implantation studies in diabetic, pancreatectomized dogs.* Science, 1991. **252**(5006): p. 718-21.
42. Theodorou, N.A. and S.L. Howell, *An assessment of diffusion chambers for use in pancreatic islet cell transplantation.* Transplantation, 1979. **27**(5): p. 350-2.

43. Colton, C.K., *Implantable biohybrid artificial organs.* Cell Transplant, 1995. **4**(4): p. 415-36.
44. Yang, H., et al., *Comparative studies of in vitro and in vivo function of three different shaped bioartificial pancreases made of agarose hydrogel.* Biomaterials, 1994. **15**(2): p. 113-20.
45. Chang, T.M., *Semipermeable Microcapsules.* Science, 1964. **146**: p. 524-5.
46. Lim, F. and A.M. Sun, *Microencapsulated islets as bioartificial endocrine pancreas.* Science, 1980. **210**(4472): p. 908-10.
47. O'Shea, G.M., M.F. Goosen, and A.M. Sun, *Prolonged survival of transplanted islets of Langerhans encapsulated in a biocompatible membrane.* Biochim Biophys Acta, 1984. **804**(1): p. 133-6.
48. Klock, G., et al., *Production of purified alginates suitable for use in immunoisolated transplantation.* Appl Microbiol Biotechnol, 1994. **40**(5): p. 638-43.
49. Otterlei, M., et al., *Induction of cytokine production from human monocytes stimulated with alginate.* J Immunother, 1991. **10**(4): p. 286-91.
50. Sefton, M.V., Stevenson, W.T.K., *Microencapsulation of Live Animal Cells Using Polyacrylates.* Adv. Polym. Sci., 1993. **107**: p. 143-197.
51. Sawhney, A.S., C.P. Pathak, and J.A. Hubbell, *Interfacial photopolymerization of poly(ethylene glycol)-based hydrogels upon alginate-poly(l-lysine) microcapsules for enhanced biocompatibility.* Biomaterials, 1993. **14**(13): p. 1008-16.
52. Peterson, K.P., C.M. Peterson, and E.J. Pope, *Silica sol-gel encapsulation of pancreatic islets.* Proc Soc Exp Biol Med, 1998. **218**(4): p. 365-9.
53. Wang, T., et al., *An encapsulation system for the immunoisolation of pancreatic islets.* Nat Biotechnol, 1997. **15**(4): p. 358-62.
54. de Vos, P., et al., *Alginate-based microcapsules for immunoisolation of pancreatic islets.* Biomaterials, 2006. **27**(32): p. 5603-17.
55. Orive, G., et al., *History, challenges and perspectives of cell microencapsulation.* Trends Biotechnol, 2004. **22**(2): p. 87-92.
56. Calafiore, R., et al., *Microencapsulated pancreatic islet allografts into nonimmunosuppressed patients with type 1 diabetes: first two cases.* Diabetes Care, 2006. **29**(1): p. 137-8.
57. *Novocell presents phase I/II data on safety and response to encapsulated islets at the American Diabetes Association's 66th annual scientific session*. http://novocell.com/news/press/2006-06-12.html 2006.
58. Soon-Shiong, P., et al., *Insulin independence in a type 1 diabetic patient after encapsulated islet transplantation.* Lancet, 1994. **343**(8903): p. 950-1.
59. *Living Cell Technologies updates shareholders on clinical trial progress at annual general meeting* http://www.lctglobal.com/news/LCT%20AGM%20update.pdf 2007.
60. *MicroIlset and Progenitor Cell Therapy enter into agreement for the manufacturing of MicroIslet-P, an encapsulated islet cell product for the treatment of type 1 diabetes*. http://phx.corporate-ir.net/phoenix.zhtml?c=122178&p=irol-newsArticle&t=Regular&id=1053966& 2007.
61. King, A., *Microencapsulation of islets of Langerhans: impact of cellular overgrowth.* Ups J Med Sci, 2001. **106**(3): p. 161-74.
62. De Vos, P., et al., *Why do microencapsulated islet grafts fail in the absence of fibrotic overgrowth?* Diabetes, 1999. **48**(7): p. 1381-8.
63. Sabatine, M.S., et al., *Delayed rejection of soluble tumor necrosis factor receptor-secreting tumor allografts.* Transplantation, 1998. **65**(1): p. 113-20.

64. Sandberg, J.O., et al., *Treatment with an interleukin-1 receptor antagonist protein prolongs mouse islet allograft survival.* Diabetes, 1993. **42**(12): p. 1845-51.
65. Dunleavy, M., *Polymeric membranes. A review of applications.* Med Device Technol, 1996. **7**(4): p. 14-6, 18-21.
66. Weber, C.J., et al., *Evaluation of graft-host response for various tissue sources and animal models.* Ann N Y Acad Sci, 1999. **875**: p. 233-54.
67. De Vos, P., et al., *Factors influencing the adequacy of microencapsulation of rat pancreatic islets.* Transplantation, 1996. **62**(7): p. 888-93.
68. Teramura, Y., Y. Kaneda, and H. Iwata, *Islet-encapsulation in ultra-thin layer-by-layer membranes of poly(vinyl alcohol) anchored to poly(ethylene glycol)-lipids in the cell membrane.* Biomaterials, 2007.
69. Wang, R.N. and L. Rosenberg, *Maintenance of beta-cell function and survival following islet isolation requires re-establishment of the islet-matrix relationship.* J Endocrinol, 1999. **163**(2): p. 181-90.
70. Gates, R.J., et al., *Return to normal of blood-glucose, plasma-insulin, and weight gain in New Zealand obese mice after implantation of islets of Langerhans.* Lancet, 1972. **2**(7777): p. 567-70.
71. Strautz, R.L., *Studies of hereditary-obese mice (obob) after implantation of pancreatic islets in Millipore filter capsules.* Diabetologia, 1970. **6**(3): p. 306-12.
72. Beck, J., et al., *Islet encapsulation: strategies to enhance islet cell functions.* Tissue Eng, 2007. **13**(3): p. 589-99.
73. Lysaght, M.J., et al., *Recent progress in immunoisolated cell therapy.* J Cell Biochem, 1994. **56**(2): p. 196-203.
74. Leoni, L. and T.A. Desai, *Micromachined biocapsules for cell-based sensing and delivery.* Adv Drug Deliv Rev, 2004. **56**(2): p. 211-29.
75. Loudovaris, T., et al., *Correction of diabetic nod mice with insulinomas implanted within Baxter immunoisolation devices.* J Mol Med, 1999. **77**(1): p. 219-22.
76. *Pioneer Surgical Technology acquires Encelle, Inc.* http://encelle.com 2007.
77. Smith, C., et al., *Diffusion characteristics of microfabricated silicon nanopore membranes as immunoisolation membranes for use in cellular therapeutics.* Diabetes Technol Ther, 2005. **7**(1): p. 151-62.
78. Desai, T.A., et al., *Microfabricated biocapsules provide short-term immunoisolation of insulinoma xenografts.* Biomed Microdevices, 1999. **1**(2): p. 131-8.
79. Desai, T.A., et al., *Microfabricated immunoisolating biocapsules.* Biotechnol Bioeng, 1998. **57**(1): p. 118-20.
80. Storrs, R., et al., *Preclinical development of the Islet Sheet.* Ann N Y Acad Sci, 2001. **944**: p. 252-66.
81. Chu, W.H., et al., *Silicon Membrane Nanofilters from Sacrificial Oxide Removal.* Journal of MEMS, 1999. **8**(1): p. 34-42.
82. Leoni, L., Attiah, Darlene, Desai, Tejal A., *Nanoporous platforms for cellular sensing and delivery.* Sensors, 2002. **2**: p. 111-120.
83. Desai, T.A., et al., *Nanoporous anti-fouling silicon membranes for biosensor applications.* Biosens Bioelectron, 2000. **15**(9-10): p. 453-62.
84. Leoni, L., Boiarski, Anthony, Desai, Tejal A., *Characterization of nanoporous membranes for immunoisolation: Diffusion properties and tissue effects.* Biomedical Microdevices, 2002. **4**(2): p. 131-139.

85. Desai, T.A., D.J. Hansford, and M. Ferrari, *Characterization of micromachined silicon membranes for immunoisolation and bioseparation applications.* J of Mem. Sci., 1999(159): p. 221-231.

86. Desai, T.A., et al., *Nanoporous microsystems for islet cell replacement.* Adv Drug Deliv Rev, 2004. **56**(11): p. 1661-73.

87. Desai, T.A., D.J. Hansford, and M. Ferrari, *Micromachined interfaces: new approaches in cell immunoisolation and biomolecular separation.* Biomol Eng, 2000. **17**(1): p. 23-36.

88. La Flamme, K.E., et al., *Nanoporous alumina capsules for cellular macroencapsulation: transport and biocompatibility.* Diabetes Technol Ther, 2005. **7**(5): p. 684-94.

89. Chou, S.Y., et al., *Sub-10 nm imprint lithography and applications.* J. Vac. Sci. Technol. B, 1997. **15**(6): p. 2897-2904.

90. Masuda, H. and K. Fukuda, *Ordered Metal Nanohole Arrays Made by a Two-Step Replication of Honeycomb Structures of Anodic Alumina.* Science, 1995. **268**: p. 1466-1468.

91. Masuda, H. and M. Satoh, *Fabrication of Gold Nanodot Array Using Anodic Porous Alumina as an Evaporation Mask.* Jpn. J. Appl. Phys., 1996. **35**: p. 126-129.

92. Gong, D., et al., *Controlled Molecular Release Using Nanoporous Alumina Capsules.* Biomedical Microdevices, 2003. **5**(1): p. 75-80.

93. Popat, K.C., et al., *Surface modification of nanoporous alumina surfaces with poly(ethylene glycol).* Langmuir, 2004. **20**(19): p. 8035-41.

94. Swan, E.E., et al., *Fabrication and evaluation of nanoporous alumina membranes for osteoblast culture.* J Biomed Mater Res A, 2005. **72**(3): p. 288-95.

95. Itoh, N., et al., *Strengthened porous alumina membrane tube prepared by means of internal anodic oxidation.* Microporous and Mesoporous Materials, 1998. **20**: p. 333-337.

96. Li, A.P., et al., *Polycrystalline nanopore arrays with hexagonal ordering on aluminum.* J. Vac. Sci. Technol. A, 1999. **17**(4): p. 1428-1431.

97. Thomas, P., et al., *Immuno-allergological properties of aluminium oxide (Al2O3) ceramics and nickel sulfate in humans.* Biomaterials, 2003. **24**(6): p. 959-66.

98. La Flamme, K.E., et al., *Biocompatibility of nanoporous alumina membranes for immunoisolation.* Biomaterials, 2007. **28**(16): p. 2638-45.

99. Popat, K.C. and T.A. Desai, *Poly(ethylene glycol) interfaces: an approach for enhanced performance of microfluidic systems.* Biosens Bioelectron, 2004. **19**(9): p. 1037-44.

100. Beranek, R., H. Hildebrand, and P. Schmuki, *Self-organized porous titanium oxide prepared in H2SO4/HF Electrolytes.* Electrochemcial and Solid-State Letters, 2003. **6**(3): p. B12-B14.

101. Cai, Q., et al., *The effect of electrolyte composition on the fabrication of self-organized titanium oxide nanotube arrays by anodic oxidation.* J. Mater. Res., 2004. **20**(1): p. 230-236.

102. Gong, D., C.A. Grimes, and O.K. Varghese, *Titanium oxide nanotube arrays prepared by anodic oxidation.* J. Mater. Res., 2001. **16**(12): p. 3331-3334.

103. Paulose, M., et al., *Anodic growth of highly ordered TiO2 nanotube arrays to 134 um in length.* J. of Phys. Chem. B, 2006. **110**(33): p. 16179-16184.

104. Ruan, C., et al., *Fabrication of highly ordered TiO2 nanotube arrays using an organic electrolyte.* J. Phys. Chem. B, 2005. **109**: p. 15754-15759.

105. Zhao, J., et al., *In situ templated synthesis of anatase single-crystal nanotube arrays.* Nanotechnology, 2005. **16**: p. 2450-2454.

106. Paulose, M., Prakasam, E. Haripriya, Varghese, Oomman K., Peng, Lily, Popat, Ketul C., Mor, Gopal K., Desai, Tejal A., Grimes, Craig A., *TiO2 Nanotube arrays of 1000 micron length by anodization of titanium foil: phenol red diffusion.* J. Phys. Chem. C, 2007. **111**(41): p. 14992-14997.
107. Mor, G.K., Varghese, Oomman K., Paulose, Maggie, Mukherjee, Niloy, Grimes, Craig A., *Fabrication of tapered, conical-shaped titania nanotubes.* J. Mater. Res., 2003. **18**(11).
108. Macak, J.M., H. Tsuchiya, and P. Schmuki, *High-aspect-ratio TiO2 nanotubes by anodization of titanium.* Angew. Chem. Int. Ed., 2005. **44**: p. 2100-2102.
109. Choi, J., et al., *Porous niobium oxide films prepared by anodization-annealing-anodization.* Nanotechnology, 2007. **18**.
110. Sieber, I., B. Kannan, and P. Schmuki, *Self-assembled porous tantalum oxide prepared in H2SO4/HF Electrolytes.* Electrochemical and Solid-State Letters, 2005. **8**(3): p. J10-J12.
111. Hohmeier, H.E., et al., *Isolation of INS-1-derived cell lines with robust ATP-sensitive K+ channel-dependent and -independent glucose-stimulated insulin secretion.* Diabetes, 2000. **49**(3): p. 424-30.
112. Arai, K.Y., et al., *Purification of recombinant activin A using the second follistatin domain of follistatin-related gene (FLRG).* Protein Expr Purif, 2006. **49**(1): p. 78-82.
113. Van Hoof, D., et al., *Phosphorylation dynamics during early differentiation of human embryonic stem cells.* Cell Stem Cell, 2009. **5**(2): p. 214-26.
114. Ichii, H. and C. Ricordi, *Current status of islet cell transplantation.* J Hepatobiliary Pancreat Surg, 2009. **16**(2): p. 101-12.
115. Shapiro, A.M., C. Ricordi, and B. Hering, *Edmonton's islet success has indeed been replicated elsewhere.* Lancet, 2003. **362**(9391): p. 1242.
116. Lehmann, R., et al., *Superiority of small islets in human islet transplantation.* Diabetes, 2007. **56**(3): p. 594-603.
117. Lau, J. and P.O. Carlsson, *Low revascularization of human islets when experimentally transplanted into the liver.* Transplantation, 2009. **87**(3): p. 322-5.
118. Meda, P., et al., *Rapid and reversible secretion changes during uncoupling of rat insulin-producing cells.* J Clin Invest, 1990. **86**(3): p. 759-68.
119. Jaques, F., et al., *Dual effect of cell-cell contact disruption on cytosolic calcium and insulin secretion.* Endocrinology, 2008. **149**(5): p. 2494-505.
120. Brereton, H.C., et al., *Homotypic cell contact enhances insulin but not glucagon secretion.* Biochem Biophys Res Commun, 2006. **344**(3): p. 995-1000.
121. Meda, P., *Cx36 involvement in insulin secretion: characteristics and mechanism.* Cell Commun Adhes, 2003. **10**(4-6): p. 431-5.
122. Bavamian, S., et al., *Islet-cell-to-cell communication as basis for normal insulin secretion.* Diabetes Obes Metab, 2007. **9 Suppl 2**: p. 118-32.
123. Nittala, A., S. Ghosh, and X. Wang, *Investigating the role of islet cytoarchitecture in its oscillation using a new beta-cell cluster model.* PLoS One, 2007. **2**(10): p. e983.
124. Kumar, A., H.A. Biebuyck, and G.M. Whitesides, *Patterning Self-Assembled Monolayers: Applications in Materials Science.* Langmuir, 1994. **10**(5): p. 1498-1511.
125. Mrksich, M., et al., *Using microcontact printing to pattern the attachment of mammalian cells to self-assembled monolayers of alkanethiolates on transparent films of gold and silver.* Exp Cell Res, 1997. **235**(2): p. 305-13.
126. Chen, C.S., et al., *Geometric control of cell life and death.* Science, 1997. **276**(5317): p. 1425-8.
127. Hou, S., et al., *Patterning of 293T fibroblasts on a mica surface.* Anal Bioanal Chem, 2009. **394**(8): p. 2111-7.

128. Rozkiewicz, D.I., et al., *Covalent microcontact printing of proteins for cell patterning.* Chemistry, 2006. **12**(24): p. 6290-7.
129. de la Fuente, J.M., et al., *Fluorescent aromatic platforms for cell patterning.* Langmuir, 2006. **22**(13): p. 5528-32.
130. Rozkiewicz, D.I., B.J. Ravoo, and D.N. Reinhoudt, *Reversible covalent patterning of self-assembled monolayers on gold and silicon oxide surfaces.* Langmuir, 2005. **21**(14): p. 6337-43.
131. Lahann, J., et al., *Reactive polymer coatings: A platform for patterning proteins and mammalian cells onto a broad range of materials.* Langmuir, 2002. **18**(9): p. 3632-3638.
132. Cavallari, G., et al., *Rat pancreatic islet size standardization by the "hanging drop" technique.* Transplant Proc, 2007. **39**(6): p. 2018-20.
133. Krishnamurthy, M., et al., *Expression and function of alphabeta1 integrins in pancretic beta (INS-1) cells.* J Cell Commun Signal, 2008. **2**(3-4): p. 67-79.
134. Miller, A.W. and J.F. Robyt, *Sodium cyanoborohydride in the immobilization of proteins to glutaraldehyde-activated aminoalkyl silica.* Biotechnol Bioeng, 1983. **25**(11): p. 2795-2800.
135. Saneinejad, S. and M.S. Shoichet, *Patterned glass surfaces direct cell adhesion and process outgrowth of primary neurons of the central nervous system.* J Biomed Mater Res, 1998. **42**(1): p. 13-9.
136. Bisceglie, V., *Uber die antineoplastiche Immunitat.* E Krebsforsch, 1933. **40**: p. 141-158.
137. Matsumoto, S., et al., *Estimation of donor usability for islet isolation with the modified Ricordi method.* Transplant Proc, 2008. **40**(2): p. 362-3.
138. Mendelsohn, A. and T. Desai, *Inorganic nanoporous membranes for immunoisolated cell-based drug delivery.* Adv Exp Med Biol, 2010. **670**: p. 104-25.
139. Wilson, J.T. and E.L. Chaikof, *Challenges and emerging technologies in the immunoisolation of cells and tissues.* Adv Drug Deliv Rev, 2008. **60**(2): p. 124-45.
140. Elliott, R.B., et al., *Live encapsulated porcine islets from a type 1 diabetic patient 9.5 yr after xenotransplantation.* Xenotransplantation, 2007. **14**(2): p. 157-61.
141. Thanos, C.G. and R.B. Elliott, *Encapsulated porcine islet transplantation: an evolving therapy for the treatment of type I diabetes.* Expert Opin Biol Ther, 2009. **9**(1): p. 29-44.
142. Kroon, E., et al., *Pancreatic endoderm derived from human embryonic stem cells generates glucose-responsive insulin-secreting cells in vivo.* Nat Biotechnol, 2008. **26**(4): p. 443-52.
143. Van Hoof, D., K.A. D'Amour, and M.S. German, *Derivation of insulin-producing cells from human embryonic stem cells.* Stem Cell Res, 2009. **3**(2-3): p. 73-87.
144. Jonkers, F.C., et al., *Influence of cell number on the characteristics and synchrony of Ca2+ oscillations in clusters of mouse pancreatic islet cells.* J Physiol, 1999. **520 Pt 3**: p. 839-49.
145. Orive, G., et al., *Biocompatibility of alginate-poly-L-lysine microcapsules for cell therapy.* Biomaterials, 2006. **27**(20): p. 3691-700.
146. Ballian, N. and F.C. Brunicardi, *Islet vasculature as a regulator of endocrine pancreas function.* World J Surg, 2007. **31**(4): p. 705-14.
147. Mendelsohn, A.D., et al., *Patterning of mono- and multilayered pancreatic beta-cell clusters.* Langmuir, 2010. **26**(12): p. 9943-9.
148. Van Hoof, D., et al., *Differentiation of human embryonic stem cells into pancreatic endoderm in patterned size-controlled clusters.* Stem Cell Res, 2011. **In Press**.

149. Block, M.B., et al., *Sequential changes in beta-cell function in insulin-treated diabetic patients assessed by C-peptide immunoreactivity.* N Engl J Med, 1973. **288**(22): p. 1144-8.
150. Steiner, D.F., et al., *Insulin biosynthesis: evidence for a precursor.* Science, 1967. **157**(789): p. 697-700.
151. Rajagopal, J., et al., *Insulin staining of ES cell progeny from insulin uptake.* Science, 2003. **299**(5605): p. 363.
152. Gold, G., et al., *Heterogeneity and compartmental properties of insulin storage and secretion in rat islets.* J Clin Invest, 1982. **69**(3): p. 554-63.
153. Van Hoof, D., et al., *Feeder-free monolayer cultures of human embryonic stem cells express an epithelial plasma membrane protein profile.* Stem Cells, 2008. **26**(11): p. 2777-81.
154. Van Hoof, D., et al., *A quest for human and mouse embryonic stem cell-specific proteins.* Mol Cell Proteomics, 2006. **5**(7): p. 1261-73.
155. Dormeyer, W., et al., *Plasma membrane proteomics of human embryonic stem cells and human embryonal carcinoma cells.* J Proteome Res, 2008. **7**(7): p. 2936-51.
156. Chen, S., et al., *A small molecule that directs differentiation of human ESCs into the pancreatic lineage.* Nat Chem Biol, 2009. **5**(4): p. 258-65.
157. D'Amour, K.A., et al., *Efficient differentiation of human embryonic stem cells to definitive endoderm.* Nat Biotechnol, 2005. **23**(12): p. 1534-41.
158. Mfopou, J.K., et al., *Recent advances and prospects in the differentiation of pancreatic cells from human embryonic stem cells.* Diabetes, 2010. **59**(9): p. 2094-101.
159. Cheng, C.M. and P.R. LeDuc, *Micropatterning polyvinyl alcohol as a biomimetic material through soft lithography with cell culture.* Mol Biosyst, 2006. **2**(6-7): p. 299-303.
160. Ma, Z., et al., *Interleukin-1 reduces the glycolytic utilization of glucose by pancreatic islets and reduces glucokinase mRNA content and protein synthesis by a nitric oxide-dependent mechanism.* J Biol Chem, 1997. **272**(28): p. 17827-35.
161. Cetkovic-Cvrlje, M. and D.L. Eizirik, *TNF-alpha and IFN-gamma potentiate the deleterious effects of IL-1 beta on mouse pancreatic islets mainly via generation of nitric oxide.* Cytokine, 1994. **6**(4): p. 399-406.
162. Engler, A.J., et al., *Matrix elasticity directs stem cell lineage specification.* Cell, 2006. **126**(4): p. 677-89.
163. Colton, C., *Mathematics of Diffusion*. 1975.

Publishing Agreement

It is the policy of the University to encourage the distribution of all theses, dissertations, and manuscripts. Copies of all UCSF theses, dissertations, and manuscripts will be routed to the library via the Graduate Division. The library will make all theses, dissertations, and manuscripts accessible to the public and will preserve these to the best of their abilities, in perpetuity.

Please sign the following statement:

I hereby grant permission to the Graduate Division of the University of California, San Francisco to release copies of my thesis, dissertation, or manuscript to the Campus Library to provide access and preservation, in whole or in part, in perpetuity.

3-17-11

Author Signature

Date